Characteristics of Neutron Stars from X-Rays Observations

by

Khaled G. Elshamouty

A thesis submitted in partial fulfillment of the requirements for the degree of

Doctor of Philosophy

Department of Physics
University of Alberta

Abstract

Neutron stars (NSs) are some of the densest objects in the universe. In this thesis, I focus on studying X-ray thermal emission from neutron stars, using X-ray observations of different varieties of NSs. X-ray observations can put constraints on the mass and radius of NSs, and thus on density and pressure of neutron star interiors, with consequences for the dense matter equation of state. X-ray observations can also constrain the temperature of NSs, with implications for the superfluidity of the core, and the composition and superfluid state of the crust.

In the first part of this thesis, I constrain the cooling of the NS surface temperature in the young NS in the Cas A supernova remnant, using X-ray flux measurements over 10 years using several detectors on the Chandra X-ray Observatory. Although measurements using Chandra's ACIS-S detector show fast cooling, measurements using Chandra's HRC-S detector find a significantly slower rate of cooling for this NS.

Fitting the thermal X-ray spectra of neutron stars in quiescent X-ray binaries can be used to measure the NS radii. However, the effect of undetected hot spots on the spectrum, and thus on the inferred NS mass and radius, has not yet been explored for appropriate atmospheres and spectra. A hot spot would harden the observed spectrum, so that spectral modeling tends to infer radii that are too small. However, a hot spot may also produce detectable pulsations.

I simulated the effects of a hot spot on the pulsed fraction and spectrum of the quiescent NSs X5 and X7 in the globular cluster 47 Tucanae using appropriate spectra and beaming for hydrogen atmosphere models, incorporating special and general relativistic effects, and sampling a range of system angles. A search for pulsations in archival Chandra HRC-S observations of two quiescent NS low-mass X-ray binaries in 47 Tuc, X5 and X7, places a 90% confidence upper limits on their pulsed fractions below 16%. These pulsation limits constrain the temperature differential of any hot

spots. I then constrain the effects of the possible hot spots on the X-ray spectrum and the inferred radius from spectral fitting. Hot spots below our pulsation limit could bias the spectroscopically inferred radius downward by up to 28%. For Cen X-4 (which has deeper published pulsation searches), an undetected hot spot could bias its inferred radius downward by up to 10%. Improving constraints on pulsations from quiescent LMXBs is essential for progress in constraining their radii.

Finally, I investigate the spectrum of a high-magnetic-field NS in a high-mass X-ray binary (HMXB). The propeller effect in accreting rotating neutron stars should cut off accretion in fast-spinning neutron star HMXBs at low mass transfer rates. However, the accretion continues in some HMXBs, as evidenced by continuing pulsations, at low luminosities. Indications of spectral softening in systems in the propeller regime suggest that some HMXBs are undergoing fundamental changes in their accretion regime. I use a 39 ks XMM-Newton observation of the transient HMXB V0332+53 at a very low X-ray luminosity to study the source of the X-ray emission in quiscence and constrain the surface temperature of the NS.

Preface

The research conducted in this thesis was done as a part of an international research collaboration, led by Professor Craig Heinke at the University of Alberta.

Chapter 2 is a work that has been conducted with C. Heinek, G. Sivakoff, W. Ho, P. Shternin, D. Yakovlev, D. Patnaude and L. David. This work has been published at the Astrophysical Journal, Volume 777, Issue 1, article id. 22, 10 pp, in 2013.

The contents of Chapters 3 and 4 are have been published in the Astrophysical Journal, Volume 826, Issue 2, article id. 162, 13 pp.. The work has been done with Heinke C., Morsink S., Bogdanov S., Stevense A. In chapter 3, I describe the background for hot spots on neutron stars, our model of hot spot emission from a neutron star, the results on pulsed fractions, and application to searches for pulsations from specific objects. Chapter 4 gives the background for work determining the neutron star radius, describes our model for calculating the effect of hot spots on the spectrum of a neutron star, calculates the limits that can be placed on the bias created by hot spots on radius measurements via spectral fitting, and summarizes caveats to our analysis.

Chapter 5 is work that has been published in the Monthly Notices of the Royal Astronomical Society in Volume 463, Issue 1, p.78-83. It has been conducted in collaboration with R. Chouinard.

Dedications

To my Family

"Two roads diverged in a wood, and I –

I took the one less traveled by,

And that has made all the difference."

– Robert Frost (1874 – 1963)

Acknowledgements

Acronyms

- **NS:** Neutron Star

- **LMXB:** Low Mass X-ray Binary

- **qLMXB:** Quiescent Low Mass X-ray Binary

- **HMXB:** High Mass X-ray Binary

- **ACIS:** Advanced CCD Imaging Spectrometer

- **HRC:** High Resolution Camera

- **EOS:** Equation of State

- **EPIC:** European Photon Imaging Camera

- **OM:** Optical Monitor

- **HRMA:** High Resolution Mirror Assembly

- **MCP:** microchannel plate

- **CALDB:** Calibration Database

- **Cas A:** Cassiopeia A

- **SNR:** Supernova Remnant

- **CCO:** Central Compact Object

- **QE:** quantum efficiency

- **CTI:** Charge Transfer Inefficiency

- **CXC:** Chandra X-ray Center

- **PF:** Pulsed Fraction

- **RMF:** Redistribution Matrix File

- **APR:** Akmal-Pahdharipande PRavenhall

- **PRE:** Photospheric Radius Expansion

Table of Contents

List of Tables

List of Figures

Chapter 1

Introduction

1.1 Neutron Stars

Stars remain at hydrostatic equilibrium due to the balance between the outward radiation pressure (as a result of nuclear fusion of lighter elements to heavier elements) and the inward gravitational force. Stars that are $\gtrsim 8\ M_\odot$ can start fusing elements beyond CO in their cores, which results in an iron (^{58}Fe) core surrounded by outer layers of other heavy elements such as oxygen, neon and carbon (Pethick & Thorsson, 1995). Iron has the greatest average binding energy per nucleon. The burning of Fe in the core no longer releases energy, but requires additional energy, therefore the temperature is reduced by this burning; this acts as a feedback mechanism to curtail Fe burning, so it halts. The Fe core grows to the critical Chandrasekhar limit (M_{Ch}) and undergoes a gravitational collapse on a free-fall time scale ($\sim$ few milliseconds) (Shapiro & Teukolsky, 1983).

The core continues to collapse until it reaches the density of atomic nuclei, where the collapse stops due to neutron degenerate pressure. This generates a massive shock in the star which expels most of the stellar matter, called a supernova. The supernova produces a huge energy release of order $\times 10^{53}$ J, and luminosities of the order $\sim 10^{10} L_\odot$, taking months to fade from visibility. Although a huge amount of energy is released during supernovae, only a small fraction ($\sim 1\%$) of the energy goes to optical light, the rest of the energy goes to the kinetic energy of the explosion and

neutrino emission (*approx* 99% in form of neutrinos and $\approx$ 1% into kinetic energy). The compact remnant from such a scenario is a neutron star with a average value of $\sim$11 km radius and 1.4 $M_\odot$ and a surface temperature of $\sim$ few $10^6 - 10^7$ K (Yakovlev et al., 1999). A thin layer of lighter elements eventually settle on the surface of the NS to form a few centimeter thick atmosphere composed mainly of H, He (Pavlov et al., 1995) or C (Ho & Heinke, 2009).

1.2   Cooling of Neutron Stars

The newly born NS remains for a short time hot and opaque to neutrinos, and then quickly becomes transparent to neutrinos (Pons et al., 2001). The emission of neutrinos from the core produces an internal cooling wave from inner to the outer layers. The NS crust is initially decoupled from the core, which can take up to a hundred years to thermally relax (Lattimer et al., 1994; Gnedin et al., 2001).

During the first few hundred years, the main processes responsible for neutrino emission from the core are called Urca Processes, in which, thermally excited particles (protons and neutrons) undergo β and inverse-β decay, releasing a stream of neutrinos. Direct Urca processes (Eq. 1.1), involving only a single nucleon, are a very rapid mechanism for cooling (Lattimer et al., 1991; Prakash et al., 1992).

$$n \rightarrow p + e^- + \bar{\nu}_e \tag{1.1}$$

$$p \rightarrow n + e^+ + \nu_e \tag{1.2}$$

The direct Urca reaction can occur only if there is a high abundance of protons in the core. This is because in this case, the NS core is degenerate, therefore the only allowed particles to undergo the reaction are the ones with energies within $\sim k_B T$ of the Fermi surface, the other processes are naturally impossible because of the Pauli exclusion principle. The Fermi electron capturing by the proton will not occur, if their combined momenta is less than the neutron Fermi level due to

2

conservation of momentum. Some other types of direct Urca processes involve muons instead of electrons (Yakovlev & Pethick, 2004).

If the direct Urca process becomes impossible, there is the modified Urca process:

$$n + N \rightarrow p + N + e^- + \bar{\nu}_e \tag{1.3}$$

$$p + N \rightarrow n + N + e^+ + \nu_e \tag{1.4}$$

The modified Urca processes are different from the direct Urca with an additional nucleon N to ensure conservation of energy and momentum of the reaction. This modified Urca process is at least 6 times slower than the direct Urca process. The core composition is the main responsible (along with the crust composition) for the core temperature and the cooling scenario the neutron star will follow, particularly in the early years. The threshold density for the direct Urca process depends crucially on the equation of state of the neutron star. For the APR equation of state, the critical mass that would allow direct Urca process is $1.97 M_\odot$ (Page et al., 2011), other EOSs have different critical masses.

These Urca processes are strongly affected by the baryon superfluidity in the core (Yakovlev et al., 1999, 2001). When the core temperature drops below the critical temperature T_c, it marks the transition of a particular baryon to superfluidity. When the core superfluid transition occurs for a particular baryon, the energy gap in the energy spectrum suppresses all reactions involving this particular baryon. For example, strong superfluidity of protons would suppress all Urca processes in this scenario.

While the Urca processes are suppressed by the superfluidity in the core, the onset of superfluidity triggers another neutrino-emission process via Cooper pairing of baryons (Flowers et al., 1976). At low temperatures and high densities baryons can create Cooper pairs similar to electron Cooper pairing (Cooper, 1956). Superfluidity in the NS cores was first discussed by Migdal (1959). Below the neutron drip (where neutrons leak out from core nuclei at some threshold density) as neutrons then will become free to move, they may interact by long-range attractive interactions pairing up two neutrons together to form Cooper pairs (singlet configuration $^1S_0$, or triplet configuration $^3P_2$)

resulting in a neutron superfluid. An enhanced neutrino emission mechanism appears as a result of this which represents the annihilation of the Cooper pair and production of a neutrino-antineutrino pair : $n+n \rightarrow \nu + \bar{\nu}$. If the core has not gone through the superfluid transition, this enhanced neutrino emission process is prohibited. As the temperature of the core decreases, this process starts to occur at T_c and is eventually suppressed when the temperature drops much below T_c. This enhanced neutrino emission operates in the core as well ass the inner crust of the NS.

This cooling scenario results in a cooling curve much faster than the modified Urca processes by about two orders of magnitude, although slower than the direct Urca processes (Yakovlev & Pethick, 2004). NS cores can also have superfluid protons in the core (Kaminker et al., 2001). The critical temperature for the superfluidity transition T_c depends on the baryon species and density, and is often indicated as $T_c(\rho)$.

1.3   X-Ray Binaries

X-ray binaries are binary stars, composed of a compact object (a white dwarf, neutron star or a black hole) which acts as the accreting object due to its greater gravitational potential, and a donor star. Depending on the mass of the donor, X-ray binaries can be classified as either Low Mass X-ray Binaries (LMXBs) where the donor is a $< 1\ M_\odot$ star (usually on the main sequence), or High Mass X-ray Binaries (HMXBs) where the mass of the donor is usually $> 10\ M_\odot$. The gravitational force of the compact object tears matter from the companion star and drags the matter toward the compact object forming an accretion disk. The NS's magnetic field can also disrupt the flow of the accreting matter, forcing the matter (protons and electrons) to flow along the magnetic field lines all the way to the surface of the NS. This inflowing matter creates an anisotropic surface temperature, and as the NSs are rotating, this allows the possibility of detecting X-ray pulsations, similar to the lighthouse effect (e.g. Giacconi et al., 1971; Schreier et al., 1972; Tananbaum et al., 1972; Lamb et al., 1973; Davidsen et al., 1972).

If the compact object is NS (or a black hole), the infalling matter encounters a huge gravita-

tional potential, that accelerates it to very high velocities. The accreting matter quickly decelerates as it hits the surface of the NS and the kinetic energy is converted to heat radiated away in form of x-ray. Black holes do not have a solid surface to hit the infalling matter, however the infalling matter accelerates to very high speeds as it passes through the accretion disk, being heated to high temperatures, and thus radiating large quantities of X-rays.

1.4   Mass and Radius Measurements

One of the most intriguing unsolved questions in physics is the equation of state (EOS) of cold, supranuclear-density matter which lies in the cores of neutron stars (NSs). The equation of state for the NS describes how the pressure relates to density and temperature (and other thermodynamic variables). The behavior of matter at extremely high densities is not well understood, which puts a big uncertainty on the NS EOS. The difficulty in calculating NS EOS models is when the density becomes too high, exceeding the nuclear saturation density $\rho_c \sim 10^{14}$ g cm^{-3}, where the relation between the pressure and the energy density is not well known (Lattimer & Prakash, 2007).

The EOS of neutron stars generates a relation between mass and radius ($M(R)$) by solving the Tolman-Oppenheimer-Volkoff equation (Oppenheimer & Volkoff, 1939). There are generally three main categories of the NS EOS, which can be generally expressed as normal, soft and stiff.

At densities on the scale of nuclear saturation density ρ_c, nuceli dissolve and merge to form nuclear matter, where neutrons dominate the support of the pressure against collapse by neutron degeneracy, and protons and electrons make up a small fraction. This can be classified as the "normal" category of EOS, where relativistic corrections on the nucleon-nucelon interactions are included (Lattimer & Prakash, 2001). Examples of this family of EOS are APR (Akmal & Pandharipande, 1997), ENG (Engvik et al., 1996), MS0 and MS2 (Müller & Serot, 1996) and LS (Lattimer et al., 1991).

The second type is "soft" EOSs, considering significant amounts of softening for matter at
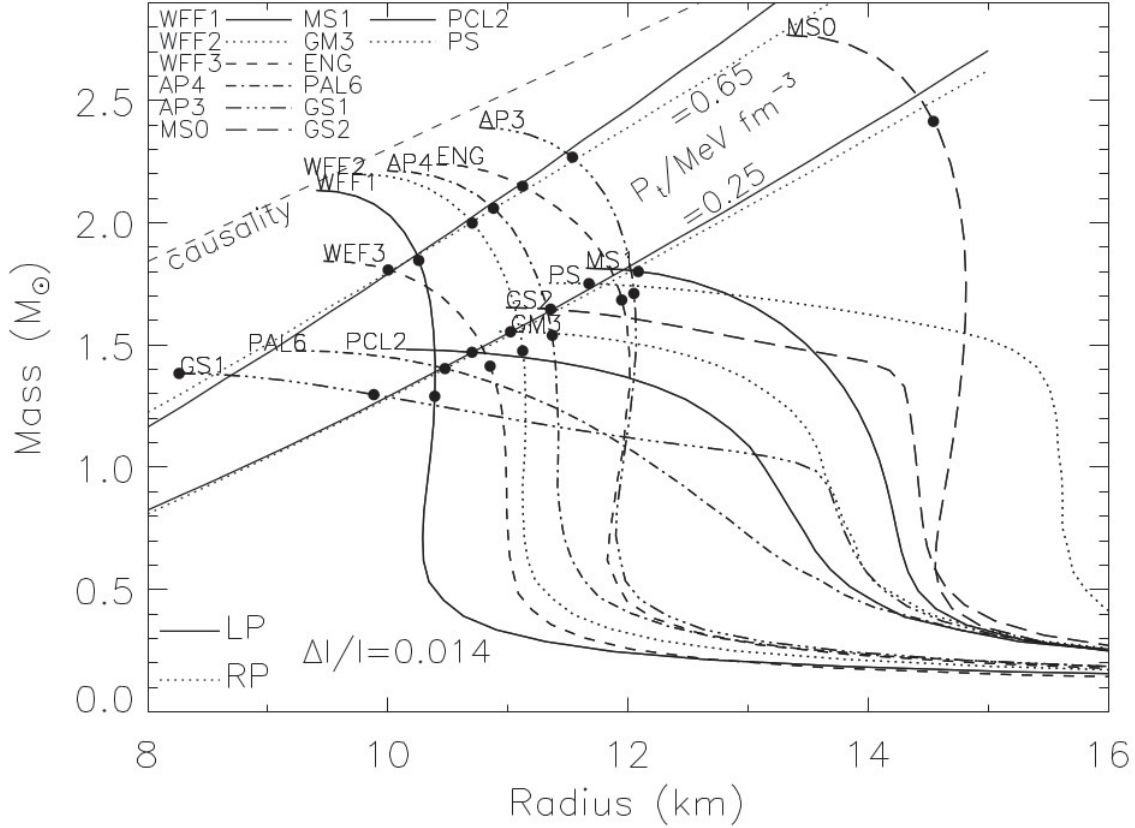
Figure 1.1: The mass-radius relations for some different equations of state. This figure is taken from Lattimer & Prakash (2001).

high densities. This treatment considers phase transitions of matter at some critical high densities, permitting an additional component such as quark, hadronic, kaon condensate (Glendenning & Schaffner-Bielich, 1998) or hyperons (Glendenning & Moszkowski, 1991) at the center of the NS. Such phase transitions result in less pressure in the core, which result in a more compact NS. The phase transitions typically allow a relatively low upper limit (e.g. 1.7 $M_\odot$) on the mass of the NS before it collapses to form a black hole, though a few exceptions exist. Examples of this type of EOSs are MS1 (Müller & Serot, 1996), FSU (Shen et al., 2010), GM3 (Glendenning & Moszkowski, 1991) and PAL6 (Prakash et al., 1988).

The third type is "strange" EOSs, where their essential assumption is that matter in its ground state is made of stange quarks. One of the important consequences of this assumption is that the pressure can be equal to zero at non-zero density, which differentiates this type from the normal

and soft EOSs. This also makes the relation between the NS mass and radius different from the other types, as the radius increases as the mass increases (Prakash et al., 1995). Fig. 1.1 shows the relation between M and R for different equations of state.

Since each proposed EOS allows a limited range of values for the NS mass M and radius R, accurate measurements of M and R can be used to constrain the NS EOS (see for reviews: Lattimer & Prakash, 2007; Hebeler et al., 2013; Özel, 2013; Lattimer & Prakash, 2016; Haensel et al., 2016; Steiner et al., 2016). While it is possible, in some cases, to obtain accurate NS mass measurements (e.g. Demorest et al., 2010; Freire et al., 2011; Antoniadis et al., 2013; Ransom et al., 2014), it is difficult to determine the NS radius.

A rapidly rotating neutron star with strong magnetic field accelerates electrons along its magnetic field lines, which radiate coherently producing radio emission. As the NS rotates, it acts as a light-house, and appears as a radio pulsar. When this radio beam passes along our line of sight, it provides an extremely useful clock. Timing observations of these systems provide an extremely precise method for measuring the five Keplerian parameters of a two orbiting bodies (orbital period, inclination, eccentricity, the time and longitude of the peri-astron) (Manchester & Lyne, 1977), which are related to the compact object and its companion masses by the mass function. General relativistic effects (post-Keplerian) correction parameters can be applied to these equations (Damour & Deruelle, 1986; Damour et al., 1992), which along with the mass function, can be used to put tight constraints on the masses (Freire et al., 2011; Antoniadis et al., 2013; Ransom et al., 2014).

One specific relativistic method of measuring the mass of the neutron star is via Shapiro delay, which is a delay in the light travel time as light passes in the spacetime near a massive object. It is one of the tests used to test general relativity. If the binary system has a high inclination angle, one can observe the delay in the pulse arrival time when the pulsating neutron star is behind its companion. General relativity predicts that in this case, the pulse will undergo a delay that depends on the companion mass and inclination angle of the orbit. The Shapiro delay can be used with the observed Keplerian mass function, to find a precise direct measurement of the neutron star mass.

For instance, the neutron star PSR J1614-2230 was measured to be $1.94 \pm 0.04\ M_\odot$ (Demorest et al., 2010), and many other NSs have extremely accurate mass measurements via this method.

Accreting neutron stars in binary systems can also undergo long episodes of small (or no) accretion, which is called quiescence. This allows us to glimpse the direct emission from the neutron star's surface. One can measure the temperature and the flux during such quiescent episodes and, assuming a low magnetic field ($< 10^9$ G, low enough to avoid detectable spectral effects) and simple light element atmospheres, One can put tight constraints on the NS radius. This method is particularly effective for X-ray binary systems in globular clusters, where the distance is well constrained (Rutledge et al., 2002b; Heinke et al., 2006; Webb & Barret, 2007; Guillot et al., 2011). However, many radius measurements are not consistent with each other which may be due to problems with instruments (Heinke et al., 2006), and/or variations in the composition of the atmosphere of neutron stars (Servillat et al., 2012).

Another way to constrain the radius is to limit the ratio M/R by modeling an observed pulse profile of a rotating neutron star. The emitted flux from a hot spot on the neutron star is strongly affected by gravitational lensing; the more compact the star is, the larger the effects of gravitational bending on the emitted light and the more the pulse is suppressed, producing a smoother pulse. From this method, the neutron star PSR J0030+0451 gives a constraint on the radius > 10.4 km at 99% confidence level (Bogdanov & Grindlay, 2009), while PSR J0437-4715 gives a radius constraint >11.1 km (Bogdanov 2013, but cf. Guillot et al. 2015 for caveats).

1.5 X-ray Missions

I will briefly cover the X-ray missions used to observe and collect data for this thesis.

1.5.1 XMM-NEWTON

The X-ray Multi-Mirror Mission was launched on December 10, 1999 by the European Space Agency. It carries the European Photon Imaging Camera (EPIC) which observes X-rays in the

range 0.2-12 keV, and covers a field of view of $\sim 30'$ at moderate spectral resolution. EPIC consists of three CCD cameras; two MOS cameras and one pn camera. High-resolution spectral information ($E/\delta E \sim 300$) for energy range between 0.4-2.5 keV) can be acquired by the Reflection Grating Spectrometer (RGS) for bright sources. XMM-NEWTON is also equipped with a 30 cm optical/UV telescope; the Optical Monitor (OM).

1.5.2 Chandra X-Ray Observatory

The Chandra X-ray observatory was launched in 1999 by the USA's NASA. The superior power of *Chandra* is its higher angular resolution (half of the power from a point source within a radius of 0.5"). Chandra's High Resolution Mirror Assembly (HRMA) is four pairs of thin-walled nested concentric paraboloid mirrors that focus the X-rays to the detectors. There are two main detectors on *Chandra* ; the Advanced CCD Imaging Spectrometer (ACIS) and the High Resolution Camera (HRC) .

The ACIS detector consists of 10 planar CCDs, each one 1024×1024 pixels, covering an ($8' \times 8'$) field of view. An array of four of these (2×2) is called ACIS-I which is optimized for imaging. ACIS-I covers a 16×16 arc minutes field of view, with chips tilted to match the Chandra focal surface. The other six CCDs, called ACIS-S, are arranged in a 1×6 array optimized for readout from the transmission grating to obtain high resolution spectra. The ACIS detector has an energy resolution as low as 95 eV at 1.49 keV. The ACIS detector energy range covers between 0.08 to 10.0 keV.

HRC is a microchannel plate (MCP) detector on *Chandra*. HRC has very good spatial resolution ($\sim 0.4''$), slightly better than ACIS due to their $0.1''$ pixel size, so the angular resolution is set by the mirrors. The HRC detector has also a time resolution 16μs, enabling sensitive searches for pulsations at millisecond periods in crowded regions. The HRC detector has a sensitivity peak at lower energies than the energy range of ACIS (HRC has a full energy range of 0.06-10 keV), but has a poor energy resolution, $E/\delta E \sim 1$ at 1 keV. HRC contains two detector arrays. HRC-I is optimized for imaging with the largest field of view on *Chandra*, $30' \times 30'$. HRC-S is optimized

to read out a spectrum spread out by the low energy transmission grating, and has a $9' \times 9'$ field of view. HRC-S is optimized for fast pulsation searches, a1lthough it has a relatively high background.

Chapter 2

Measuring the Cooling of the Neutron Star in Cassiopeia A with all *Chandra X-ray Observatory* Detectors

2.1   Forward

The work presented in this chapter has been published in the Astrophysical Journal, Volume 777, Issue 1, article id. 22, 10 pp. (2013).

The work presented in this chapter has been partly presented in my Master of Science degree in 2012. Several key results were not included at the time, which I present here.

The previous work used the instrument calibration database (CALDB) v4.4.6 for the reduction and analysis of the data from the HRC-S, HRC-I, ACIS-I and ACIS-S Faint observations and did not include any analysis of the ACIS-S Graded observations. It also only reported the results from each of the four instruments separately, without calculating the systematic errors. Finally, it did not include the theoretical implications of the results for the superfluidity in the core of the Cas A NS.

The work presented in this chapter include the following new advancements over the previous work:

- Analysis of all *Chandra* ACIS-S Graded observations between 2010 and 2013, using four different extraction regions for the source and the background. It also uses the upgraded instrument calibration database (CALDB) 4.5.5.1. This work is different from Heinke et al. (2009) which did not include analysis of the 2013 observation, did not include four different extraction regions, and did not use the newly upgraded CALDB (section 2.4.2).

- Re-analysing the HRC-S, HRC-I, ACIS-I, and ACIS-S Faint data using CALDB 4.5.5.1. The analysis for ACIS-I observations was improved to merge observations taken close togther, and exclude other observations with high off-axis angles (sections 2.4.1, 2.4.3).

- Calculating the combined measured cooling rate using all the instruments together, including statistical errors and systematic errors based on a weighted fit of the temperature declines inferred by the various detectors (section 2.4.4).

- Theoretical intepretation of the minimal cooling for measurements as low as 1% as reported from HRC-S, and the illustrations of the results on the theoretical cooling curves and the NS EOS (section 2.5).

2.2 Introduction

Young neutron stars (NSs) cool primarily through neutrino emission from their cores, allowing studies of NS thermal evolution to probe the physics of dense matter (see Yakovlev & Pethick, 2004; Page et al., 2006; Tsuruta, 1998, for reviews). Many young NSs are known, and their ages and temperatures can be estimated, allowing studies of NS cooling curves (e.g. Yakovlev et al., 2011; Page et al., 2009; Tsuruta et al., 2009). However, accurately measuring the current temperature decline rate in a young NS can provide significantly clearer information about the interior physics of NSs.

The NS at the center of the Cassiopeia A (Cas A) supernova remnant, 3.4 kpc away (Reed et al., 1995), was discovered by *Chandra* in 1999 (Tananbaum, 1999). The age of the supernova remnant is estimated to be ≈ 330 years (Fesen et al., 2006). This NS shows no evidence for X-ray pulsations, despite repeated searches using *XMM-Newton* and multiple *Chandra* detectors, culminating in a long 2009 *Chandra* HRC-S time series (Murray et al., 2002; Mereghetti et al., 2002; Pavlov & Luna, 2009; Halpern & Gotthelf, 2010). The Cas A NS has not been detected in radio imaging surveys, nor radio pulsation searches (McLaughlin et al., 2001), shows no optical or infrared counterpart (Fesen et al., 2006; Wang et al., 2007), and shows no evidence of an extended X-ray pulsar wind nebula (Pavlov & Luna, 2009). The soft X-ray spectrum, X-ray luminosity, and lack of multiwavelength counterparts or any evidence of radio pulsar activity make the Cas A NS similar to nine other central X-ray sources, presumably NSs, in young supernova remnants, the so-called Central Compact Objects (see Ho, 2013; Gotthelf et al., 2013, for reviews). The normalization of the soft blackbody-like X-ray spectrum requires either tiny hot spots on the NS surface (difficult to understand, given the tight pulsation limits; Pavlov & Luna, 2009) or an atmosphere of carbon (Ho & Heinke, 2009). The latter model fits the spectrum well, and can be explained by the burning and removal of light elements on the surface of the NS on a timescale $\lesssim 100$ years (Chang et al., 2010).

Heinke & Ho (2010) reported a $3.6 \pm 0.6\%$ relative decay ratio (T_{2000}/T_{2009}) in surface temperature over 9 years using a series of archival *Chandra* ACIS-S Graded observations, extended by

Shternin et al. (2011) to a tenth year. This decline is significantly steeper than can be explained by the modified Urca mechanism (Yakovlev et al., 2011). The rapid decline but relatively high temperature require a recent, dramatic change in the neutrino emission properties of the NS. Page et al. (2011) and Shternin et al. (2011) interpret this change as due to the transition of the neutrons in the core to a superfluid state, during which the pairing of neutrons produces enhanced neutrino emission (Flowers et al., 1976; Page et al., 2004; Gusakov et al., 2004). This identification allows the measurement of the critical temperature for core neutron superfluidity, around $(5-8)\times10^8$ K (Page et al., 2011; Shternin et al., 2011). This interpretation also requires core proton superfluidity, with critical temperature T_c above 10^9 K. Verifying this temperature decay is thus of great importance for the physics of high density nuclear matter.

However, even the best-calibrated detectors on *Chandra*, the ACIS imaging detectors, suffer from a few problems that could affect the reliability of the temperature decline measurement. An obvious problem is the decline in quantum efficiency (QE) due to the buildup of a molecular contaminant on the CCDs[1], which mimics a declining count rate and inferred temperature. However, this decline is strongest at low (< 0.7 keV) energies, and has been well-studied and calibrated. Heinke & Ho (2010) showed that the flux decline from the Cas A NS is slightly stronger at higher, rather than lower, energies, which is inconsistent with this QE decline. Another problem that affects observed count rates is Charge Transfer Inefficiency (CTI), where a fraction of the charge released by an X-ray photon is lost as the electrons transfer from one pixel to another on the CCD during the readout time of the detector (Townsley et al., 2000), causing an alteration of the measured energy of the photon. Event pileup, where the detector identifies two photons landing on the same or adjacent pixels within one frame time as a single photon, can cause both a lower count rate and a higher recorded energy for each photon (Davis, 2001). Both CTI and pileup can cause grade migration, where the pattern of released electrons on the detector is altered from a pattern typical of a single photon (denoted a "good" grade) to a pattern atypical of single photons (a "bad" grade, commonly produced by cosmic rays). Since Graded mode observations do not telemeter the 3×3

---

[1]http://cxc.harvard.edu/cal/Acis/Cal_prods/qeDeg

or 5×5 charge distribution around each event to the ground, the effects of CTI cannot be corrected with the standard procedure.

Since ACIS data provided in Graded mode omits some data classified with "bad" grades from the *Chandra* telemetry stream, any increased rates of grade migration can lead to a (previously uncalibrated) decrease in count rate for Graded mode data over the *Chandra* lifetime. Robert Rutledge reported[2] that the ACIS-S detector, when operating in Graded mode, has indeed suffered increasing rates of grade migration during the past ten years, due to radiation damage on the ACIS CCDs causing increased CTI. This effect has been confirmed by the *Chandra* X-ray Center (CXC) and new calibrations were generated to correct for this effect. Since Cas A is a very bright X-ray source, most ACIS data on it has been taken in Graded mode. Given that this calibration update was unavailable for the Heinke & Ho (2010) analysis, this problem could affect their Cas A NS temperature decline measurement.

Since it is premature to conclude that there are no other systematic uncertainties affecting the temperature decline measurement, our goal in this paper is to measure the temperature change of the Cas A NS over 10 years using updated calibrations and archival data from all of the imaging detectors on *Chandra*; HRC-S, HRC-I, ACIS-I, ACIS-S (Faint mode), and ACIS-S (Graded mode, including a new 2012 observation). The HRC cameras use a completely different detector system (a multichannel plate) than the ACIS CCDs, and they should not suffer the same systematic detector uncertainties (though they may have other problems). While we cannot expect that the different detectors are cross-calibrated at the sensitivity necessary to directly compare the measured temperatures between detectors, the fractional temperature gradient (in time) for each detector should be more robust. In all our analysis, the decline rate is calculated using a best-fit line according to

$$\text{decay}\,[\%] = \left(1 - \frac{a\,y_f + b}{a\,y_i + b}\right) \times 100, \tag{2.1}$$

where $y_i = 2000$ and $y_f = 2010$. All errors presented throughout the paper enclose the 1σ confidence interval.

---

[2]Talk at the Institute for Nuclear Theory conference on astrophysical transients, `http://www.int.washington.edu/PROGRAMS/11-2b/`

2.3   X-ray Analysis

Our analysis was conducted using the *Chandra* Interactive Analysis of Observations (CIAO) 4.4 software along with the *Chandra* Calibration Database (CALDB) 4.4.6 for analyzing HRC-S and HRC-I observations, omitting the few observations taken using gratings. Although there was an update to the HRC-S QE in CALDB 4.4.7, this only affected the QE below 0.1 keV, which does not affect the analysis of the highly absorbed central compact source in Cas A. For ACIS-I, ACIS-S in Faint mode, and ACIS-S in Graded mode observations, I use CIAO 4.5 and CALDB 4.5.5.1. The CXC calibration team released this calibration update to correct ACIS-S Graded observations for the grade migration problem described above.

Below I describe details of the analysis for each detector.

2.3.1   HRC-S

The Cas A supernova remnant was observed by the *Chandra* HRC-S camera in 1999 September, 2000 October, and 2001 September, and then in five long exposures in 2009 March. Three other HRC-S observations were not analyzed because the supernova remnant is at very large offset angles, and thus strongly out of focus. In all the remaining HRC-S observations, the Cas A NS is projected relatively close to the aimpoint, in a region on the chip that is relatively well calibrated. Table 2.1 lists the ObsIDs considered in our analysis, with their exposures. The HRC-S data are good candidates to compare with the ACIS-S observations, since the HRC-S observations place the NS near the optical axis of the telescope (i.e., at small off-axis angles of $\theta_{\text{off-axis}} < 1'$); this avoids the blurring of the point-spread function incurred at large off-axis angles[3].

Most importantly — apart from ObsID 172 in 1999 which was only 9.5 ks — these are deep observations of 50–130 ks, providing sufficient statistics for a clear result. Since ObsIDs 10227, 10228, 10229, 10698, and 10892 were taken within ten days in 2009, their calibration should be identical. I therefore merged them into a single observation for the purposes of this analysis. I used

---

[3]Chandra Proposer's Observatory Guide, `http://cxc.harvard.edu/proposer/POG/`

ObsID	Year	Exposure [ks]	$\theta_{\text{off-axis}}$ [']	Case I[a] Count Rate [$10^{-2}\,\text{cnt}\,\text{s}^{-1}$]	T_{eff} [$10^6\,\text{K}$]	Case II Count Rate [$10^{-2}\,\text{cnt}\,\text{s}^{-1}$]	T_{eff} [$10^6\,\text{K}$]	Case III Count Rate [$10^{-2}\,\text{cnt}\,\text{s}^{-1}$]	T_{eff} [$10^6\,\text{K}$]	Case IV Count Rate [$10^{-2}\,\text{cnt}\,\text{s}^{-1}$]	T_{eff} [$10^6\,\text{K}$]
172	1999.68	9.4	0.7	2.83±0.19	2.006±0.025	2.71±0.18	1.990±0.024	3.00±0.22	2.028±0.028	3.14±0.22	2.046±0.027
1857	2000.76	48.4	0.3	3.01±0.09	2.032±0.011	2.93±0.08	2.022±0.010	3.14±0.09	2.048±0.011	3.19±0.10	2.054±0.011
1038	2001.80	50.0	0.2	2.84±0.08	2.013±0.011	2.74±0.08	2.000±0.010	2.96±0.09	2.028±0.011	3.07±0.09	2.042±0.011
Merged[b]	2009.23	484.4	0.3	2.60±0.06	2.005±0.008	2.53±0.05	1.994±0.007	2.60±0.06	2.004±0.008	2.69±0.06	2.017±0.008

Table 2.1: The different cases represent different choices of source and background regions:

Case I — $r_{\text{src}} = 1.97''$, $r_{\text{bkg}} = 2.5''$–$3.9''$

Case II — $r_{\text{src}} = 1.3''$, $r_{\text{bkg}} = 2''$–$3.3''$

Case III — $r_{\text{src}} = 3''$, $r_{\text{bkg}} = 5''$–$8''$

Case IV — $r_{\text{src}} = 3''$, $r_{\text{bkg}} = 5''$–$8''$ excluding filaments.

[a]This case is our preferred case for cross-detector comparison.

[b]The merged 2009 observations consist of ObsIDs 10227, 10228, 10229,10698 and 10892.

the processed event-2 files from the public *Chandra* Observation Catalogue[4].

Since the spectral energy resolution of HRC-S is poor, no significant spectral information can be extracted from HRC-S observations. Therefore, for each observation, I calculate a table of conversion factors between the observed count rate and the NS temperature, using a simulated spectrum and the relevant response. Then I use the observed count rates to calculate the NS temperature at each epoch. Our model for the Cas A NS spectrum utilizes the best fit values from the ACIS-S spectral fitting (Shternin et al., 2011); this includes a non-magnetized carbon atmosphere (Ho & Heinke, 2009), scattering of soft X-rays by interstellar dust (Predehl et al., 2003), and the Tuebingen-Boulder model for photoelectric absorption by interstellar gas and dust (Wilms et al. 2000, including its updated solar abundances, with cross-sections from Balucinska-Church & Mc-Cammon 1992). I allow only the temperature of the NS to vary (as physically expected), fixing the other parameters at the values used in Shternin et al. (2011); distance of $d = 3.4$ kpc, radius of $R_{NS} = 10.19$ km, mass of $M_{NS} = 1.62\,M_{\odot}$, and interstellar absorption $N_H = 1.734 \times 10^{22}$ cm^{-2}. I note that the best-fit N_H from the carbon-atmosphere fits is more consistent with the estimated N_H at positions near the NS from spectral fits of the remnant (between 1.7–2.0$\times 10^{22}$ cm^{-2}, Hwang & Laming, 2012, U. Hwang 2013, priv. comm.) than the estimates using a hydrogen atmosphere (best fit $N_H \sim 1.6 \times 10^{22}$ cm^{-2}, Pavlov & Luna, 2009) or a blackbody ($N_H = 1.2$–1.4×10^{22} cm^{-2}, Pavlov & Luna, 2009).

The effective area file, or ARF, has been generated for each HRC-S observation using the CIAO tool mkarf. In real-world detectors, incident photons at any given energy will be detected as events at a range of measured energies (technically, the detector pulse height amplitude), a process that is expressed as a matrix multiplication through a Redistribution Matrix File (RMF). The poor spectral resolution of HRC-S means that this matrix has very substantial terms far off the diagonal. I used a simple RMF for HRC-S that was released by the CXC in 2010; however, since I use the total count rate of HRC data, rather than attempting detailed spectral fitting, the choice of RMF is not likely to have a strong impact. I combined the calibration files and models described above in XSPEC

---

[4]http://cda.harvard.edu/chaser/

v. 12.7.0 (Arnaud, 1996) to create a table of temperatures corresponding to different count rates for each epoch. Through this, I matched *real* measured count rates to model-predicted count rates within $< 1\%$, to calculate the temperature for each HRC-S observation.

Deep ACIS-S observations of the sky area around the Cas A NS reveal strong variability of nonthermal X-ray filaments of the supernova remnant over time (Patnaude & Fesen, 2009). Some of these filaments cross the NS from our perspective. Variability in the portion of the filamentary structure lying across the NS need not correlate with neighboring parts of the filament. Since these latter regions potentially contaminate the local background region used in analyzing the NS, differential variability of filaments in the supernova remnant may lead to a mis-measurement of the count rate/temperature for the NS; a brightening of filaments in the background region could cause an overestimated decrease in the NS count rate. I attempted to constrain the behavior of this filament by making images of the area around the NS in hard energy bands: 5–6 keV, 5–7 keV, and 7–8 keV. However, pile up from the NS still contributed counts in these bands, making the behaviour of the filaments across the NS difficult to determine. I tentatively assume that the portion of the filament crossing over the NS has the same average surface brightness as nearby filaments.

To address systematic errors due to the filaments on the measured count rates and the inferred temperatures, I considered several choices of source and background extraction regions. For consistency with past analyses, our default source extraction region (hereafter, Case I) matches the circular region ($r_{\mathrm{src}} = 1.97''$) considered by Pavlov & Luna (2009) and Heinke & Ho (2010)[5]. For this case, I chose a background annulus of radii $2.5''$–$3.9''$. I pair a more compact region (Case II), which corresponds to the smallest region that encloses 90% of the flux from a point source ($r_{\mathrm{src}} = 1.3''$, 10 HRC pixels), with a background annulus of radii $2''$–$3.3''$. A larger set of regions was also considered (Case III, $r_{\mathrm{src}} = 3''$, $r_{\mathrm{bkg}} = 5''$–$8''$). Because the larger background region extends further away from the NS, it includes brighter, more highly variable filaments, which likely increase our systematic uncertainties. Therefore, for our largest source aperture, I created a second

---

[5]Note that Heinke & Ho (2010) say they used a 4-pixel extraction region, corresponding to $2.37''$; the 4-pixel radius is correct, but this corresponds to $1.97''$.
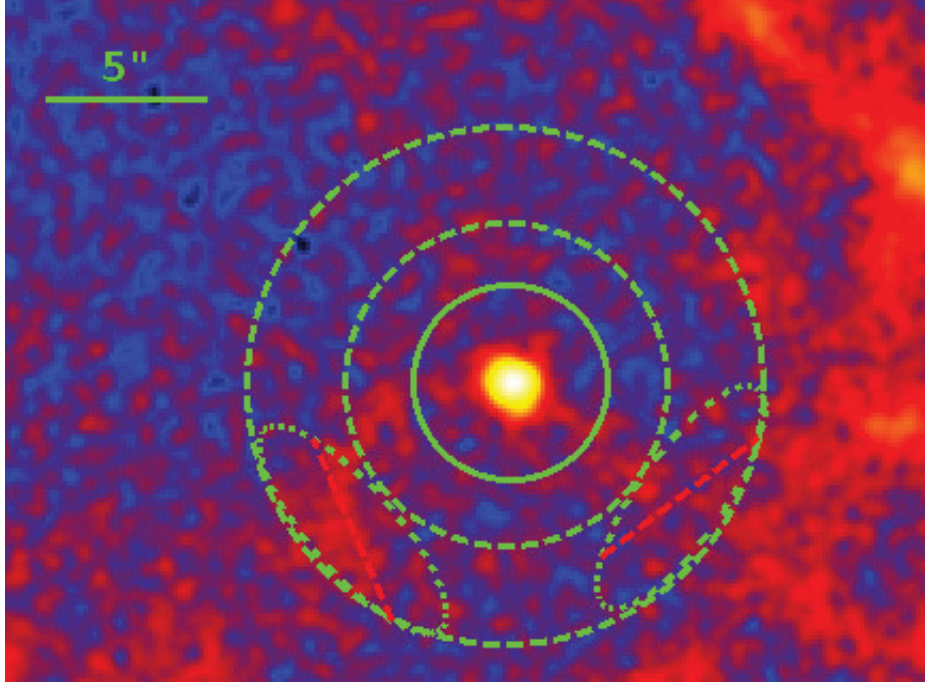
Figure 2.1: Image of the Cas A NS taken with the HRC-S detector (ObsID 10227), showing the circular
source extraction region (solid line) and annular background extraction region (dashed lines) for
our Case IV. Clear filaments are visible, and are excluded (short dashed lines) in Case IV.

background region, which potentially minimizes the effects of bright filaments. In this Case IV,
the regions showing bright filaments in some observations were excluded in all observations (see
Figure 2.1). Table 2.1 gives the measured count rates and effective temperatures for the HRC-S
observations.

2.3.2   ACIS-S, Graded mode

I analyzed all the ACIS-S Graded observations between 2000 and 2012, excluding observations
where bad columns intersected the Cas A NS (see discussion in Heinke & Ho, 2010). Prior to
2005, the ACIS-S Graded observations were taken with a 3.24 s frame time. Since then, only one
ACIS-S chip has been turned on during the observations, leading to a 3.04 s frame time. Since three
sets of two observations (10935/12020, 10936/13177, and 9117/10773) were each taken very close
together in time and with the same instrument setup, each of these three sets were merged together.

I also analyze the recent deep (~ 50 ks) ObsID 14229 taken in 2012 May. I note that several ACIS-S (and ACIS-I) ObsIDs suffer from telemetry saturation, with some dropped frames. The reduction in exposure is accounted for in standard processing (via the "good time intervals"), and there is no evidence that the temperature measurements from these ObsIDs are biased compared to other ObsIDs.

I fit spectra of the ACIS-S Graded data to measure the NS surface temperature. To allow consistent comparisons with the previous results using this detector, I first extracted spectra from the same regions (our Case I) used in Heinke & Ho (2010) and Shternin et al. (2011). After generating the appropriate ARF and RMF files for each observation, I binned the extracted spectra at a minimum of 25 counts per bin. I adopted the same fitting parameters as in Shternin et al. (2011, and as above) for the neutron star M_{NS}, R_{NS}, and N_H. The fits to the extracted ACIS-S spectra also account for the effects of pileup through the pileup model implemented in XSPEC (Davis, 2001). I fixed the grade migration parameter for pileup to $\alpha = 0.27$ for the 3.24 s frame time observations and $\alpha = 0.24$ for the 3.04 s frame time observations (the best-fit found by Heinke & Ho, 2010). The maximum number of photons is fixed to 5 and the PSF fraction is set to 0.95 for all observations. The temperatures for Case I are summarized in Table 2.2. To determine if the ACIS camera suffered from a different systematic error due to the choice of regions, I followed the same procedure for Cases II – IV.

2.3.3 HRC-I

Nineteen observations of Cas A were made using HRC-I, all of them on-axis ($\theta_{off-axis} < 1'$), spaced between 2001 and 2011. However, with the exception of ObsID 11240 and ObsID 12059, which have ~ 13 ks exposures, most of the HRC-I observations are only ~ 5 ks long. I used the same analysis method as in the HRC-S analysis, using the HRC-I response matrix (hrciD1999-07-22rmfN0002.fits) generated by the CXC in 2009 December. The proper ARF files were computed for each observation using mkarf, and used together with the RMF to simulate HRC-I spectra and determine the count rate-temperature conversion. I only report the results from Case I, though I

ObsID	Year	Exposure [ks]	$\theta_{\text{off–axis}}$ [']	Count Rate $[10^{-2}\,\text{cnt}\,\text{s}^{-1}]$	T_{eff} $[10^6\,\text{K}]$
114	2000.08	49.9	1.9	9.99 ± 0.15	$2.145^{+0.009}_{-0.008}$
1952	2002.10	49.6	1.9	9.72 ± 0.15	$2.142^{+0.009}_{-0.008}$
5196	2004.11	49.5	1.9	9.36 ± 0.15	$2.118^{+0.011}_{-0.007}$
9117 , 09773[a]	2007.93	49.7	1.9	8.89 ± 0.14	$2.095^{+0.007}_{-0.010}$
10935, 12020[a]	2009.84	49.6	1.9	8.57 ± 0.14	$2.080^{+0.009}_{-0.008}$
10936, 13177[a]	2010.83	49.5	1.9	8.42 ± 0.14	$2.070^{+0.009}_{-0.009}$
14229	2012.37	49.1	2.4	6.87 ± 0.14	$2.050^{+0.009}_{-0.008}$

Table 2.2: ACIS-S (Graded Mode) Count Rates and Temperatures of the Cas A NS.

[a] The two listed ObsIDs, which were taken very close together in time with the same instrument setup, were merged prior to spectral analysis.

also computed Case II and found similar results. Table 2.3 gives the ObsIDs, exposures, off-axis angles, count rates, and inferred temperatures of the HRC-I data.

2.3.4   ACIS-I

All observations using the ACIS-I detector were analysed. Although these are more frequent, with 23 ACIS-I observations between 2000 and 2009, they are very shallow, with an average exposure of 1.7 ks. All ACIS-I observations were taken with a 3.24 s frame time, except ObsID 10624, which has a 3.04 s frame time. The Cas A NS was projected onto the I3 chip for all observations, except for ObsID 223, which used the I0 chip, ObsID 224, which used the I1 chip, and ObsID 225, which used the I2 chip.

The ACIS-I observations have several potential sources of systematic errors beyond those affecting the other detectors. Since the majority of the ACIS-I observations aimed to study the supernova remnant, as opposed to the NS, these observations tend to place the whole supernova remnant on the center of a CCD chip. Given that the the aim point of the ACIS-I detector is at the corner of

ObsID	Year	Exposure [ks]	$\theta_{\text{off}-\text{axis}}$ [']	Count Rate $[10^{-2}\,\text{cnt}\,\text{s}^{-1}]$	T_{eff} $[10^6\,\text{K}]$
01549	2001.04	4.9	0.1	3.24 ± 0.26	2.110 ± 0.030
01550	2001.53	4.8	0.5	2.93 ± 0.25	2.070 ± 0.031
02871	2002.10	4.9	0.0	2.95 ± 0.25	2.066 ± 0.031
02878	2002.66	1.5	0.6	2.32 ± 0.39	1.960 ± 0.070
03698	2003.20	5.0	0.2	2.22 ± 0.21	1.957 ± 0.032
03705	2003.80	5.0	0.5	2.74 ± 0.23	2.035 ± 0.031
05164	2004.23	4.8	0.2	2.82 ± 0.23	2.014 ± 0.033
05157	2004.83	5.1	0.5	2.74 ± 0.23	2.047 ± 0.031
06069	2005.80	5.1	0.3	3.26 ± 0.25	2.100 ± 0.030
06083	2005.81	5.1	0.5	3.03 ± 0.24	2.074 ± 0.031
06739	2006.22	5.0	0.2	3.10 ± 0.24	2.082 ± 0.030
06746	2006.79	5.0	0.5	2.67 ± 0.23	2.026 ± 0.032
08370	2007.18	5.0	0.1	2.66 ± 0.22	2.070 ± 0.031
09700	2008.23	5.0	0.2	3.00 ± 0.24	2.112 ± 0.030
12057	2009.95	10.9	0.2	2.73 ± 0.16	2.004 ± 0.022
12059	2009.96	12.8	0.2	2.52 ± 0.14	2.004 ± 0.020
12058	2009.96	9.2	0.2	2.69 ± 0.17	2.000 ± 0.024
11240	2009.97	12.9	0.2	2.88 ± 0.15	2.045 ± 0.020
11955	2010.27	9.5	0.3	2.95 ± 0.18	2.032 ± 0.022

Table 2.3: HRC-I Count Rates and Inferred Temperatures of the Cas A NS

the I3 chip, this places the NS at large off-axis angles. This leads to significant asymmetric smearing of the NS point-spread function, which could blend photons from the NS with emission from different parts of the supernova remnant in each observation. In addition, the different observations have different telescope roll angles that lead to different filamentary features contributing to the source and background regions. Finally, further systematic errors could be induced by uncertainties in the calibration of the response of the ACIS-I CCDs at different off-axis angles.

I used a larger source extraction region of $r_{\rm src} = 4.2''$ (8.5 ACIS pixels), to make sure that the extraction region of the source contains most of the smeared point-spread function. I extract the background from an annulus with radii $6.3''$–$12.5''$, excluding in all observations a region showing bright, variable supernova remnant filaments. This choice of extraction regions (hereafter Case V) is only considered for the ACIS-I observations.

As with the ACIS-S Graded data, extracted spectra of all observations were binned at a minimum of 25 counts per bin. The grade migration parameter of the pileup model may differ in ACIS-I compared to the ACIS-S data. I fixed $\alpha = 0.5$, the nominal best value of Davis (2001), for all our ACIS-I spectra. I note that this is higher than that used for ACIS-S data in Heinke & Ho (2010), where α was allowed to vary with a typical value $\alpha \sim 0.25$. Varying our choice of α had little effect, likely due to the lower degree of pileup in these off-axis observations. In the pileup model, the maximum number of photons is fixed to 5 and the PSF fraction to 0.95 for all observations. Table 2.4 gives the ObsIDs, exposures, off-axis angles, count rates, and temperatures for the ACIS-I data. Since ObsIDs 226 and 233–235 were taken very close together in time, were on the same chip, and had consistent temperatures, they were merged for the temperature decline analysis. To minimize systematic errors due to the ACIS-I chip used, only the observations where the Cas A NS was on the I3 chip were used for the temperature decline analysis.

2.3.5 ACIS-S, Faint Mode

Finally, ACIS-S Faint mode observations were analyzed using the same technique as used with the ACIS-S Graded and ACIS-I observations. These 19 observations are more widely distributed in

ObsID	Year	Exposure [ks]	$\theta_{\text{off-axis}}$ [']	Count Rate [$10^{-2}\,\text{cnt}\,\text{s}^{-1}$]	T_{eff} [$10^6\,\text{K}$]
Merged 2000.2 Observations[a]					
00226	2000.16	2.7	3.9	9.59 ± 0.60	2.140 ± 0.042
00233	2000.16	1.3	5.4	10.60 ± 0.92	2.201 ± 0.057
00234	2000.16	1.3	7.2	7.89 ± 0.77	2.232 ± 0.069
00235	2000.16	1.3	6.2	9.12 ± 0.83	2.248 ± 0.068
Merged	2000.16	6.6	...	9.35 ± 0.37	2.193 ± 0.060
Individual Observations					
00194	2000.38	3.4	4.3	8.03 ± 0.45	2.067 ± 0.040
01545	2001.04	1.5	3.6	6.66 ± 0.66	2.123 ± 0.054
01546	2001.53	1.4	4.0	8.22 ± 0.77	2.089 ± 0.058
02869	2002.10	1.4	3.6	6.68 ± 0.69	2.040 ± 0.062
02876	2002.66	1.4	5.4	8.21 ± 0.76	2.130 ± 0.058
03696	2003.21	1.6	5.3	8.07 ± 0.70	2.123 ± 0.057
03703	2003.79	1.5	6.2	8.19 ± 0.73	2.207 ± 0.056
05162	2004.21	1.4	5.2	7.69 ± 0.73	2.138 ± 0.059
05155	2004.82	1.6	6.2	7.26 ± 0.68	2.163 ± 0.060
06067	2005.28	1.7	5.7	9.13 ± 0.73	2.131 ± 0.054
06081	2005.80	1.7	6.2	7.70 ± 0.67	2.145 ± 0.060
06737	2006.22	1.7	5.4	6.23 ± 0.61	2.026 ± 0.054
06744	2006.78	1.7	6.2	6.26 ± 0.61	2.101 ± 0.056
08368	2007.19	1.7	5.1	5.34 ± 0.56	1.965 ± 0.064
09698	2008.23	1.8	5.4	6.67 ± 0.67	2.050 ± 0.052
10642	2009.36	1.8	5.7	6.54 ± 0.60	2.162 ± 0.050
Excluded Observations[b]					
00223	2000.16	0.8	7.6	4.94 ± 0.77	2.052 ± 0.100
00224	2000.16	1.0	6.6	5.72 ± 0.75	2.021 ± 0.080
00225	2000.16	1.0	7.2	7.23 ± 0.84	2.120 ± 0.075

Table 2.4: ACIS-I Count Rates and Temperatures of the Cas A NS.
[a] Since ObsIDs 226 and 233–235 were taken very close together in time, were on the same chip, and had consistent temperatures, they were merged for the temperature decline analysis.
[b] Since Obs IDs 223–225 were not taken on the I3 CCD, they were excluded from the temperature decline analysis.

time than the HRC-S observations, and unlike the ACIS-I observations do not suffer from large off-axis angles. Most of the ACIS-S Faint observations have $\theta_{\text{off}-\text{axis}} \sim 2.5'$, similar to the ACIS-S Graded mode observations (this centers the supernova remnant on the S3 chip). However, most of these observations have short exposures around $1\,\text{ks}$, leading to poor statistics. ObsID 6690 was taken using a 1/8 subarray mode, eliminating pileup. To ensure consistent comparison with past analyses, I exclude it from our analysis. Table 2.5 gives the ObsIDs, exposures, off-axis angles, count rates, and temperatures for the ACIS-S Faint Mode data.

ObsID	Year	Exposure [ks]	$\theta_{off-axis}$ [']	Count Rate $[10^{-2}\,\mathrm{cnt\,s^{-1}}]$	T_{eff} $[10^6\,\mathrm{K}]$
00230] 230	2000.16	2.1	2.6	10.79 ± 0.70	2.104 ± 0.040
00236] 236	2000.16	1.0	3.1	11.41 ± 1.01	2.168 ± 0.060
00237] 237	2000.16	1.0	4.4	9.75 ± 0.98	2.169 ± 0.062
00198] 198	2000.39	2.5	0.9	9.75 ± 0.62	2.095 ± 0.040
01547] 1547	2001.02	1.1	2.2	10.48 ± 0.97	2.152 ± 0.064
01548] 1548	2001.53	1.1	2.7	8.76 ± 0.89	2.051 ± 0.056
02870] 2870	2002.10	1.8	2.4	8.71 ± 0.70	2.029 ± 0.055
02877] 2877	2002.66	1.1	3.0	7.63 ± 0.83	2.025 ± 0.055
03697] 3697	2003.21	1.2	2.6	9.07 ± 0.87	2.096 ± 0.051
03704] 3704	2003.80	1.2	2.6	8.90 ± 0.86	2.087 ± 0.056
05163] 5163	2004.20	1.1	2.6	9.98 ± 0.95	2.093 ± 0.050
05156] 5156	2004.83	1.1	2.5	9.07 ± 0.91	2.095 ± 0.054
06068] 6068	2005.28	1.2	2.6	8.68 ± 0.85	2.047 ± 0.050
06082] 6082	2005.81	1.2	2.6	7.49 ± 0.79	2.064 ± 0.022
06738] 6738	2006.22	1.2	2.6	9.57 ± 0.89	2.104 ± 0.047
06745] 6745	2006.79	1.2	2.7	8.59 ± 0.85	2.056 ± 0.051
08369] 8369	2007.19	1.3	2.6	10.48 ± 0.90	2.136 ± 0.048
09699] 9699	2008.23	2.2	2.6	8.24 ± 0.20	2.034 ± 0.037
10643]10643	2009.36	1.3	2.4	9.13 ± 0.84	2.082 ± 0.047

Table 2.5: ACIS-S (Faint Mode) Count Rates and Temperatures of the Cas A NS.

2.4 Results and Discussion

2.4.1 HRC-S

Given that our source extraction regions account for the fraction of the enclosed PSF, to first order, I should expect that Cases I-IV (i.e., different source and background extraction regions) should yield consistent temperature declines. However, in the case of a spatially and temporally dependent background produced by the synchrotron emitting filaments that cross the NS and background extraction regions, the different Cases will yield different results. By comparing the decline in count rates measured by Cases I-IV, I can estimate the strength of this systematic effect.

A linear fit to the decline of the HRC-S count rate in Case I gives a count rate decline of $12.6 \pm 2.8\%$ over 10 years. Case II is not very different, where the 10-year decline is $12.2 \pm 2.8\%$. Case III gives the highest count rate decline over 10 years at $17.0 \pm 2.7\%$, while Case IV gives a slightly smaller decline of $16.3 \pm 2.7\%$. Table 2.1 summarizes all the HRC-S results for the different cases, the measured count rates, and the inferred temperatures.

The currently released calibration[6] of the QE decline for HRC-S is $0.75 \pm 0.19\% \, \mathrm{yr}^{-1}$. This suggests that the QE-corrected NS count rate decline over 10 years would range from $4.7 \pm 3.4\%$ (for Case I) to $9.5 \pm 3.4\%$ (for Case III). This leads to a real NS temperature drop of 1–2% over 10 years.

I obtain similar results when estimating the NS temperatures directly, by comparing the measured count rates with the count rates predicted for the model atmosphere in XSPEC, for different extraction cases (Table 2.1, last column). Cases I and II show marginal NS temperature declines over 10 years of $1.0 \pm 0.7\%$ and $0.9 \pm 0.6\%$, respectively. Since the $\chi^2 = 2.7$ for 2 degrees of freedom (d.o.f.) for Case II, I have rescaled its errors to give a reduced-$\chi^2 \equiv \chi^2_\nu = 1$ for comparison with other measurements; I follow the same procedure whenever $\chi^2_\nu > 1$. When using larger source and background regions, the inferred decline over 10 years increases slightly to $2.0 \pm 0.7\%$

---

[6]http://cxc.cfa.harvard.edu/cal/Hrc/Monitor/index.html

Detector	Case	Temperature Decline [% over 10 yr]	χ^2_ν
HRC-S[a]	I	$1.0 \pm 0.7_{\text{stat}} \pm 0.6^b_{\text{sys}}$	0.90
HRC-S	II	$0.9 \pm 0.6_{\text{stat}} \pm 0.0^b_{\text{sys}}$	1.4
HRC-S	III	$2.0 \pm 0.7_{\text{stat}} \pm 0.0^b_{\text{sys}}$	0.62
HRC-S	IV	$1.8 \pm 0.7_{\text{stat}} \pm 0.0^b_{\text{sys}}$	0.15
ACIS-S (Graded Mode)[a]	I	$3.5 \pm 0.4_{\text{stat}} \pm 1.0^b_{\text{sys}}$	0.39
ACIS-S (Graded Mode)	II	$3.1 \pm 0.3_{\text{stat}} \pm 0.0^b_{\text{sys}}$	0.65
ACIS-S (Graded Mode)	III	$5.0 \pm 0.4_{\text{stat}} \pm 0.0^b_{\text{sys}}$	1.4
ACIS-S (Graded Mode)	IV	$4.9 \pm 0.4_{\text{stat}} \pm 0.0^b_{\text{sys}}$	0.67
HRC-I[a]	I	$2.1 \pm 1.0_{\text{stat}} \pm 0.0^b_{\text{sys}}$	2.2
ACIS-I[a]	V	$2.6 \pm 1.9_{\text{stat}} \pm 0.0^b_{\text{sys}}$	1.5
ACIS-S (Faint Mode)[a]	I	$2.1 \pm 1.9_{\text{stat}} \pm 0.0^b_{\text{sys}}$	0.56
All except ACIS-S (Graded Mode)	...	$1.4 \pm 0.6_{\text{stat}} \pm 1.0^c_{\text{sys}}$	...
All except HRC-S	...	$3.4 \pm 0.3_{\text{stat}} \pm 1.0^c_{\text{sys}}$	...
All	...	$2.9 \pm 0.5_{\text{stat}} \pm 1.0^{c,d}_{\text{sys}}$	...

Table 2.6: Temperature Decline Percentages for the NS in Cas A over 2000–201.

[a] Adopted temperature decline for comparison with other detectors.

[b] Systematic errors calculated based on interval indicated by the standard deviation between all of the Cases for this detector.

[c] Combined temperature decline percentages calculated from the weighted average using the statistical errors, after rescaling errors where $\chi^2_\nu > 1$. I set the systematic error due to region selection using the larger error indicated by the ACIS-S in Graded mode.

[d] The statistical error includes an additional multiplicative rescaling since the χ^2_ν of this weighted average was 3.0.
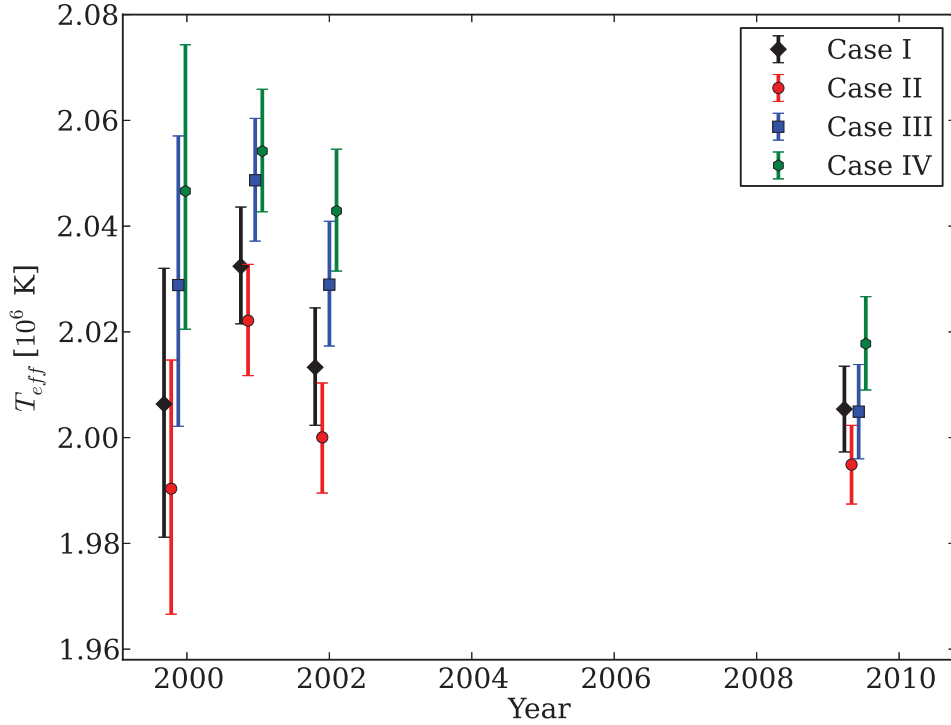
Figure 2.2: Inferred temperatures from HRC-S count rates for the NS in Cas A with different cases of source and background extraction regions (see Table 2.1 for case definitions). Cases II, III, IV have been shifted by a small offset in time (+0.1, +0.2, +0.3, respectively) to make them easier to distinguish. The temperature decline over 10 years, for different cases, ranges from $0.9 \pm 0.6\%$ ($\chi^2 = 2.7$ for 2 d.o.f) to $2 \pm 0.7\%$ ($\chi^2 = 1.3$ for 2 d.o.f). Our preferred value for comparison with other detectors, Case I, exhibits a temperature decline of $1.0 \pm 0.7\%$ ($\chi^2 = 1.8$ for 2 d.o.f).

($\chi^2 = 1.3$ for 2 d.o.f) and $1.8 \pm 0.7\%$ ($\chi^2 = 0.3$ for 2 d.o.f) for Cases III and IV, respectively (see Figure 2.2). The larger source and background extraction regions in Cases III and IV are more likely to contain variable filament emission. I summarize these results in Table 2.6 for HRC-S and all other detectors.

As a third method of estimating the temperature decline, I measured the background-subtracted energy flux for the NS (for Cases I–III) using the CIAO tool `eff2evt`, which calculates an inferred flux for each detected photon. Since the HRC energy resolution is poor, I select an energy of 1.5 keV to calculate the QE and effective area, which corresponds to the peak of the NS spectrum.

The results are consistent with the other two methods of calculating the flux and/or temperature decline, for the corresponding cases. Case I shows a $5.2^{+3.1}_{-3.3}\%$ decline in the measured flux over 10 years, while in Case II the decline is $4.0^{+3.4}_{-3.5}\%$. Case III shows a higher measured flux decline over 10 years of $9.5 \pm 2.3\%$; all of these linear fits show $\chi^2_\nu < 1$. These fits correspond to temperature declines that are consistent with the other two methods.

Since the larger extraction regions (Cases III and IV) are more likely to suffer from additional systematic errors produced by variable filament emission, I prefer Case I as our default source extraction region. Moreover, using Case I provides for consistent comparison with past work. Although I expect that Cases III and IV would be more likely to be affected by a filament, a priori I could not predict the direction of this effect on the temperature decline. However, there is still a chance that Cases I and II could be more strongly affected by a filament (e.g., if a variable filament was in their background extraction region). Therefore I adopt the standard deviation of the temperature decline of Cases I–IV as a quantitative measure of the confidence interval for the systematic error due to region selection in this complex source. Choosing Case I as our default extraction region for comparison with previous work and across other detectors, our best-fit temperature decline for HRC-S is $1.0 \pm 0.7_{\mathrm{stat}} \pm 0.6_{\mathrm{sys}}\%$ over 10 years.

2.4.2 ACIS-S, Graded

I first determine how the temperature decline was affected by the recent calibration upgrades (CALDB 4.5.5.1) through direct comparison with Shternin et al. (2011, which used CALDB 4.2.1). For consistency with the previous results, I only consider Case I. The best-fit line for the Shternin et al. (2011) results shows a decline of $4.1 \pm 0.4\%$ in temperature over 10 years, with $\chi^2 = 3.3$ for 4 d.o.f., while our re-analysis using the upgraded CALDB shows an 0.8% slower decline for the same data, with a best-fit decline of $3.3 \pm 0.4\%$ with $\chi^2 = 1.0$ for 4 d.o.f.

Including ObsID 14299 from 2012 May increases our baseline to 12 years. Under CALDB 4.5.5.1, this increases the cooling rate to $3.5 \pm 0.4\%$ over the 10 years between 2000 and 2010 (see Figure 2.3). As with the HRC-S analysis, I consider the average temperature decline of Cases
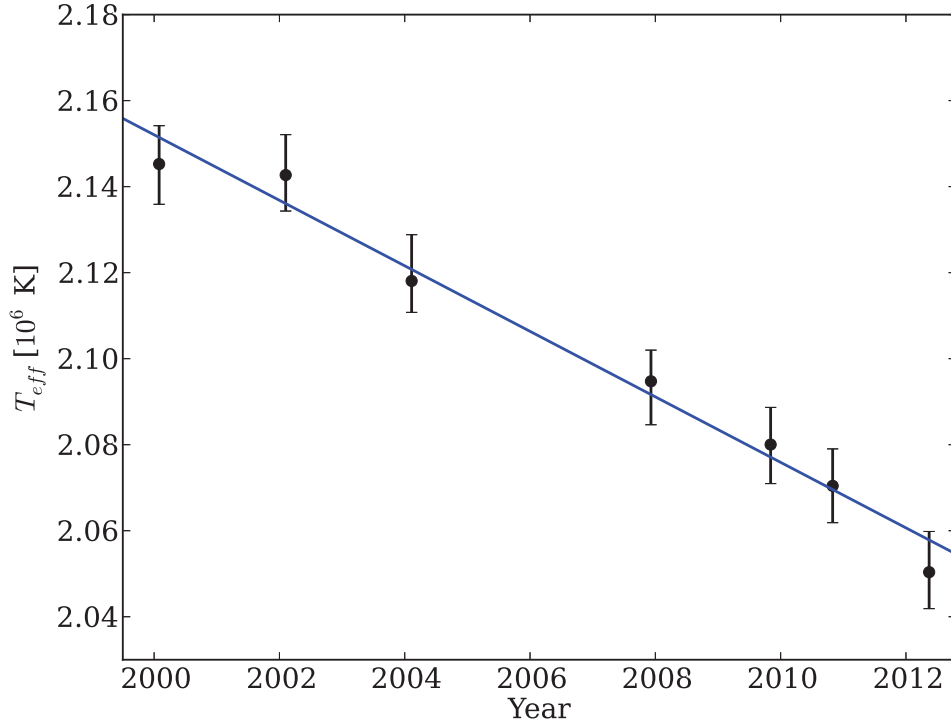
Figure 2.3: The measured temperatures from ACIS-S Graded data (Case I) for the NS in Cas A. Linear fitting (blue line) indicates a decline of $3.5 \pm 0.4\%$ ($\chi^2 = 2.0$ for 5 d.o.f.).

I–IV with the standard deviation of these cases to determine the confidence interval due to region selection. Adopting Case I as our best fit, I find the ACIS-S Graded data support a temperature decline over 10 years of $3.5 \pm 0.4_{\text{stat}} \pm 1.0_{\text{sys}}\%$.

Excluding the systematic error which will likely affect both detectors similarly, I find that the temperature decline measured by HRC-S and by ACIS-S Graded data are significantly different (at the 3.3σ level). This suggests that our measurements using one or both of these detectors still suffer from unaccounted for systematic errors. For example, the combination of moderate pileup with increasing CTI in GRADED mode data may introduce changes in ACIS-S GRADED data that are difficult to fully calibrate, but there are other possibilities for systematic effects in either detector.

Figure 2.4: The measured temperatures from ACIS-I (Case V) for the NS in Cas A. Linear fitting indicates a decline of $2.6 \pm 1.9\%$ over 10 years ($\chi^2 = 22$ for 15 d.o.f.) Temperature measurements when the NS was not on the I3 chip (crossed/cyan data points) are excluded from the fitting. ACIS-I analysis requires its unique extraction Case due to the large off-axis angles involved.

2.4.3   Other detectors

Linear fitting of the ACIS-I temperatures (using only data from the I3 CCD) gives a decline of $2.6 \pm 1.9\%$ over 10 years (see Figure 2.4) with a $\chi^2 = 22.1$ for 15 d.o.f. I also fitted the inferred temperatures after multiplying the errors by a factor of 1.47 to reduce the χ_ν^2 to 1.0. The uncertainty on the drop increases, giving a drop of $2.6 \pm 2.8\%$; this increased uncertainty was used to calculate all weighted averages.

The results from HRC-I suffer from short exposures and poor spectral resolution, which cause large errors and highly dispersed inferred temperature values. Linear fitting of the temperature decline gives a temperature drop of $2.1 \pm 1.0\%$ with a poor fit of $\chi^2 = 37.5$ for 17 d.o.f. I also

Figure 2.5: Inferred temperatures from HRC-I (Case I) count rates for the NS in Cas A. Linear fitting indicates a decline of $2.1 \pm 1.0\%$ over 10 years. The linear fit is poor with $\chi^2 = 37.5$ for 17 d.o.f.

performed the fitting after multiplying the errors by a factor of 2.2, to attain $\chi^2_\nu = 1$. This increases the uncertainty on the drop, to $2.0 \pm 2.4\%$ over 10 years, consistent with either the ACIS-S Graded result or no decline at all (see Figure 2.5).

Finally, a linear fitting of temperatures from ACIS-S Faint mode observations yields a drop of $2.1 \pm 1.9\%$ over 10 years (see Figure 2.6), consistent with the ACIS-S Graded result or with no temperature decline. The linear fit has a $\chi^2 = 9.6$ for 17 d.o.f.
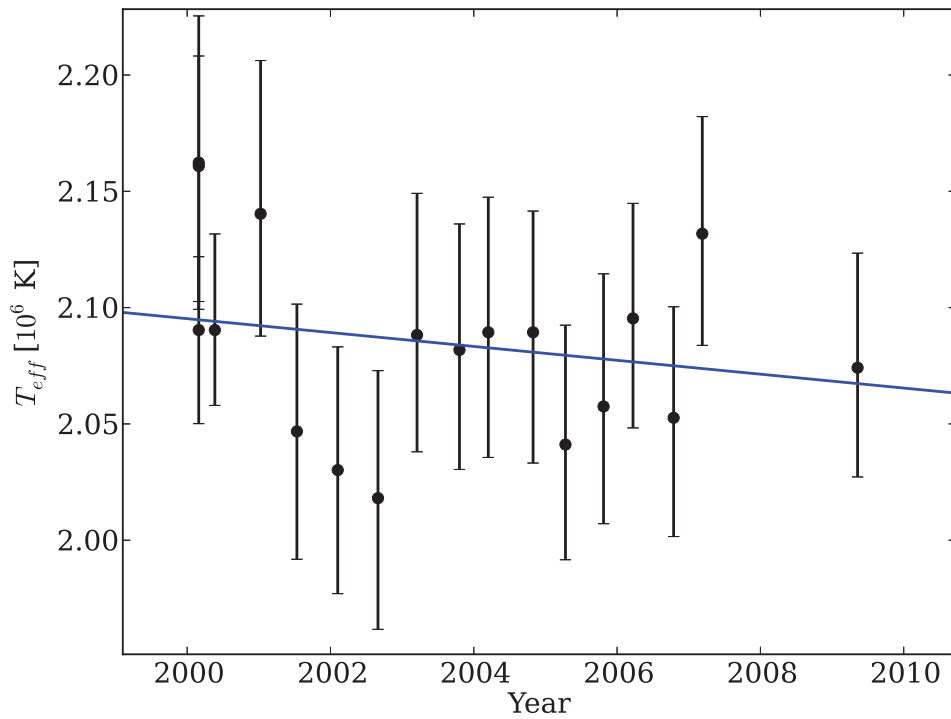
Figure 2.6: The measured temperatures from ACIS-S Faint data (Case I) for the NS in Cas A. Linear fitting indicates a decline of $2.1 \pm 1.9\%$ over 10 years ($\chi^2 = 9.6$ for 17 d.o.f.).

2.4.4 Combined Best Cooling Estimate

I synthesize a best estimate of the cooling of the Cas A NS by performing a weighted fit of the temperature declines inferred by the various detectors. For all detectors except ACIS-I, I adopt Case I to ensure a consistent comparison; ACIS-I requires its unique larger extraction regions due to the large off-axis angles of the NS in its observations. I use the statistical errors of each detector to weight the fit, and reserve the systematic error from extraction choices to include at the end (as the choices should affect all detectors similarly). I adopt the larger systematic error confidence interval from the ACIS-S Graded observations.

Our best estimate, using information from all five detector setups, is $2.9 \pm 0.3_{\text{stat}}\%$; however, the χ_ν^2 of the fit was large (3.0), mainly due to the different measurements of the HRC-S and ACIS-S Graded data. To account for this discrepancy, I multiply the statistical error by the square root of this χ_ν^2. Our final best-fit estimate is $2.9 \pm 0.5_{\text{stat}} \pm 1.0_{\text{sys}}\%$. After adding the errors in quadrature, the temperature decline is detected at the 2.6σ level. Figure 2.7 summarizes the results inferred from all detectors and the weighted fits.

Since there may be an unaccounted systematic error in either the ACIS-S Graded or HRC-S temperature decline and these detectors statistically dominate our results, I also calculated the combined estimate excluding each of these detectors separately. Our best-fit estimate excluding ACIS-S Graded data is $1.4 \pm 0.6_{\text{stat}} \pm 1.0_{\text{sys}}\%$, while our best-fit estimate excluding HRC-S data is $3.4 \pm 0.3_{\text{stat}} \pm 1.0_{\text{sys}}\%$.
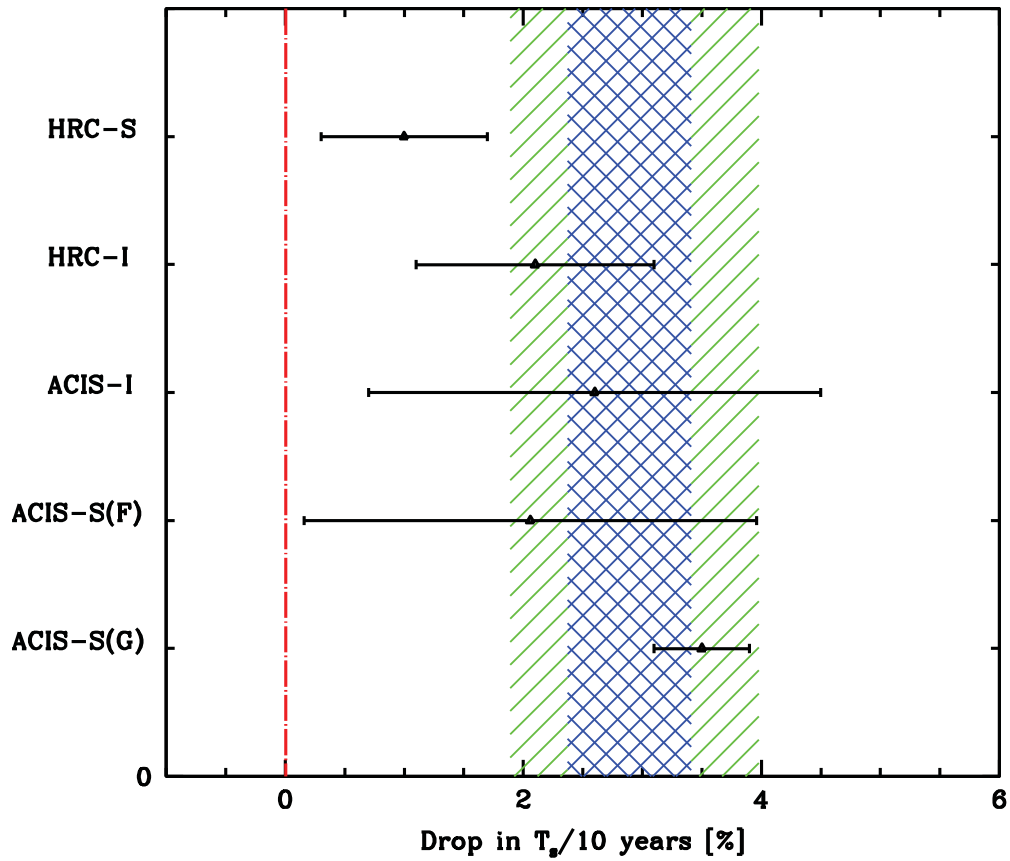
Figure 2.7: The decline in surface temperature of the NS in Cas A from all detectors on *Chandra* over 10 years (2000 to 2010). The errors on the decline inferred by each instrument are the statistical errors. The blue diagonal-hatched region indicates the best estimate from all the detectors considering only the statistical error ($2.9 \pm 0.5_{\text{stat}}\%$), while the green diagonal-hatched region includes the quadrature addition of both the statistical and the systematic error ($2.9 \pm 0.5_{\text{stat}} \pm 1.0_{\text{sys}}\%$). The best estimate is a weighted average of the individual results.

2.5 Theoretical interpretation

If the NS in Cas A underwent standard cooling (through neutrino emission from the core due to the modified Urca process) its surface temperature decline in 10 years would be $\approx 0.2\%$–0.3%. A reduction of the temperature decline of $\approx 3.6\%$, reported initially by Heinke & Ho (2010), or even as low as $\approx 1\%$, does not change the principal conclusion that the cooling is extraordinarily fast. If this rapid cooling was constant from the birth of the NS, the current temperature would have to be much smaller than is currently measured. It is reasonable to assume that the cooling was initially slow but greatly accelerated later.

The previous cooling observations were successfully explained (Page et al., 2011; Shternin et al., 2011) assuming that the NS has a superfluid nucleon core. The powerful direct Urca process of neutrino cooling from the core was supposed to be absent (either completely forbidden or strongly suppressed by superfluidity). One needed strong proton superfluidity throughout the core to appear soon after the birth of the NS to suppress the modified Urca process and make the initial cooling very slow. The corresponding critical temperature $T_{cp}(\rho)$ for proton superfluidity should be high, $T_{cp}(\rho) \gtrsim 3 \times 10^9$ K, for all densities ρ in the core. In addition, one needed moderately strong superfluidity due to triplet-state pairing of neutrons, with a wide critical temperature profile $T_{cn}(\rho)$ over the core. When the temperature T in the cooling core falls below the maximum of $T_{cn}(\rho)$, neutron superfluidity sets in. This triggers a strong neutrino outburst due to Cooper pairing of neutrons, which produces the required rapid cooling. The peak of $T_{cn}(\rho)$ was found to be $\approx (5-8) \times 10^8$ K, and neutron superfluidity should have appeared about one century ago.

I have checked that the same explanation holds for slower temperature drops of 1–2%. I have taken the same NS models as in Shternin et al. (2011) and easily obtained satisfactory agreement with slower temperature declines by slightly adjusting the parameters of superfluidity. One may need a somewhat shifted and less broad $T_{cn}(\rho)$ profile, or a smaller factor q that determines the reduction of the Cooper pairing neutrino emission by many-body effects (e.g., Leinson, 2010). Although I can also weaken proton superfluidity, the data is more readily fit if proton superfluidity

is kept strong.

These statements are illustrated in Figure 2.8, which is similar to Figure 1 of Shternin et al. (2011). Calculations are performed for the $M = 1.65\,M_\odot$ NS model with the APR (Akmal-Pahdharipande-Ravenhall) equation of state in the core. The proton superfluidity is assumed to be the same as in Shternin et al. (2011). The left panel in Figure 2.8 presents five phenomenological $T_{cn}(\rho)$ profiles over the NS core. The right panel shows corresponding cooling curves over a period of about 40 years including 10 years of observations. The ACIS-S Graded data for Case I are overlaid (with their 3.5% temperature drop). Note that I plot the effective surface temperature T_{eff}^∞ redshifted for a distant observer.

The temperature profile in the left panel of Figure 2.8 that corresponds to a 3.5% temperature decline in the right panel, profile (1a), is calculated assuming $q = 0.76$. The temperature profiles (1b) and (1c) correspond to similar $T_{cn}(\rho)$ profiles, but with higher peaks of $T_{cn}(\rho)$ and lower q (0.40 and 0.19, respectively); these models for neutron superfluidity lead to lower temperature declines of 2% and 1%, respectively. The two other profiles, (2) and (3), are calculated for $q = 0.76$; their $T_{cn}(\rho)$ profiles are shifted to higher ρ in the core and have higher peaks than (1a). They give temperature declines of 2% and 1.5% respectively. Therefore, by slightly changing $T_{cn}(\rho)$ profiles and the factor q, One can easily explain the range of temperature drops inferred from observations by different *Chandra* detectors (Table 2.6).

These proposed explanations are based on standard neutrino physics. Note that a few alternative explanations (for instance, Blaschke et al., 2012; Negreiros et al., 2012; Sedrakian, 2013) employ less standard assumptions on NS physics and evolution.
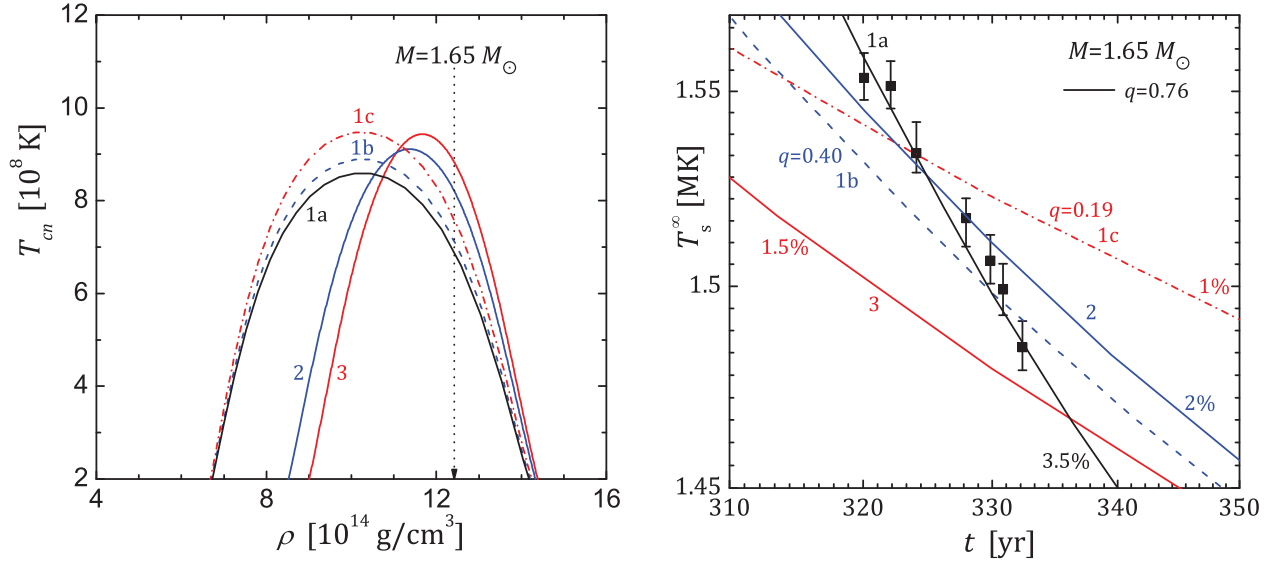
Figure 2.8: *Left:* Five models (1a), (1b), (1c), (2) and (3) for the critical temperature of triplet-state neutron pairing versus density in the NS core. The vertical dotted line shows the central density of the 1.65 $M_\odot$ NS. *Right:* Cooling curves for the 1.65 $M_\odot$ NS with the five models for neutron superfluidity and with strong proton superfluidity. For models (1a), (1b) and (1c) I adopt $q =$ 0.76, 0.40 and 0.19, respectively, while for models (2) and (3) I adopt $q = 0.76$. Calculated temperature declines over 10 years are given near the curves (in percent). The ACIS-S Graded data for Case I are overlaid.

2.6 Disagreement with ACIS-S *sub-array* results

Following work by Posselt et al. (2013) where they observed the Cas A NS with ACIS-S in Faint mode using a subarray for a second epoch (PI G. Pavlov). The importance of observation in subarray mode is avoiding pile-up of photons, where some other instruments severely suffered from as we showed in previous sections. The results compare the measurements of the surface temperature of the NS in Cas A in 2006 and 2012 and they find negligible or no temperature decrease whether assuming Hydrogen or Carbon atmosphere. They found that the drop in surface temperature varies depending on whether the value of N_H is allowed to vary or not. In case of a fixed N_H and a Carbon atmosphere, they report a 0.7% relative decline in surface temperature between he two observations, which is pushed smaller to only 0.5% relative decline in case of a varying N_H. Allowing the value of N_H to vary, and considering the $\pm 10\%$ uncertainty in the optical depth of the ACIS filter contamination, the authors report less than $1-\sigma$ significance drop in the surface temperature of the NS, and increases to $3-\sigma$ when assuming the same N_H in 2006 and 2012. This result is more likely in agreement with the HRC data we analyze in this work. This suggests that it is likely that the rapid cooling observed in this work and in Heinke et al. (2009) is a combination between instrument calibration problems specially with the the pile up and poor quality data of the ACIS-I, HRC-I and ACIS-S Faint and the possibility that significant drop we observe is due to varying N_H i.e.; foreground moving patches of the young supernova remnants.

2.7   Summary

Of all the analysed observations by *Chandra* detectors, HRC-S provides the best data to compare with the ACIS-S Graded result. However, the 1%–2% range for the temperature decline inferred from HRC-S is less than that inferred from ACIS-S Graded observations. We report a new ACIS-S Graded estimate of the actual drop in temperature of $3.5 \pm 0.4\%$ over 10 years, using a new calibration designed to deal with grade migration problems in Graded mode. Recent calibration changes have only minimally reduced the measured temperature decline.

The datasets produced by the remaining *Chandra* detectors suffer from a range of problems induced by observational circumstances. The ACIS-I observations are affected by the NS being at large off-axis angles. The statistics of the HRC-I and ACIS-S Faint data are relatively low because of their short exposure times.

Combining the available data in a consistent manner, we estimate a temperature decline of $2.9 \pm 0.5_{\mathrm{stat}} \pm 1.0_{\mathrm{sys}}\%$ over 10 years, where the systematic error is due to different source and background extraction regions. Even a temperature decline as low as 1% over 10 years would still indicate extraordinarily fast cooling of the NS in the present epoch. It can be explained by models of NSs with nucleon cores that contain strong superfluidity of protons and moderately strong superfluidity of neutrons. Successful explanations are similar to those suggested by Page et al. (2011) and Shternin et al. (2011), with slightly different parameters of nucleon superfluidity.

However, another possible explanation for the temperature decline showed by Posselt et al. (2013) using ACIS-S in subarray mode (to avoide pileup) suggest that it is due to a combination of instrument calibration issues and moving filaments in the foreground of the neutron star.

Chapter 3

Surface Temperature Inhomogeneities in Quiescent Neutron Stars

3.1 Forward

The contents of Chapters 3 and 4 constitute an accepted manuscript that will soon be published in the Astrophysical Journal (AAS00231R1). The work has been done with Heinke, C., Morsink, S., Bogdanov, S., and Stevens, A. In chapter 3, we describe the background for hot spots on neutron stars, our model of hot spot emission from a neutron star, the results on pulsed fractions, and application to searches for pulsations from specific objects. Chapter 4 gives the background for work determining the neutron star radius, describes our model for calculating the effect of hot spots on the spectrum of a neutron star, calculates the limits that can be placed on the bias created by hot spots on radius measurements via spectral fitting, and summarizes caveats to our analysis.

3.2 Introduction

Temperature inhomogeneities, typically in the form of hot spots, have long been suggested to be present on the surface of NSs. The presence of possible hot spots is a well-known concern when

modeling the emission from several varieties of NSs (e.g. Greenstein et al., 1983; Zavlin et al., 2000; Pons et al., 2002). The thermal radiation from the surface can be inhomogeneous if the polar caps of the NS are heated, either through irradiation by positrons and electrons from an active radio pulsar (Harding et al., 2002), or via accretion if the magnetic field of the NS is strong enough to channel accreting matter onto the magnetic poles (Gierliński et al., 2002), or via channeling of heat from the core to the poles if the internal magnetic field is of order 10^{12} G or higher (Greenstein et al., 1983; Potekhin & Yakovlev, 2001; Geppert et al., 2004). The result is pulsed emission from the NS surface, which can be detected if the temperature anisotropy, spot size, geometry relative to the observer, and detector sensitivity are favorable. Careful measurement of the shape of the pulse profile can constrain the ratio of mass and radius, or even both independently (e.g. Morsink et al., 2007; Bogdanov, 2013; Psaltis et al., 2014; Miller & Miller, 2015). However, in other cases (such as the blackbody method, discussed in Chapter 4), undetected temperature inhomogeneities may bias the method.

My goal in this chapter is to determine what pulsed flux fraction will be produced by hot spots of relevant ranges of size and temperature difference? Since this depends on the angle between the hot spot and NS rotational axis and between the rotational axis and the observer, the results will be probability distribution functions. Detailed calculations for this problem have been done for blackbody emission (Psaltis et al., 2000; Lamb et al., 2009), with angular beaming dependence appropriate for the accretion- and nuclear-powered pulsations observed in accreting systems in outburst. However, this calculation has not been performed specifically for hydrogen atmosphere models (which experience greater limb darkening) at temperatures relevant to quiescent NS low-mass X-ray binaries. In the next chapter, we will consider, given constraints on pulsed flux from a given quiescent NS low-mass X-ray binary, what constraints can we then impose on temperature differentials on the NS surface?

Although much of our calculations are general, we will apply them to the specific cases of the relatively bright ($L_X \sim 10^{33}$ erg/s) quiescent NS low-mass X-ray binaries X5 and X7 in the globular cluster 47 Tuc, due to their suitability for placing constraints on the NS radius. 47 Tuc is at a

distance of 4.6±0.2 kpc (Woodley et al., 2012; Hansen et al., 2013) and experiences little Galactic reddening, $E(B-V) = 0.024 \pm 0.004$ (Gratton et al., 2003). X-ray emission was discovered from 47 Tuc by *Einstein* (Hertz & Grindlay, 1983), and resolved into nine sources by *ROSAT* (Hasinger et al., 1994; Verbunt & Hasinger, 1998). Spectral analysis of the two bright X-ray sources X5 and X7 in initial *Chandra* ACIS data identified them as qLMXBs with dominantly thermal X-ray emission (Grindlay et al., 2001; Heinke et al., 2003). X5 suffers varying obscuration and eclipses as a result of its edge-on 8.7-hour orbit (Heinke et al., 2003), and has a known optical counterpart (Edmonds et al., 2002).

Extremely deep (800 kilosecond) *Chandra* observations of 47 Tuc have been performed with the HRC-S detector (Cameron et al., 2007), which retains high (microsecond) timing resolution, though it has very poor spectral resolution. This dataset enables a search for pulsations from X7 and X5, which we report in this work, utilizing acceleration searches (Ransom et al., 2001).

3.3   Theoretical Model

Our model assumes a spherical neutron star of mass M with radius R, and spin frequency f. The emission from most of the star is at one fixed temperature T_{NS}, but with one circular spot with a higher temperature T_{spot}. The spot's angular radius is ρ, and the emission angle e is the angle between the star's spin axis and the centre of the spot. The inclination angle i measures the angle between the spin axis and the direction of the observer. Figure 3.1 shows a schematic representation of the angles used in our model. The distance to the star is d and the gas column density is N_H. This leads to a total of 10 parameters to describe the flux from a star with a hot spot.

For most of our calculations, we choose the spot size to match that predicted by the polar cap model, (Lyne et al., 2006, equation 18.4):

$$\rho = (2\pi f R/c)^{1/2},\tag{3.1}$$

where c is the speed of light. This formulation reduces the number of parameters in our problem by one. This appears to be a reasonably adequate approximation for the trend of the size of X-ray
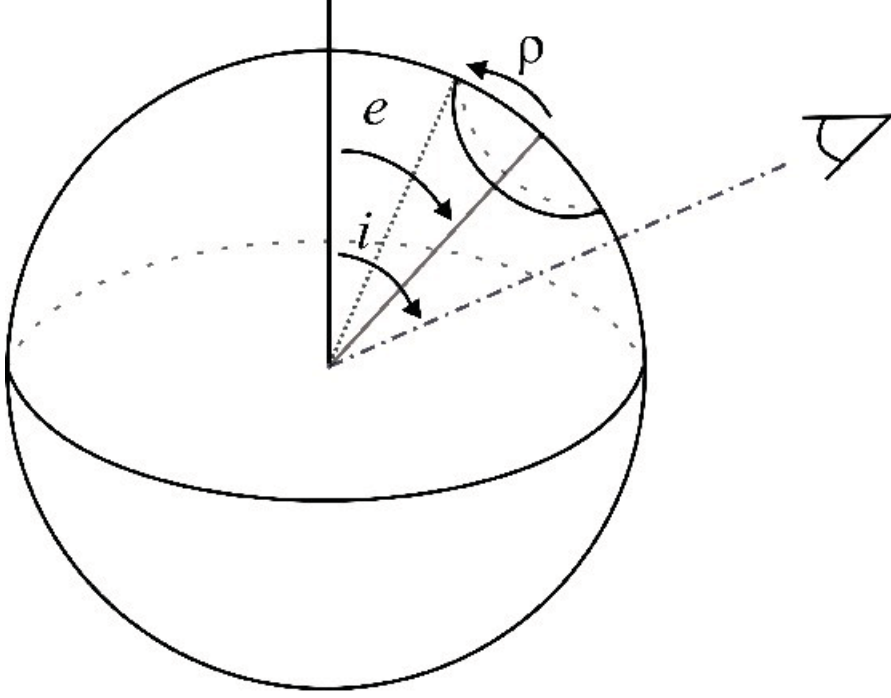
Figure 3.1: Schematic representation indicating the different angles. The spot's angular radius is ρ, and the emission angle e is the angle between the star's spin axis and the centre of the spot. The inclination angle i measures the angle between the spin axis and the direction of the observer.

emitting hot spots on radio pulsars, as suggested by phase-resolved X-ray spectral fitting of PSR J0437-4715 (Bogdanov, 2013), the Vela pulsar (Manzali et al., 2007), PSR B1055-52, and PSR B0656+14 (De Luca et al., 2005). It is not known if this is a good approximation for the spot size for qLMXBs. We will show that the dependence of pulsed fraction on spin frequency (for fixed spot size) is small.

The hydrogen atmosphere model (McClintock et al. 2004; Heinke et al. 2006; similar to that of Zavlin et al. 1996 and Lloyd 2003) assumes a thin static layer of pure hydrogen ($R_{\text{H-atm}} \ll R_{\text{NS}}$), which allows the use of a plane-parallel approximation. We assume (following e.g. Bhattacharya & van den Heuvel 1991) that the NS is weakly magnetized ($B \ll 10^9$ G), therefore the effects of the magnetic field on the opacity and equation of state of the atmosphere can be neglected. The opacity within the atmosphere is due to a combination of thermal free-free absorption and Thomson scattering. Light-element neutron star atmosphere models shift the peak of the emission to higher

energies, relative to a blackbody model at the same effective surface temperature, due to the strong frequency dependence of free-free absorption (Romani, 1987; Zavlin et al., 1996; Rajagopal & Romani, 1996). The opacity of the atmosphere introduces an angular dependence to the radiation which is beamed towards the normal to the surface, leading to a limb-darkening effect (Zavlin et al., 1996; Bogdanov et al., 2007). Limb-darkening leads to a higher pulsed fraction compared to isotropic surface emission, since the effects of light-bending and Doppler boosting are reduced (Pavlov et al., 1994; Bogdanov et al., 2007). The flux from the hydrogen atmosphere decreases slightly as the acceleration due to gravity increases, while it increases as the effective temperature increases.

The flux from the star is computed using the Schwarzschild plus Doppler approximation (Miller & Lamb, 1998; Poutanen & Gierliński, 2003) where the gravitational light-bending is computed using the Schwarzschild metric (Pechenick et al., 1983) and then Doppler effects are added as though the star were a rotating object with no gravitational field. This approximation captures the most important features of the pulsed emission for rapid rotation (Cadeau et al., 2007), except for effects due to the oblateness of the star (Morsink et al., 2007). The oblate shape of the star is not included in the computations done in this paper, since the oblate shape only adds small corrections to the pulsed fraction compared to factors such as the temperature differential and spot size. In addition, it has been shown (Bauböck et al., 2015a) that the oblate shape affects the inferred radius (at the level of a few percent) for uniformly emitting blackbody stars. We note that these effects should be even less in hydrogen atmosphere models than in blackbody models, since the limb darkening in the hydrogen atmosphere case reduces the importance of emission from the edges of the star, and thus of the exact shape.

In order to speed up the computations, we divide the flux calculation into three sections: F_{spot}, the flux from only the spot with effective temperature T_{spot} (the rest of the star does not emit); F_{NS}, the flux from the entire star with uniform temperature T_{NS}; and F_{backspot}, which only includes flux from the spot with effective temperature T_{NS}. The total observed flux is then

$$F_{\text{obs}} = F_{\text{NS}} + F_{\text{spot}} - F_{\text{backspot}}, \tag{3.2}$$

which depends on photon energy and rotational phase.

The computation of F_{spot} is done by first choosing values for M, R, f, ρ, i, e, T_{spot}, d, and N_H. The Schwarzschild plus Doppler approximation is used to compute the flux at a distance d from the star assuming that the parts of star outside of the spot do not emit any light.

For the lightcurve calculation, we first calculate the X-ray absorption by the interstellar medium (using the `tbabs` model with `wilm` abundances, Wilms et al. 2000) on the model array, assuming $N_H = 1.3 \times 10^{20}$ cm^{-2}. The N_H is inferred from the measured $E(B-V)$ using the Predehl et al. (1991) relation. We then fold the flux model array over the *Chandra* HRC effective area and a diagonal response matrix. Finally, the flux is summed over the energy range of the detector (0 - 10 keV) for each value of rotational phase. The result is the light curve emergent from a hot spot with temperature T_{spot} on the surface of a rotating neutron star, as detected by *Chandra* HRC. Similarly, F_{backspot} is computed in the same way, except that the effective temperature of the spot is T_{NS} instead of T_{spot}. To calculate the emission F_{NS} from the entire uniformly emitting surface, we calculate the predicted flux from the `NSATMOS` model at T_{NS}, folded through the `tbabs` model, using the same choices of N_H, M/R and d. The pulse fraction PF for the *Chandra* HRC is calculated by finding the maximum and minimum values for the observed flux, and computing

$$PF = (F_{\text{obs,max}} - F_{\text{obs,min}})/(F_{\text{obs,max}} + F_{\text{obs,min}}). \tag{3.3}$$

To compute the expected spectrum, we follow the same procedure for calculating the observed flux (F_{obs}), and then integrate the flux over all phase bins at each observed energy. We then incorporate X-ray absorption by the interstellar medium, and fold the flux through the relevant *Chandra* ACIS-S effective area and Response Matrix File (CALDB 4.6.3, appropriate for observations taken in 2010), ending with the phase-averaged absorbed spectrum.

In this paper, we make reference to a fiducial star with the values of $M = 1.4\ M_\odot$, $R = 11.5$ km, and $d = 4.6$ kpc. We use a value for the NS effective surface temperature $T_{\text{NS}} = 0.100$ keV (or
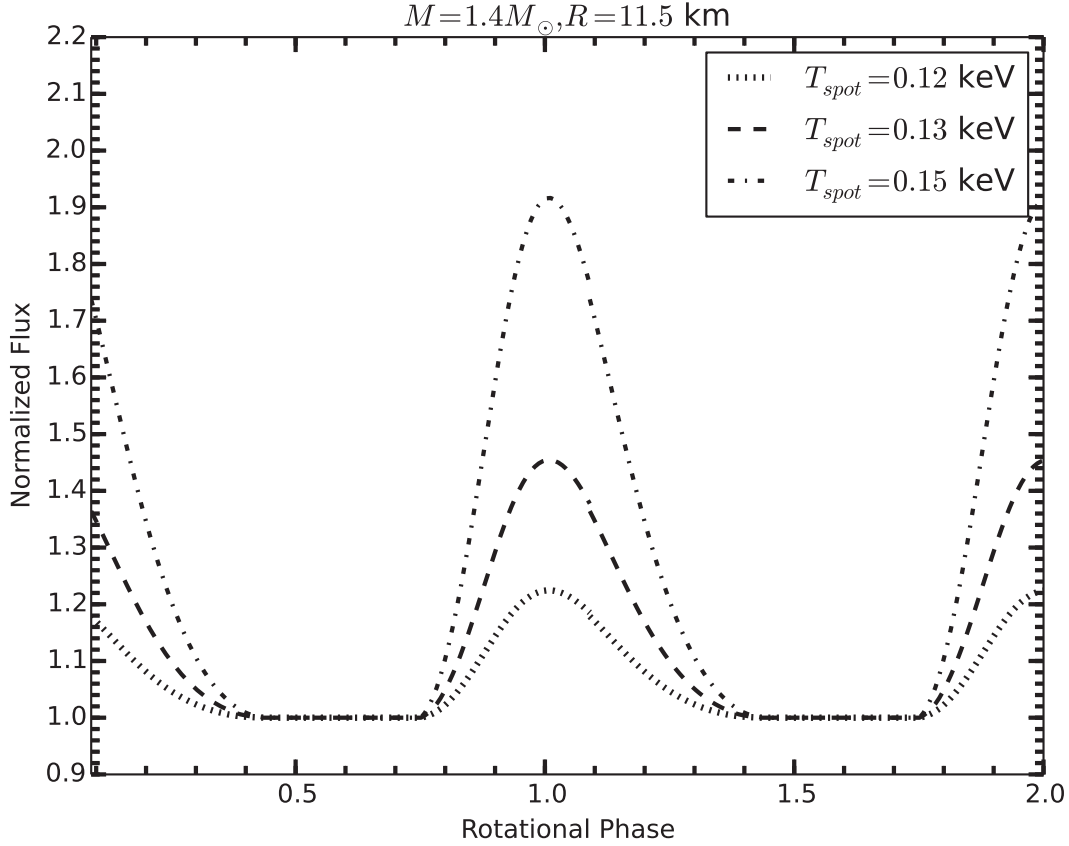
Figure 3.2: Pulse profiles for a 1.4 $M_\odot$, 11.5 km neutron star with a hot spot at $i = 86°$ and $e = 85°$ at different temperature differentials. The spin frequency is 500 Hz and $\rho = 20°$.

equivalently log T_{NS} = 6.06), which is appropriate for the qLMXBs X5 and X7 in 47 Tuc (Heinke et al., 2003, 2006; Bogdanov et al., 2016).

In Fig. 3.2, we show the normalised pulse profiles for the fiducial star with different surface temperature differentials. The star spins with frequency 500 Hz, which corresponds to a spot angular radius of 20° in Equation 3.1. The spot's centre is at colatitude 85° and the observer's inclination angle is 86°. Naturally, there is a strong dependence of the pulse fraction on the temperature of the spot. The pulse fraction increases from 16% to 27% when the temperature differential increases by 0.02 keV, from T_{spot} = 0.13 keV to T_{spot} = 0.15 keV.

49

3.4   Limits on Pulse Fraction

We now address the limits on the surface temperature differentials that can be made from obser-vational upper limits on a neutron star's pulse fraction. To investigate this, we choose different parameters M, R, f, ρ and T_{spot} describing the neutron star and its spot (with $T_{NS} = 0.1$ keV, $N_H = 1.3 \times 10^{20}$ cm^{-2} fixed for all models). For each choice of these parameters we then simu-late the pulse profiles using the methods described in Section 3.3 for 300 choices of inclination, i, and emission, e, angles. We select i and e from distributions uniform in $\cos i$, appropriate for random orientations on the sky, and for most of our analyses, uniform in $\cos e$, random positions of the magnetic axis on the neutron star. Distributions of an angle that are uniform in the cosine of the angle tend to favour inclinations close to 90°, which produce relatively large pulse fractions. We note that our assumption of a distribution of e, uniform in $\cos e$, may not be correct, if accreting NSs tend to shift their magnetic poles close to their rotational poles, as suggested in some theories (Chen & Ruderman, 1993; Chen et al., 1998; Lamb et al., 2009). Radio polarization studies do not find clear results for millisecond pulsars (Manchester & Han, 2004), but there is evidence from gamma-ray lightcurve fitting (e.g. Johnson et al., 2014) and phase-resolved X-ray spectroscopy (e.g. Bogdanov, 2013) that radio millisecond pulsars (descendants of LMXBs) generally have rel-atively large angles between their magnetic and rotational poles. To explore the effects of differing assumptions about the distribution of e, in our last analysis (on effects of spots on the inferred neutron star radius) we consider both a distribution uniform in $\cos e$, and one that is uniform in e.

We computed pulse fractions, using the same model used to generate Figure 3.2, with values of T_{spot} ranging from 0.105 keV to 0.160 keV, and a distribution of 300 choices of i and e for each spot temperature. In Fig. 3.3 we plot histograms of the pulse fractions for each value of the spot temperature.

The peak for each distribution corresponds to choices of i and e being close to 90°, which give the highest pulse fraction, while the tail of the i and e distributions extend to 3° with very small probability. As expected, as the temperature differential between the spot and the rest of the star
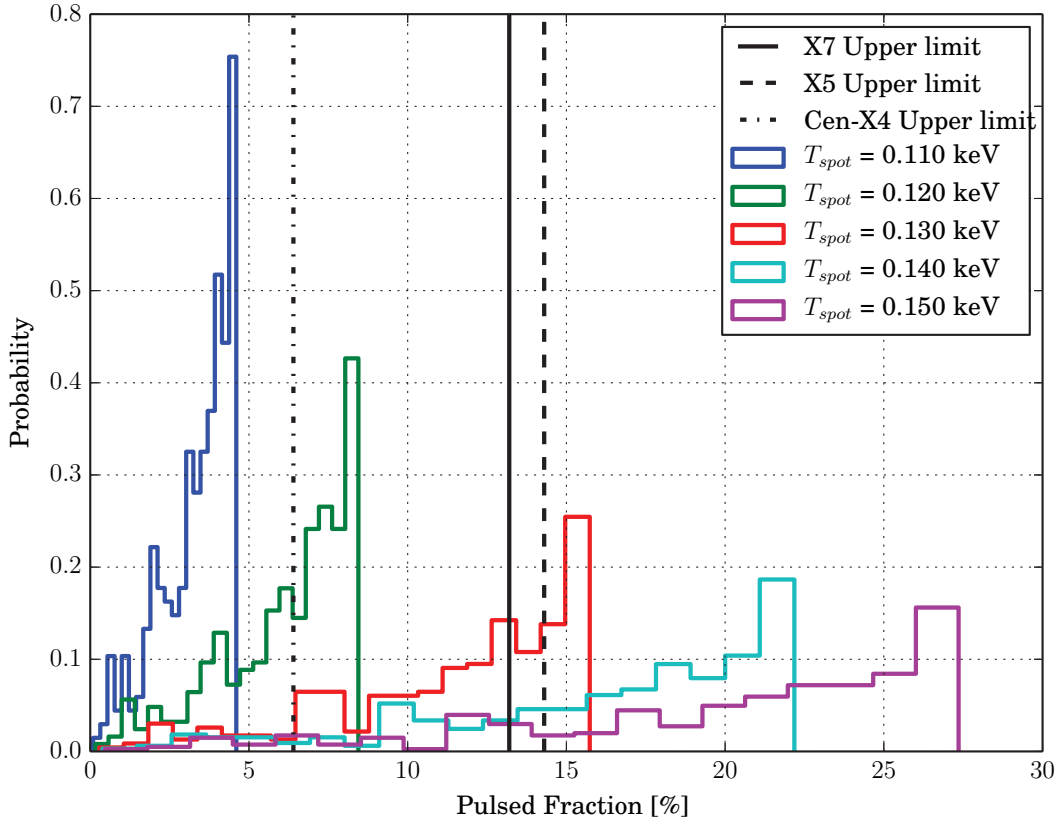
Figure 3.3: Histograms of simulated pulsed fractions for the fiducial NS with 300 different combinations of *i* and *e* for 5 different temperature differentials. The spin frequency is fixed at 500 Hz and the spot angular radius is $\rho = 20°$. The neutron star surface's effective temperature is fixed at 0.10 keV with $M = 1.4\,M_\odot$ and $R = 11.5$ km.

increases, the typical pulse fraction increases, while a tail of low pulsed fraction simulations is always present. Similarly, the spot size correlates strongly with pulse fraction. In Fig. 3.4 we vary spot size, while keeping all other parameters constant. Here, Equation (3.1) was not used to relate spin frequency and polar cap size, instead keeping the frequency fixed. In Table 3.1 we show the 90th percentile upper & lower limits on pulse fraction for a wide range of angular spot sizes ρ and spot temperatures.

We now explore the importance of the polar cap model, Equation (3.1), linking the angular spot size to the spin frequency. First, consider the effect of choosing the spin frequency independent

51

T_{spot}	ρ	f	PF	
[keV]	[°]	[Hz]	90% <	90% >
0.105	20 (24)	500 (716)	2.3 (3.7)	0.9 (1.4)
0.110	20 (24)	500 (716)	4.4 (7.0)	1.8 (2.6)
0.115	20 (24)	500 (716)	6.4 (9.9)	2.5 (3.8)
0.120	20 (24)	500 (716)	8.2 (12.6)	3.3 (4.9)
0.125	20 (24)	500 (716)	11.6 (17.3)	4.8 (6.8)
0.130	20 (24)	500 (716)	15.4 (22.5)	6.6 (9.0)
0.135	20 (24)	500 (716)	18.7 (26.9)	7.9 (11.0)
0.140	20 (24)	500 (716)	21.7 (30.7)	9.2 (12.7)
0.145	20 (24)	500 (716)	24.4 (33.9)	10.3 (14.1)
0.150	20 (24)	500 (716)	26.8 (37.3)	11.3 (15.5)
0.155	20 (24)	500 (716)	30.1 (41.1)	12.6 (17.1)
0.160	20 (24)	500 (716)	34.8 (46.3)	14.5 (19.3)

Table 3.1: Results for Monte Carlo simulations of 300 choices of i and e (drawn from distributions uniform in $\cos i$ and $\cos e$), for each choice of spot temperature and rotation rate (500 Hz and 716 Hz). The spot size is determined by the polar cap model. The values in parentheses are for the case of spin frequency 716 Hz and spot size of 24°. The last two right columns represents the upper and lower 90% bounds on the pulsed fraction.
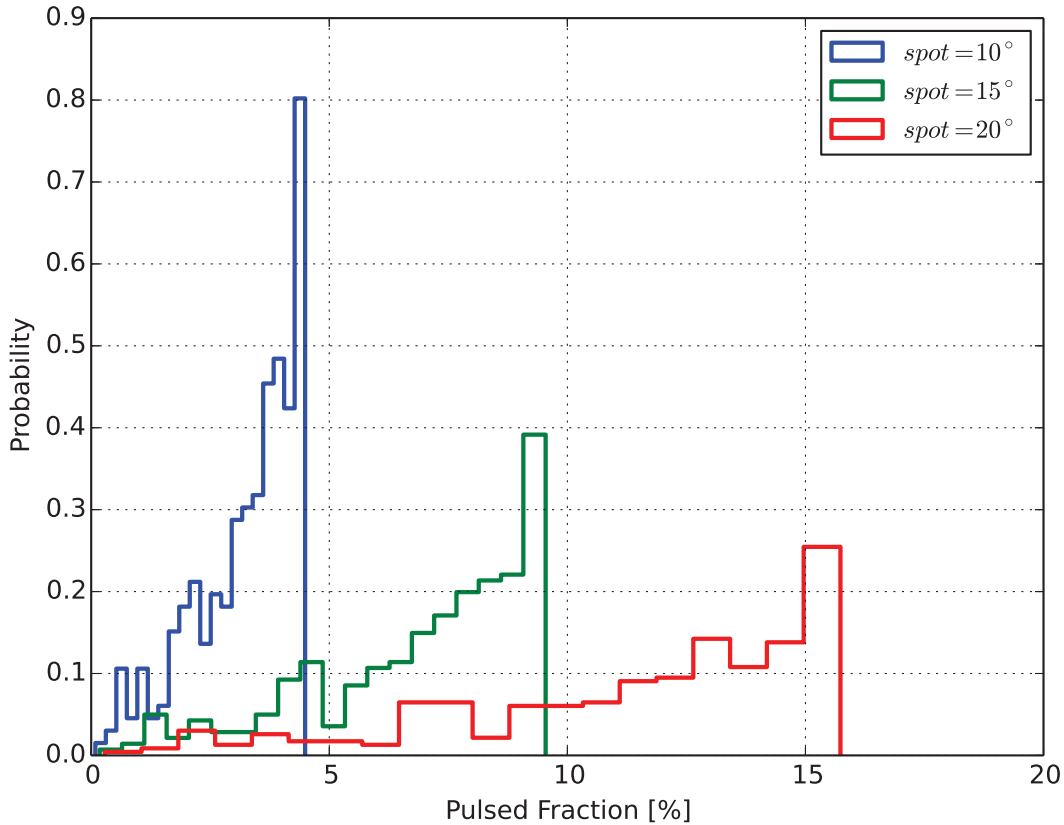
Figure 3.4: Effect of angular spot radius on the histogram of pulse fractions for 300 values of i and e. For each histogram the neutron star parameters were fixed at $M = 1.4\,M_\odot$, $R = 11.5$ km, $T_{\mathrm{NS}} = 0.10$ keV, $T_{spot} = 0.13$ keV, $f = 500$ Hz.

of the spot size. As the star's spin increases, the Doppler boosting increases, which increases the intensity of the blueshifted side of the star, which will increase the pulse fraction. This effect is shown in Figure 3.5, where it can be seen that increasing the star's spin frequency does increase the pulse fraction. However, the effect is quite small, since the pulse fraction increases only by 2% when the frequency increases from 100 to 500 Hz. This should be contrasted with Figure 3.4 where the effect of changing the spot size but keeping the spin frequency fixed is shown. Increasing the angular spot radius by a factor of two increases the maximum pulse fraction by a factor of three.

The choice of mass and radius affects the pulse profile through two physical effects. First, the ratio of M/R controls the angles through which the light rays are bent. Larger M/R gives a more
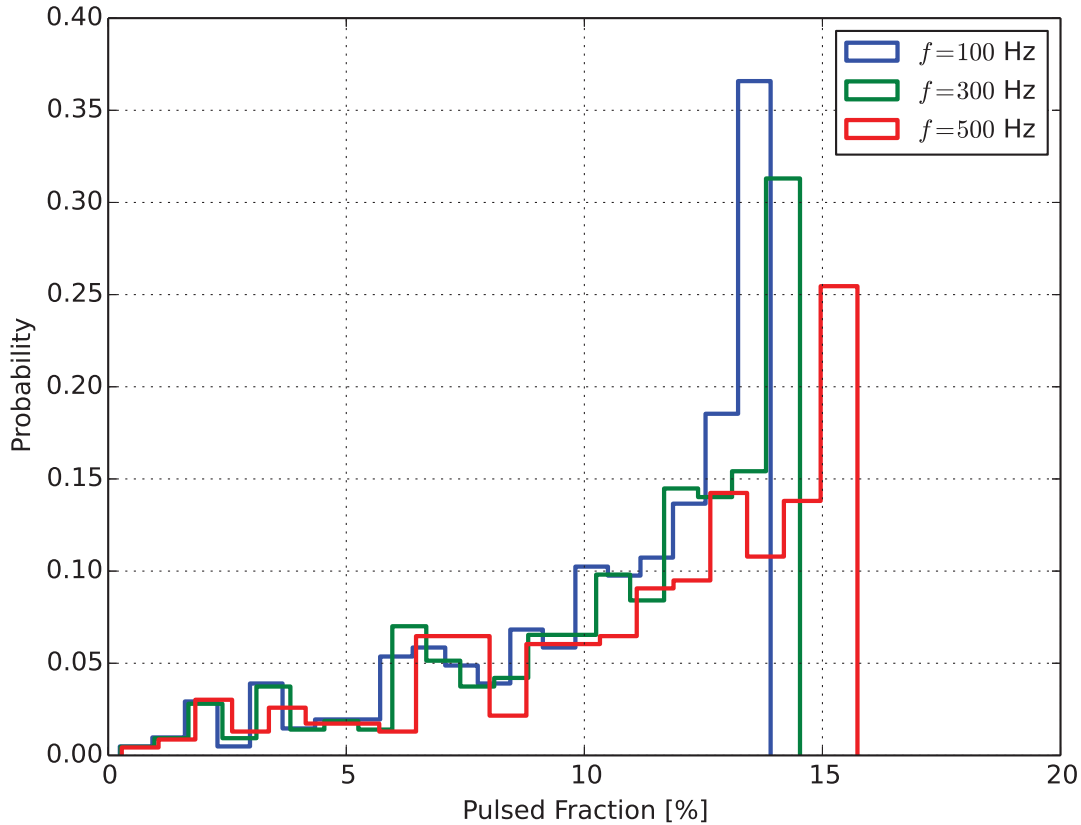
Figure 3.5: Effect of spin frequency on the histogram of pulse fractions for 300 values of i and e. For each histogram the neutron star parameters were fixed at $M = 1.4\,M_\odot$, $R = 11.5$ km, $T_{NS} = 0.10$ keV, $T_{spot} = 0.13$ keV, $\rho = 20°$.

compact star, which produces more gravitational bending. This leads to more of the star being visible at any time, which produces a lower pulse fraction (Pechenick et al., 1983), as can be seen in Figure 3.6. Secondly, increasing the surface gravity (where $g = GMR^{-2}/\sqrt{1-2GM/Rc^2}$) alters the emission pattern, decreasing the limb darkening, which decreases the pulse fraction. The effect of the surface gravity is shown in Figure 3.7 where different values of M and R are chosen so that the ratio M/R is kept constant. The largest star has the lowest surface gravity and the largest pulse fraction. Both effects are small, with changes in M/R causing changes in the pulse fraction of a similar order as the changes due to spin frequency. The effects due to surface gravity changes are even smaller. All of these effects act to increase the pulse fraction if the radius of the star is

increased while keeping the mass constant, as shown by Bogdanov et al. (2007).

In this work, we simulate the effects of one spot. Adding a second spot would typically reduce the measured pulse fraction. This depends on the compactness of the star, on the angles e and i, and on whether the spots are antipodal. For angles e and i near 90 degrees, one spot will always be visible (for typical neutron star compactness values, such as our 11.5 km, 1.4 $M_\odot$ standard star), which will reduce the pulsed fraction. However, if the angles e and i are both far from 90 degrees, then the far spot will not be strongly visible and the pulsed fraction will not change dramatically. Thus, the effect on the histograms of pulsed fractions will be to shift the peak to smaller values, but the tail at low values (which is made up of realizations with small values of e and/or i) will be much less affected. The 90th percentile lower limits on the pulse fraction are set by the tail at low values, so the pulsed fraction lower limits will generally not be strongly affected by adding a second spot (assuming it is antipodal to the first spot).

3.4.1   Application to qLMXBs in 47 Tuc, M28 and Cen X-4

Among globular cluster qLMXBs with thermal spectra, only three (X5 and X7 in 47 Tuc, and source 26 in M28) have substantial observations with a telescope and instrument with the timing and spatial resolution (Chandra's HRC-S camera in timing mode) to conduct significant searches for pulsations at spin periods of milliseconds.[1] These targets have not previously been searched for pulsations.

To search for pulsations from qLXMBs we make use of *Chandra* HRC-S observations, which offer a time resolution of ∼16 μs in the special SI mode. We extracted lightcurves from X7 and X5 from 800 ksec of *Chandra* HRC-S data, obtained during December 2005 to January 2006, described in Cameron et al. (2007). We also extracted source events from the M28 qLMXB (named Source 26 by Becker et al. 2003) from two exposures obtained in 2002 and 2006 (Rutledge et al., 2004;

---

[1]Note that Papitto et al. (2013) searched for pulsations from the accreting millisecond X-ray pulsar IGR J18245-2452 during an intermediate-luminosity (1.4×10^{33} erg/s) outburst, using a 53-ks HRC-S observation of M28 and a known ephemeris for the pulsar, and placed an upper limit of 17% on the pulse amplitude.

Cluster/source	ObsID	Date	Exposure (ks)
47 Tucanae	5542	2005 Dec 19	50.16
X5 & X7	5543	2005 Dec 20	51.39
	5544	2005 Dec 21	50.14
	5545	2005 Dec 23	51.87
	5546	2005 Dec 27	50.15
	6230	2005 Dec 28	49.40
	6231	2005 Dec 29	47.15
	6232	2005 Dec 31	44.36
	6233	2006 Jan 2	97.93
	6235	2006 Jan 4	50.13
	6236	2006 Jan 5	51.92
	6237	2005 Dec 24	50.17
	6238	2005 Dec 25	48.40
	6239	2006 Jan 6	50.16
	6240	2006 Jan 8	49.29
M28	2797	2002 Nov 8	49.37
Source 26	6769	2006 May 27	41.07

Table 3.2: Archival *Chandra* HRC observations of 47 Tucanae and M28.
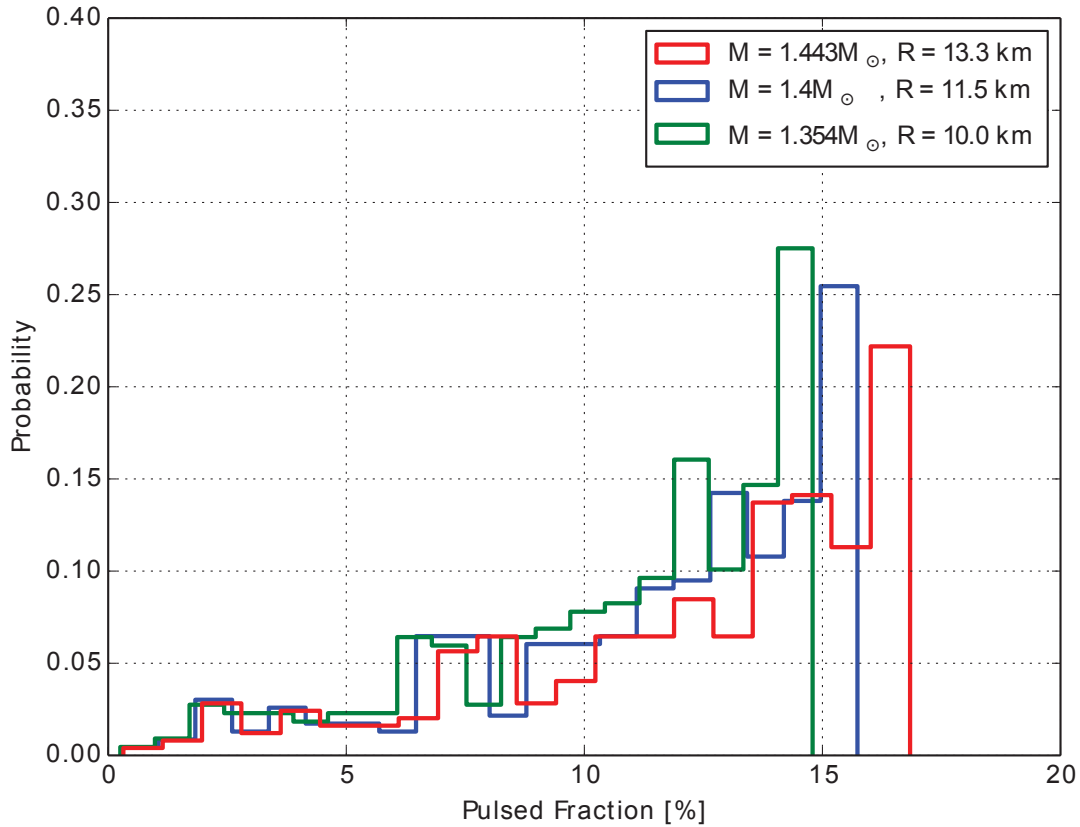
Figure 3.6: Effect of M/R on the histogram of pulse fractions for 300 values of i and e. The choices of M/R values are 0.16, 0.18, and 0.2 for the red, blue and green histograms respectively. For each histogram the neutron star parameters were fixed at $T_{NS} = 0.10$ keV, $T_{spot} = 0.13$ keV, $f = 500$ Hz, and $\rho = 20°$. Values of mass and radius are chosen so that $\log g = 14.244$.

Bogdanov et al., 2011). Table 3.2 summarizes the archival observations that were used in this analysis. For each source the events were extracted from circular regions of radius 2.5″ centered on the positions obtained from `wavdetect`. The recorded arrival times were then translated to the solar system barycenter using the `axbary` tool in CIAO assuming the DE405 solar system ephemeris. The HRC provides no reliable spectral information so all collected events were used for the analysis below.

The pulsation searches were conducted using the PRESTO pulsar search software package. Given that NS qLMXBs are by definition in compact binaries, the detection of X-ray pulsations
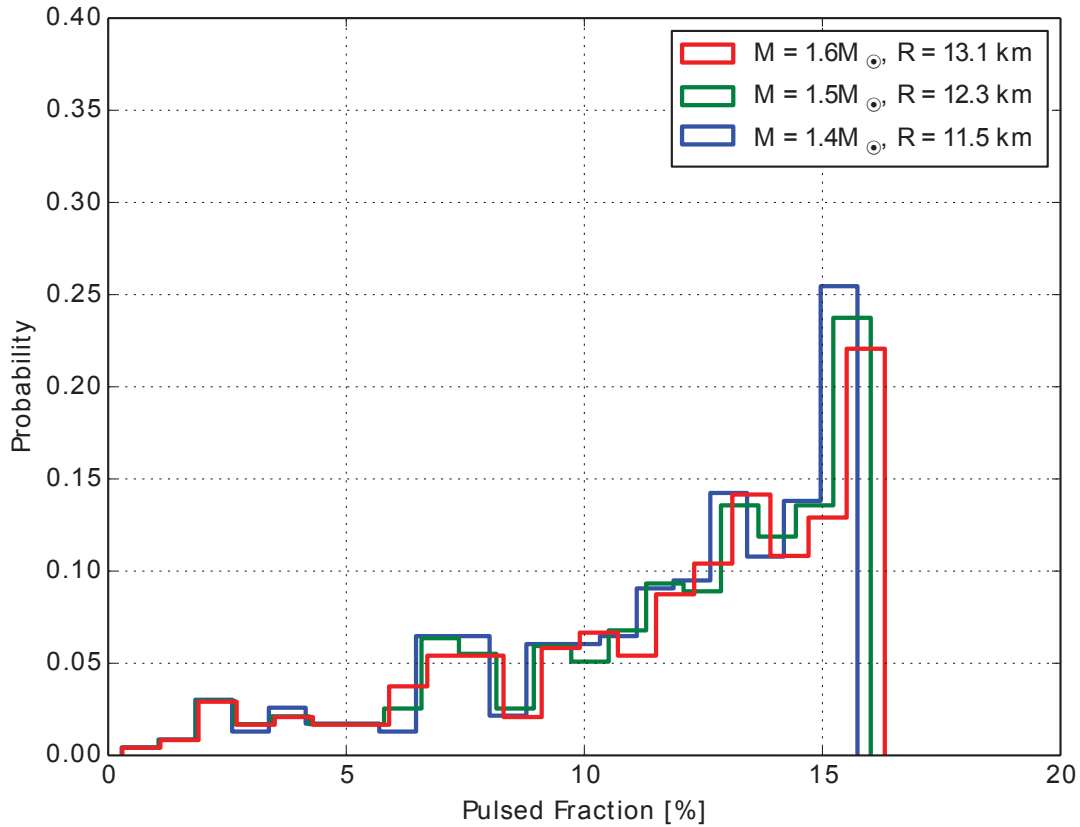
Figure 3.7: Effect of surface gravity on the histogram of pulse fractions for 300 values of *i* and *e*. The choices of $\log g$ are 14.186, 14.214 and 14.244 for the red, blue and green histograms. For each histogram the neutron star parameters were fixed at $M/R = 0.18$, $T_{\rm NS} = 0.10$ keV, $T_{spot} = 0.13$ keV, $f = 500$ Hz, and $\rho = 20°$.

from these objects in blind periodicity searches is complicated by the binary motion of the NS, which smears out the pulsed signal over numerous Fourier bins and thus diminishes its detectability. Therefore, it is necessary to employ Fourier-domain periodicity search techniques that compensate for the binary motion when searching for spin-induced flux variations. For this analysis, we use two complementary methods: acceleration searches and "sideband" (or phase-modulation) modulation searches. For the acceleration search technique, the algorithm attempts to recover the loss of power caused by the large period derivative induced by the rapid orbital motion (Ransom, 2002). This method is most effective when the exposure time of the observation is a small fraction of the orbital

period. In contrast, the sideband technique is most effective when the observation is much longer than the orbital period, provided that the observation is contiguous (Ransom et al., 2003). This approach identifies sidebands produced in the power spectrum centered around the intrinsic spin period and stacks them in order to recover some sensitivity to the pulsed signal.

The orbital periods of LMXBs are typically of order hours, or for the case of ultracompact systems, $\lesssim$1 hour. Due to the relatively low count rates of the three qLMXB sources, searching for pulsations over short segments of the binary orbit ($\lesssim$30 minutes) is not feasible so acceleration searches are insensitive to pulsations from these targets. As the *Chandra* exposures are longer than the orbital cycle of X5 and likely for X7 and M28 source 26 as well, the phase-modulation method is the most effective for this purpose.

The maximum frequency that we search up to sets our number of trials, and thus sets how strong an upper limit we can set. The pulse fraction limit increases as we go to higher frequencies because it is necessary to bin the event data for the acceleration and sideband searches. This causes frequency dependent attenuation of the signal - resulting in decreased sensitivity at high frequencies (e.g. Middleditch, 1976; Leahy et al., 1983). The pulse fraction upper limits were obtained in PRESTO, which considers the maximum power found in the power spectrum as described in Vaughan et al. (1994).

We find no evidence for coherent X-ray pulsations in any of the individual observations of the three qLMXBs. The most restrictive upper limits on the X-ray pulsed fraction were obtained from the longest exposures. We find that for spin periods as low as 2 ms (500 Hz), the 90% upper limit on any pulsed signal is 14%, 13%, and 37%, for X5, X7 and M28 source 26, respectively. Performing searches up to the fastest known neutron star spin period (Hessels et al., 2006), 1.4 ms (716 Hz), the limits are 16%, 15%, and 37%. Since the pulsed fraction upper limit for Source 26 in M28 is so high, it does not lead to useful constraints, so we do not consider it further in our analysis.

Our pulsed fraction upper limit on X7 (as an example) places limits on the temperature differentials that the NS may have. For a spin frequency of 500 Hz, the 90% upper limit of 13% can be compared with the pulse fraction probabilities for different spot temperatures shown in Table

3.1. For example, for a spot temperature of 0.125 keV, 90% of computed models have a pulse fraction smaller than 11.6%. In fact, all computed models at this spot temperature (0.125 keV) have pulse fractions below the 13% upper limit for X7, so this temperature differential is consistent with the observations. This means that X7 could have an undetected hot spot. However, increasing the spot temperature to 0.130 keV, the histogram plotted in Figure 3.3 shows that only 58% of our simulations give a pulsed fraction below the 90% upper limit on X7's pulsed fraction.

For higher spot temperatures, it becomes more improbable to have an undetected hot spot; that is, a pulse fraction below the 90% upper limit on the pulse fraction for X7. We find that a spot temperature of 0.155 keV, or a temperature differential of 0.055 keV, gives the maximum temperature differential allowable for X7. This calculation assumes that X7 is spinning at 500 Hz. For higher spin frequencies, which give a larger spot radius (as we linked frequency to spot radius), we get higher pulsed fractions when other inputs are identical. Therefore, the maximum temperature differential allowable slightly decreases to 0.050 keV (spot temperature of 0.150 keV) above which, over 90% of the simulations are above the 90% pulse fraction upper limit of X7. The 90% upper limit on X5's pulsed fraction is only 1% larger than that for X7, which will increase the maximum temperature differential allowable for X5 by a few percent more than allowed for X7 ($\sim$0.005 keV larger). Our computations all assume that the neutron star has $M = 1.4\ M_\odot$ and $R = 11.5$ km, however, our results show that the dependence on mass and radius is weak.

Even more stringent constraints are possible from the accreting neutron star in Cen X-4, which was observed at a similar luminosity as X7, but at a distance of only 1.2 kpc (Chevalier & Ilovaisky, 1989), with a more sensitive X-ray telescope, *XMM-Newton*. D'Angelo et al. (2015) used a deep (80 ks) *XMM-Newton* observation (Chakrabarty et al., 2014), in which the PN camera was operated in timing mode (with 30 μs time resolution), to search for pulsations. D'Angelo et al. utilized a semicoherent search strategy, in which short segments of data are searched coherently, and then combined incoherently (Messenger, 2011). This analysis assumed a circular orbit, with orbital period and semimajor axis as measured by Chevalier & Ilovaisky (1989), but left orbital phase free.

D'Angelo et al. calculated a fractional-amplitude upper limit of 6.4% from Cen X-4 in qui-

escence. This is significantly lower than the pulsed fraction limits in X5 and X7, so it provides a tighter constraint on the temperature differential, as can be seen in Fig. 3.3. If we assume the neutron star in Cen X-4 to have the same physical properties as X7, then its maximum spot temperature must be smaller. Our simulations show that even with this small upper limit Cen X-4 can have small temperature differentials (up to 0.01 keV) with all simulations being below the pulsed fraction upper limit. The maximum spot temperature the neutron star in Cen X-4 may have is 0.130 keV, at which 90% of the simulations have pulsed fractions that are above the 90% upper limit. Similarly, for higher frequencies, at 716 Hz, the maximum allowable spot temperature decreases to only 0.125 keV. In chapter 4, we address how these possible hot spots could affect spectroscopic inferences of neutron star radii, and what limits we can place on these effects from our constraints on the pulsed fraction and temperature differential.

3.5   Summary

In this chapter, we studied the effects of hot spots on the lightcurves and pulsed fraction of quiescent neutron stars with hydrogen atmospheres. Hydrogen atmospheres, due to limb darkening, display higher pulsed fractions than blackbody emission, so a new analysis is necessary in order to constrain the systematic effects of radius measurements on quiescent neutron stars.

We first computed the 90% upper limits on the pulsed fractions from 800 ks *Chandra* HRC-S observation for the two sources X5 and X7 in the globular cluster 47-Tuc to be 14% and 13% respectively, searching spin frequencies < 500 Hz. For higher spin frequencies (up to 716 Hz) the limits are 16% and 15% respectively. We simulated pulse profiles for ranges of inclination and hot spot emission angles i and e , obtaining the central 90% range of pulse fraction obtained for different choices of temperature differentials (between the hot spot and the rest of the NS) and NS spin frequencies. This allows us to constrain the maximum temperature differential for any hot spots on X5 and X7. In the case of X7, if we assume it is a 1.4 $M_{\odot}$ neutron star spinning at 500 Hz, our results indicate that the maximum allowable temperature differential is 0.055 keV, where

> 90% of our simulations are above the 90% upper limit of pulsed fraction. The neutron star in Cen-X4 has a significantly lower upper limit on the pulse fraction of 6.4%, which puts a tighter constraint on the maximum allowable temperature differential of 0.025 keV. Since the upper limit of Source 26 in M28 is high (37%), it does not provide strong constraints.

Chapter 4

The Impact of Surface Temperature Inhomogeneities on Quiescent Neutron Star Radius Measurements

4.1   Forward

The contents of Chapters 3 and 4 constitute an accepted manuscript that will soon be published in the Astrophysical Journal (AAS00231R1). The work has been done with Heinke, C., Morsink, S., Bogdanov, S., and Stevens, A. In chapter 3, we described the background for hot spots on neutron stars, our model of hot spot emission from a neutron star, the results on pulsed fractions, and application to searches for pulsations from specific objects. Chapter 4 gives the background for work determining the neutron star radius, describes our model for calculating the effect of hot spots on the spectrum of a neutron star, calculates the limits that can be placed on the bias created by hot spots on radius measurements via spectral fitting, and summarizes caveats to our analysis.

4.2   Introduction

Measuring the neutron star's radius with good accuracy is a major challenge, which if successful, will enable constraints upon the interior physics of NSs. One method for determining the size of a NS is through a modification of the blackbody radius method (van Paradijs, 1979); if the distance, flux and temperature of a perfect blackbody sphere can be measured, then its radius is also known. Since NSs are not perfect blackbodies, this method has been modified to take into account more realistic spectra. General relativistic effects also make these radius measurements degenerate with mass, providing constraints along curved tracks close to lines of constant $R_\infty = R/\sqrt{1-2GM/(Rc^2)}$, where M and R are the NS mass and radius.

The two main types of NSs that this method has been applied to are NSs with Type I X-ray bursts, and NSs in quiescent low mass X-ray binaries (qLMXBs). Some NSs that have Type I X-ray bursts also exhibit photospheric radius expansion (PRE) bursts, and these systems have great potential (Sztajno et al., 1987; Damen et al., 1990; Lewin et al., 1993; Özel, 2006) to provide EOS constraints. Observations of PRE bursts and fitting to different spectral models have provided some estimations of the NS mass and radius (Özel et al., 2009; Güver et al., 2010b,a; Suleimanov et al., 2011; Poutanen et al., 2014; Nättilä et al., 2015). However, a variety of uncertainties in the chemical composition of the photosphere, the emission anisotropy, color correction factors, and changes in the persistent accretion flux, complicate these analyses (Bhattacharyya, 2010; Steiner et al., 2010; Galloway & Lampe, 2012; Zamfir et al., 2012; Worpel et al., 2013; Özel et al., 2016).

An alternative approach is to fit the emission from low-mass X-ray binaries during quiescence (qLMXBs). During quiescence, the X-rays are (often) dominated by thermal emission from the quiet NS surface, due to heating of the NS core and crust during accretion episodes (Brown et al., 1998). Nonthermal emission is often present, and typically fit by a power-law; this emission may be produced by accretion, synchrotron emission from an active pulsar wind, and/or a shock between this wind and inflowing matter (Campana et al., 1998b; Deufel et al., 2001; Cackett et al., 2010; Bogdanov et al., 2011; Chakrabarty et al., 2014). The thermal emission passes through a single-

component atmosphere (typically a few cm layer of H, which would have a mass of $\sim 10^{-20}$ $M_\odot$ for ~ 1 cm (Zavlin & Pavlov, 2002)) , since the elements gravitationally settle within seconds (Alcock & Illarionov, 1980; Hameury et al., 1983). Current physical models of hydrogen atmospheres in low magnetic fields (appropriate for old accreting NSs) are very consistent and reliable (Zavlin et al., 1996; Rajagopal & Romani, 1996; Heinke et al., 2006; Haakonsen et al., 2012).

Recent work has focused on qLMXBs in globular clusters, where the distance can be known as accurately as 6% (Woodley et al., 2012), thus enabling stringent constraints on the radius (Rutledge et al., 2002a). Observations with *Chandra* and its ACIS detector (high spatial and moderate spectral resolution), or *XMM-Newton* with its EPIC detector (moderate spatial resolution, higher sensitivity) have allowed the identification and spectroscopy of globular cluster qLMXBs. Several dozen qLMXBs are now known in globular clusters, but only a few provide sufficient flux, and have sufficiently little interstellar gas absorption, to provide useful constraints (e.g. Heinke et al., 2006; Webb & Barret, 2007; Guillot et al., 2011; Servillat et al., 2012). The errors on a few of these measurements are beginning to approach 1 km, or $\sim$10% (see e.g. Guillot et al. 2013), at which point they become useful for constraining nuclear physics (Lattimer & Prakash, 2001). Indeed, a new *Chandra* observation of the qLMXB X7 in 47 Tuc provides radius uncertainties at the 10% level (Bogdanov et al., 2016).

Thus, it has now become crucially important to identify and constrain systematic uncertainties in the qLMXB spectral fitting method. Previous works have checked the effects of variations between hydrogen atmosphere models (Heinke et al., 2006; Haakonsen et al., 2012), distance errors (Heinke et al., 2006; Guillot et al., 2011, 2013; Heinke et al., 2014; Bogdanov et al., 2016), detector systematics (Heinke et al., 2006; Guillot et al., 2011; Heinke et al., 2014), and modeling of the interstellar medium (Heinke et al., 2014; Bogdanov et al., 2016). The largest systematic uncertainty identified so far is the atmospheric composition. If the accreted material contains no hydrogen (as expected from white dwarfs that make up 1/3 of known LMXBs in globular clusters, Bahramian et al. 2014), then a helium (or heavier element) atmosphere will be produced. Such helium atmospheres will have harder spectra than hydrogen atmospheres, so the inferred radii will be larger,

typically by about 50% (Servillat et al., 2012; Catuneanu et al., 2013; Lattimer & Steiner, 2014; Heinke et al., 2014). This uncertainty can be addressed by identification of the nature of the donor (e.g. by detecting Hα emission, Haggard et al. 2004, or orbital periods, Heinke et al. 2003).

This chapter extends and applies the results of chapter 3 to time-integrated spectroscopy. Specifically, we address the uncertainties inherited measuring neutron stars radii in qLMXBs based on spectral fitting. My goal in this chapter is to answer the question; how much error is incurred in calculations of the NS mass and radius by spectral fitting to a single-temperature NS, particularly for hot spots within the constraints determined in the previous chapter.

If the hot spots are not large or hot enough, or the emission geometry not favourable, the overall pulse amplitude may be too low to be detected by current observations. However, the undetected hot spots will affect the spectrum of the emitted light, typically hardening the spectrum compared to a star with a uniform temperature. If one were to fit the star's spectrum with a single temperature, the presence of undetected hot spots will cause the inferred temperature to be higher, and the inferred radius to be smaller, than their true values. The fluxes from qLMXBs are generally so low that it is difficult to conduct effective pulsation searches, leaving open the possibility of hot spots. Investigating the effect of undetected hot spots on the inferred NS radius, in the context of the qLMXBs, is our goal.

Deep (300 kilosecond) *Chandra* ACIS observations provided excellent spectra of the qLMXB X7, enabling tight constraints on X7's radius, $14.5^{+1.6}_{-1.4}$ km for an assumed 1.4 $M_\odot$ mass (Heinke et al., 2006). However, these spectra suffered from significant pileup, the combination of energies from multiple X-ray photons that land in nearby pixels during one exposure (Davis, 2001). Although a model was used to correct for this effect, this pileup model contributed unquantified systematic uncertainties to the analysis, and thus the reported constraint is no longer generally accepted (e.g. Steiner et al., 2010). A new, 180 kilosecond *Chandra* observation of 47 Tuc in 2014-2015 was taken with *Chandra*'s ACIS detector in a mode minimizing pileup effects, providing a high-quality spectrum of X7 that enables tight constraints on the radius (Bogdanov et al., 2016). Our simulated spectra are designed specifically to model the effects of hot spots on this new

spectrum of X7.

Our constraints on the pulsed fractions from X7 and X5 from Chapter 3 can enable us to place constraints on the effects of undetected hot spots upon their X-ray spectra. Naturally, these constraints are probabilistic in nature, since the orientation of the NS, and of hot spots on it, affects the probability of detecting pulsations from hot spots of a given size and temperature. We also consider what constraints may be obtained from the deeper pulsation limits from *XMM-Newton* observations of the (non-cluster) qLMXB Cen X-4 D'Angelo et al. (2015).

4.3   Effect of a Hot Spot on the Spectrum

The existence of a hot spot causes a change in the observed spectrum from the NS. We utilize the same model for a radiating NS as in Chapter 3; see that chapter for definitions of the relevant terms. To illustrate the effect of a hot spot on the spectrum we choose an extreme case, corresponding to our fiducial NS (T_{surf} =0.1 keV, 11.5 km radius, 1.4 $M_\odot$ mass) rotating at a 500 Hz spin frequency, plus a spot with $T_{spot} = 0.15$ keV, angular radius $\rho = 20°$, and emission and inclination angles $e = 85°$ and $i = 86°$. The pulse profile for this case is shown in Figure 3.2 and has a pulsed fraction of 31%. The method described in Section 3.3 is used to compute the flux from the spot and the rest of the star. We compute the spectra for each rotational phase of the neutron star over the energy range (0.2 - 10.0 keV), then we integrate the spectra over all rotational phases to produce the simulated phase-averaged spectrum. We convolve the flux from the spot and star with our interstellar medium model, then fold them over the proper response matrix and effective area of the *Chandra* ACIS-S detector. We fix the exposure time in our simulation at 200 kiloseconds (chosen to represent the 2014–2015 *Chandra* / ACIS observation of 47 Tuc), then use a Poisson distribution to select the number of counts per energy bin.

Figure 4.1 shows an example spectrum. The dashed curve shows the flux F_{NS} integrated over phase, which corresponds to the flux from all parts of a star at $T_{NS} = 0.1$ keV. The dotted curve shows the flux from the hot spot F_{spot}, at temperature 0.15 keV. The solid curve shows the observed
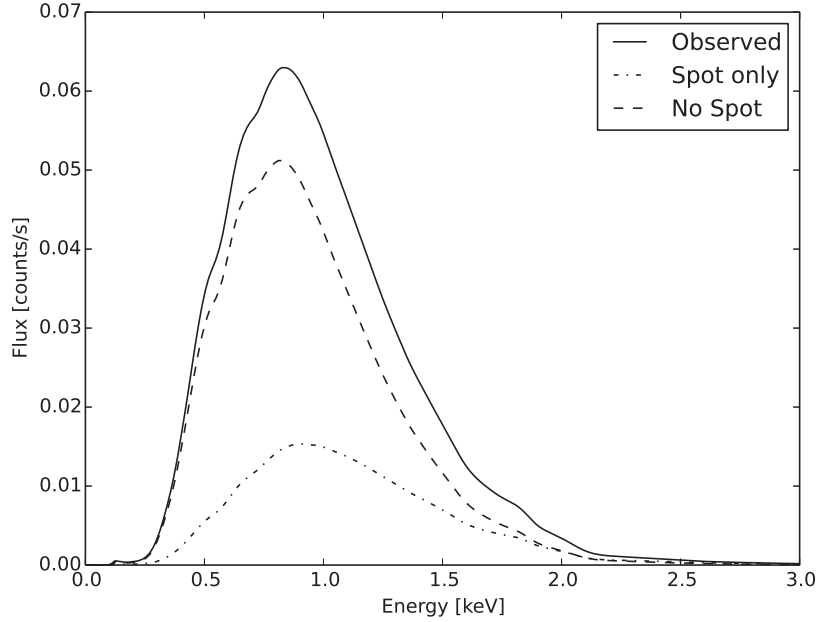
Figure 4.1: The effect of the existence of hot spots on the observed spectrum. The neutron star has a surface temperature of 0.10 keV, and the hot spot is at 0.15 keV. The peak of the spectrum slightly shifts to a higher energy by 0.02 keV. The hotter the spot is, the more distorted the spectrum will be.

flux $F_{obs} = F_{NS} + F_{spot} - F_{backspot}$. The peak of the observed spectrum is shifted by ~ 0.02 keV, and the flux increases by over 20%. The shift of the peak photon energy is smaller than the energy resolution of *Chandra* / ACIS at lower energies (of order 0.1 keV).

We now test how the spectroscopically inferred radius changes if the star has a hot spot, but the spectral fitting assumes that the star's emission is homogeneous. We simulated spectra for the fiducial star with $M = 1.4\ M_\odot$, $R = 11.5$ km, $T_{NS} = 0.1$ keV, $d = 4.6$ kpc, $f = 500$ Hz, and $N_H = 1.3 \times 10^{20}$ cm^{-2} with a hot spot on the surface. We chose a variety of temperature differentials and spot sizes (assuming the polar cap model), as shown in Table 4.1. For each model, we use the HEASOFT tool `FLX2XSP` to convert the flux array to a PHA spectrum, which we load into `XSPEC` to fit. We let R and T_{NS} be free in the spectral fit, while we fix the mass at $M = 1.4\ M_\odot$ and the distance $d = 4.6$ kpc. We allow N_H to be free, but with a minimum value of 1.3×10^{20} cm^{-2}. The resulting `XSPEC` fitted values and uncertainties for the radius and temperature are shown along

68

with the reduced chi-squared in Table 4.1.

The first row in Table 4.1 shows the uncertainty inherent in the method, by first simulating a light curve for a star with no hot spot; the best-fit radius is quite close (0.1 km) to the input value, and the radius uncertainty (0.7-0.8 km) is consistent with that from fitting to real data on X7 (Bogdanov et al. 2016). Next, we see that there is a systematic trend in the inferred radii of the neutron stars introduced by an undetected hot spot. XSPEC interprets the shifted spectrum as an increase in the temperature of the whole star. However, the observed flux will not be as large as one would expect for the higher temperature, so this is interpreted as indicating a smaller star. The general result is that the star's radius is under-estimated when an undetected hot spot is present. This effect can be seen in many of the best-fit solutions shown in Table 4.1. The principal factor in introducing bias is the spot temperature; a 15% bias in the average fitted temperature is induced by spot temperatures of 0.14 to 0.15 keV, for spot sizes between 9° and 23°. For this reason, we focus on the spot temperature as the crucial variable to explore below.

Table 4.1 only shows results for one particular choice of emission and inclination angles. For a more general picture, for each value of T_{spot} we simulated 300 spectra with emission and inclination angles drawn from distributions uniform in $\cos i$ and $\cos e$ for the fiducial star, assuming a 500 Hz spin, a 1.4 $M_\odot$ mass, and a radius of 11.5 km. Each simulation was fit in XSPEC using the same method used for Table 4.1. The resulting 90% confidence limits on the radius from each simulation are indicated by coloured dots in Figures 4.2. Each graph shows the results for a particular spot temperature and has four regions, separated by black lines indicating the input value of the neutron star's radius R used in the simulation (the "true" radius). The region with $R_{\max} \geq R$ and $R_{\min} \leq R$ (lower right-hand quadrant) corresponds to fits that are consistent with the correct radius. The points in the region with $R_{\min} > R$ (upper right-hand quadrant) are fits that overestimate the neutron star's radius, while the points in the region with $R_{\max} < R$ (lower left-hand quadrant) underestimate the radius. The fourth region, shaded grey, is forbidden since it corresponds to $R_{\min} > R_{\max}$.

To determine whether the spectral distortion due to a hot spot would be detectable, and thus whether NSs with hot spots might be identified by their poor fits to single-temperature models, we

retained fit quality information for each fit. We define each fit with a reduced chi-squared value greater than 1.1 (which indicates a null hypothesis probability less than 0.044, given the 51 degrees of freedom) to be a "bad" fit, and mark it as a red cross. Unfortunately, the fraction of "bad" fits does not increase substantially with increasing hot spot temperature (Fig. 4.2, and Table 4.2), indicating that fit quality cannot effectively identify spectra with hot spots.

Each simulation also has an associated pulsed fraction. If the pulsed fraction is larger than the measured upper-limit for X7 (for an assumed spin of 500 Hz), we marked it as a black hollow circle. Good fits that do not violate the pulsed-fraction limit are marked as a green triangle. For spot temperatures up to 0.125 keV we find that over 75% of the simulations give inferred radii that are consistent with the true value of R_{NS}. For higher temperature differentials ($T_{spot} > 0.13$ keV) a large fraction of the inferred radii are biased downward from the "true" value by larger than 10% of the true radius of the neutron star, while the majority ($>58\%$) of the simulations are below the X7 pulse fraction upper limit. This pulse fraction limit, and the inferred bias, changes if the spin frequency (and consequently the spot size) changes. For the higher spin frequency of 716 Hz we find that inferred radii can be biased up to 15% smaller than the true radius of the neutron star for $T_{spot}=0.13$ keV. In Table 4.2, we summarize the percentage of inferred radii consistent with the "true" value, the percentage of good fits, and the average bias in the inferred radius for different choices of spot temperature. We examined the behaviour of $(R_{max}+R_{min})/2$ vs. R_{fit}, finding a well-behaved linear relationship between the two quantities. In this paper we calculate the bias as the difference between the median of the inferred $R_{fit, no spot}$ radii with no hot spots and the median of the inferred radii $R_{fit, spot}$ with a hot spot, divided by the latter. (This definition allows this bias to be directly applicable to observed radius estimates). The $R_{fit, no spot}$ values are results of fitting 300 simulated spectra from a poisson distribution, which would give a distribution of R_{fit} peaked at the *true* value of $R = 11.5$ km.

In Fig. 4.3 we present histograms of the inferred R_{fit} at different spot temperatures, and compare it to the distribution of inferred R_{fit} with no spot. This shows the bias in the mean between the histogram with no spot and the histogram of inferred radii with a hot spot. For a spot temperature as

high as 0.125 keV, the bias in R_{fit} is still at or below 5%. At 0.130 keV, the majority of simulations do not violate the pulse fraction limit, the bias in the mean is 10%, and over half the fits are consistent with the input radius. For the maximum spot temperature we allow in our simulations, the bias in the mean of R_{fit} can reach up to 40%, however < 10% of the simulations at this spot temperature are below the upper limits for either X7 or Cen X-4.

To identify a reasonable limiting case, we choose the T_{spot} where less than 10% of the simulations provide pulse fractions below the upper limit on each neutron star's pulse fraction; thus, 0.155 keV for X7, and 0.130 keV for Cen X-4. This allows a maximum downward bias in their spectroscopically inferred radii of up to 28% for X7, and 10% for Cen X-4. For example, if we assume the neutron star in Cen X-4 to be a 1.4 $M_{\odot}$ star spinning at 500 Hz with a spectroscopically inferred radius of exactly 11.5 km, an undetected hot spot could allow a true radius as high as 12.65 km. For X7, in the case of maximal undetected hot spots, the measured radius of $11.1^{+0.8}_{-0.7}$ km (for an assumed 1.4 $M_{\odot}$ neutron star mass, Bogdanov et al. 2016) could allow a true radius up to 15.2 km in the extreme case. In Fig. 4.4 we summarize the bias in R_{fit} versus spot temperature at 500 Hz and 716 Hz frequencies. At both frequencies, the bias is below 10% for relatively small spot temperatures (up to 0.125 keV). However, at higher spot temperatures (> 0.130 keV) there is a clear divergence between the magnitude of the biases at 500 Hz and 716 Hz, becoming larger with spot temperature. Increasing the frequency from 500 to 716 Hz changes the bias from 32% to 41% at the highest spot temperature (0.160 keV), but since the 716 Hz frequency also has a larger pulsed fraction for the same spot temperature, the maximum spot temperature is reduced in the 716 Hz case, and the actual maximum bias in the 500 and 716 Hz cases is similar. Finally, we ran the simulations with choices of a uniform distribution of e and $\cos i$. This produces lower pulsed fractions when compared to simulations using a uniform distribution of $\cos e$ at the same spot temperature (see numbers in parentheses in Table.4.2) . In turn, this increases the maximum allowable spot temperature that would not give rise to detectable pulsations. For X7, the maximum spot temperature for an assumed uniform distribution of e is larger than 0.160 keV (the limit of our model), while the maximum spot temperature for Cen X-4 would be 0.155 keV, both at the spin frequency of 500

Hz. A hot spot temperature larger than 0.160 keV would give a spectroscopically inferred radius less than 50% of the true radius, which essentially means the bias is not usefully bounded.

T_{spot}	ρ	f	PF	R_{fit}	$\text{Log}T_{\text{eff,fit}}$	χ^2_ν
[keV]	[°]	[Hz]	[%]	[km]		
...	...	...	...	$11.4^{+0.8}_{-0.7}$	$6.05^{+0.02}_{-0.02}$	0.99
0.13	9	100	3.3	$11.4^{+1.3}_{-0.8}$	$6.04^{+0.02}_{-0.02}$	1.09
0.15	9	100	9.0	$9.7^{+1.1}_{-0.6}$	$6.09^{+0.02}_{-0.02}$	1.09
0.11	20	500	5.5	$11.8^{+1.3}_{-0.8}$	$6.03^{+0.03}_{-0.02}$	1.10
0.12	20	500	9.8	$11.6^{+0.9}_{-0.8}$	$6.04^{+0.02}_{-0.02}$	0.82
0.13	20	500	18.0	$10.9^{+0.8}_{-0.8}$	$6.07^{+0.02}_{-0.02}$	1.15
0.14	20	500	25.2	$9.8^{+0.8}_{-0.6}$	$6.10^{+0.02}_{-0.02}$	1.04
0.15	20	500	30.8	$9.3^{+0.8}_{-0.8}$	$6.11^{+0.02}_{-0.02}$	1.01
0.11	23	667	7.7	$11.6^{+0.8}_{-0.8}$	$6.04^{+0.02}_{-0.02}$	1.06
0.12	23	667	13.9	$10.9^{+0.8}_{-0.6}$	$6.06^{+0.02}_{-0.02}$	0.70
0.13	23	667	24.5	$10.9^{+1.1}_{-0.8}$	$6.07^{+0.02}_{-0.03}$	0.98
0.14	23	667	33.2	$9.1^{+0.9}_{-0.6}$	$6.13^{+0.02}_{-0.02}$	1.18
0.15	23	667	39.5	$8.8^{+1.0}_{-0.4}$	$6.14^{+0.03}_{-0.02}$	1.40

Table 4.1: Best-fit values of R and T_{eff} for given choices of T_{spot}, spot size ρ, spin frequency, and constant angles $i = 80°$ and $e = 89°$. The spectra are generated assuming $M = 1.4\,M_\odot$, $R = 11.5$ km, surface temperature T_{NS}=0.10 keV, $\log T_{\text{NS}} = 6.06$. Errors are 90% confidence. Spectral fits assume $M = 1.4\,M_\odot$ and $d = 4.6$ kpc. The pulse fractions produced by each simulation are provided for reference.

T_{spot}	f	< X7 limit	< Cen-X4 limit	Consistent	Good fits	Bias
[keV]	[Hz]	[%]	[%]	[%]	[%]	[%]
0.105	500	100 (100)	100 (100)	93	79	−0.3
0.110	500	100 (100)	100 (100)	92	75	−0.4
0.115	500	100 (100)	87 (89)	90	78	−1
0.120	500	100 (100)	45 (56)	84	73	−2
0.125	500	100 (100)	22 (34)	76	69	−5
0.130	500	58 (64)	10 (26)	55	73	−10
0.135	500	33 (47)	8 (20)	38	72	−14
0.140	500	24 (38)	7 (16)	19	71	−17
0.145	500	21 (33)	6 (14)	15	69	−20
0.150	500	17 (31)	5 (12)	9	76	−22
0.155	500	12 (28)	3 (10)	5	71	−28
0.160	500	8 (23)	2 (8)	0.6	57	−32
0.105	716	100	100	89	77	−1
0.110	716	100	73	87	79	−2
0.115	716	100	32	86	78	−3
0.120	716	100	21	79	79	−3
0.125	716	63	9	62	79	−8
0.130	716	32	7	33	77	−13
0.135	716	22	6	16	74	−19
0.140	716	17	4	10	72	−23
0.145	716	13	3	5	67	−26
0.150	716	10	3	4	65	−31
0.155	716	8	2	2	56	−38
0.160	716	7	2	0.6	57	−41

Table 4.2: For different spot temperatures, the bias (right column) in radius determinations, and the percentages of simulations that lie under the upper limits on the pulsed fraction for X7 and Cen X-4, that give spectral fits consistent with the "true" radius, and that give "good" fits ($\chi_\nu^2 < 1.1$). Each line gives results from fitting 300 simulated spectra using $R = 11.5$ km and surface temperature $T_{NS} = 0.10$ keV, for different choices of spot temperatures and spin frequency. Spectral fits assume $M = 1.4\ M_\odot$ and $d = 4.6$ kpc. The percentage of "good fits" are the percentage of the simulations below the upper limits. Numbers in brackets are for simulations performed with a uniform distribution of e (rather than uniform in $\cos e$).
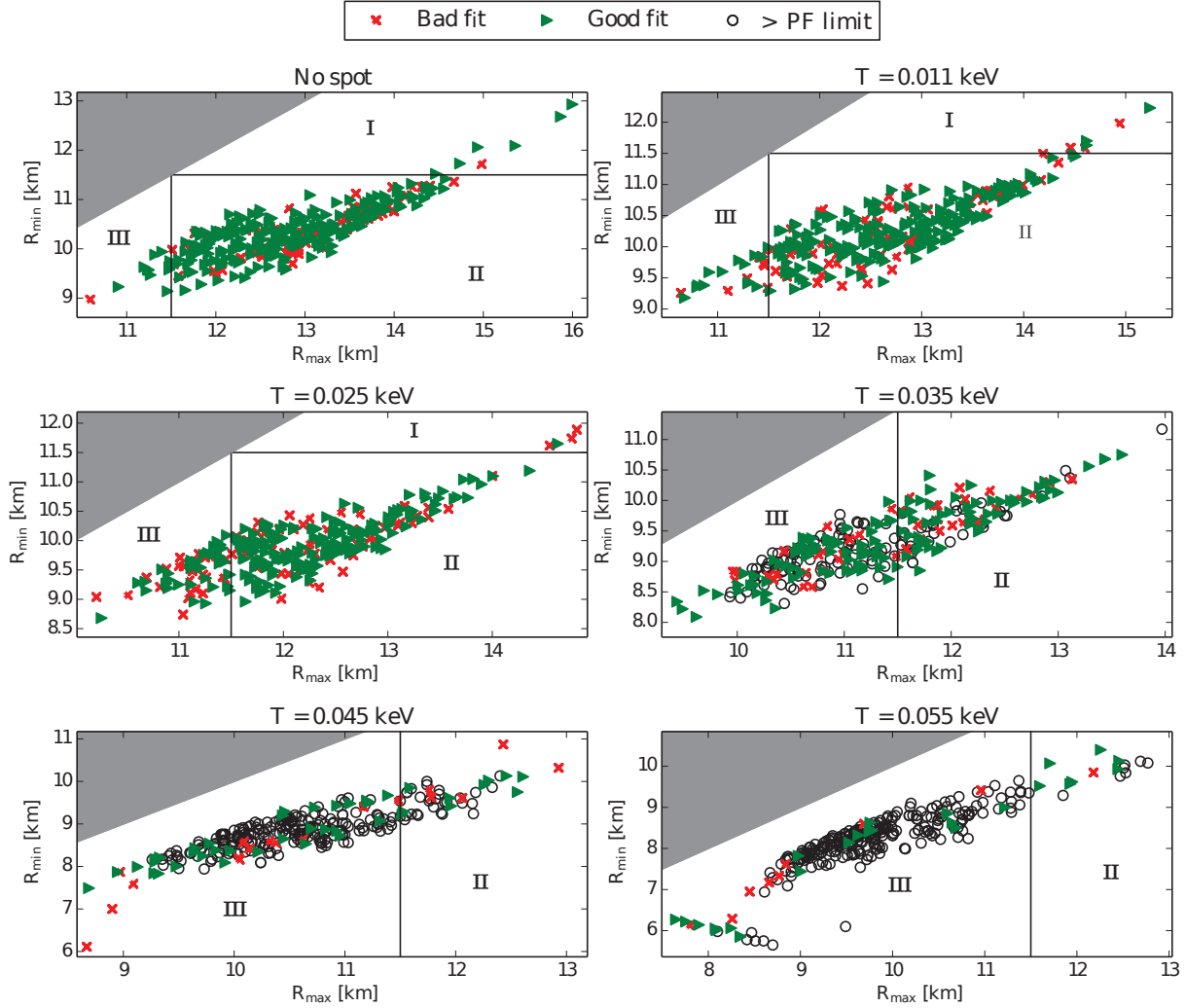
Figure 4.2: Calculated upper and lower radius limits (90% confidence) from fitting 300 spectral simulations with different choices of the temperature differential, assuming a 1.4 $M_\odot$ NS, with the angles e and i chosen from distributions uniform in $\cos i$ and $\cos e$. The shaded area is prohibited, and the solid lines represent the "true" (input to simulation) value of the neutron star radius, $R_{NS} = 11.5$ km. Points in the lower right quadrant of each graph indicate fits where the "true" (input) radius falls between the inferred upper and lower radius limits, while points in the lower left quadrant show a radius upper limit below the "true" value. The results shown here are directly applicable to the neutron star X7 in 47 Tuc, which has a 90% upper limit of 13% on the pulsed fraction.
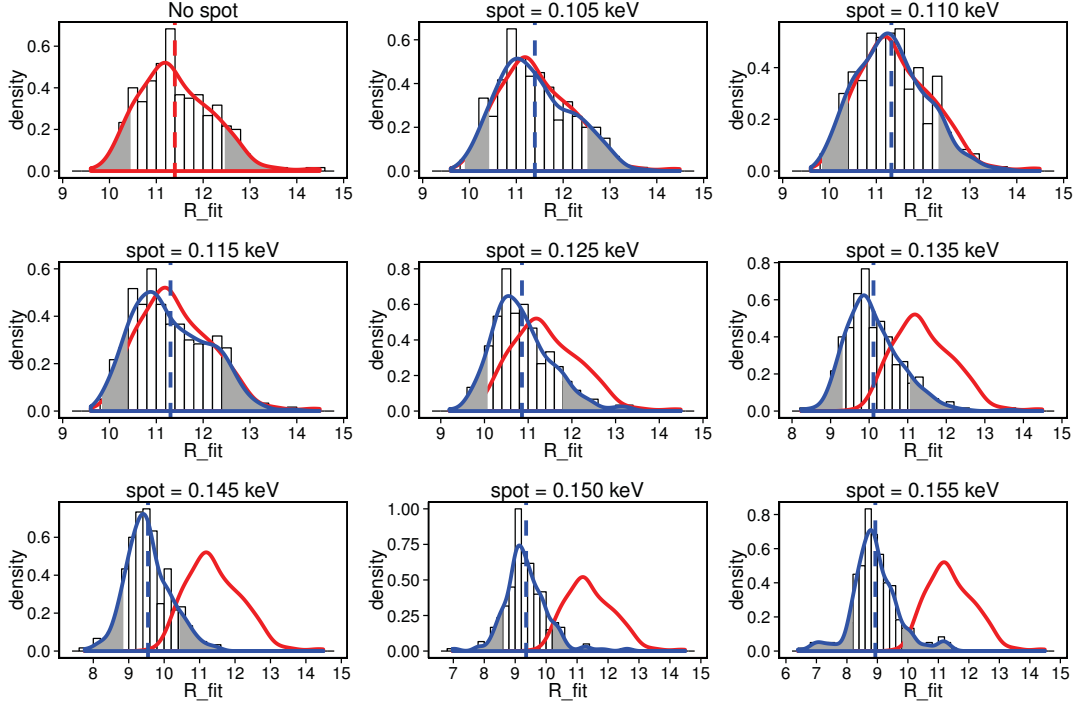
Figure 4.3: Distribution of (R_{fit}) from fitting 300 spectral simulations for different choices of the temperature differential, assuming a 1.4 $M_\odot$ NS, with the angles e and i chosen from distributions uniform in $\cos i$ and $\cos e$. The red curve is the probability density curve for the simulations without a hot spot (essentially the systematic errors inherent in the method), while the blue curve indicates the probability density of the inferred R_{fit} at each hot spot temperature. The dashed line is the mean of (R_{fit}). The shaded grey areas exclude the upper and lower 10% of each probability density curve. The theoretical model is for a 11.5 km neutron star spinning at 500 Hz. These histograms show the bias in radii measurements.
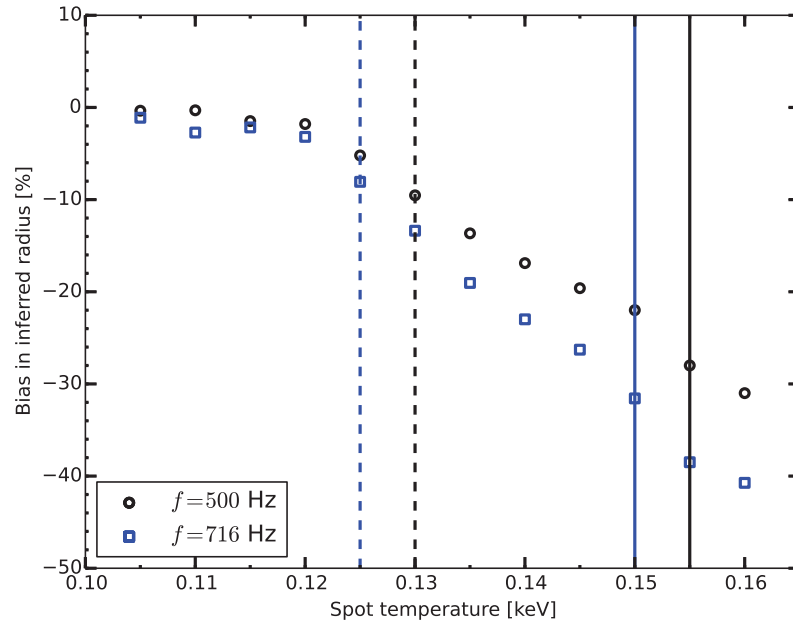
Figure 4.4: Bias in the spectroscopically inferred R_{max} (90% confidence) as a function of the spot tempera-
ture relative to a NS at surface temperature of 0.100 keV. The black colour is associated spinning
frequency of 500 Hz and the blue colour is associated the 716 Hz. The solid and dashed lines
are the maximum allowable spot temperatures that would not give rise to detectable pulsations
based on the pulse fraction limits for X7 and Cen-X4 respectively.

4.3.1   Limits of our analysis

Our analysis necessarily is limited in scope. Here, we enumerate some complexities that we have not addressed in this work. The temperature distribution of the hot spots may be more complex than we have assumed; especially for large spots, this might cause significant changes (see, e.g. Bauböck et al., 2015b). We have sampled only a few values of the spin period, mass, and radius. We have assumed hydrogen atmospheres; helium atmospheres, while generally similar in spectra and angular dependences, have some subtle differences (see Zavlin et al., 1996, figures 5 and 9). These issues are unlikely to significantly alter our results.

A larger issue is that we assume that the neutron star has only one spot. A second spot would reduce the average pulsed fraction, though it would probably not reduce the lower limit on the pulsed fraction substantially (see chapter 3 for an explanation). The second spot would generally increase the visible amount of the star at a higher temperature, so it would increase the bias in the radius. Some NSs have strong evidence for poles that are not offset by 180 degrees (e.g. Bogdanov, 2013), and/or with different sizes and temperatures (Gotthelf et al., 2010), adding additional possible complexity.

Another major issue is that the distribution of e may not be uniform in either $\cos e$ or in e; if hot spots are more concentrated towards the poles than we assume (as suggested by Lamb et al. 2009), then the pulsed fractions will tend to be lower than we assume.

A final issue, relating to the applicability of our results to other systems, is that our simulations were designed with surface temperature and extinction (N_H) designed to match specific qLMXBs in 47 Tuc. Increased N_H would tend to obscure the softer emission from the full surface more than the hot spot, thus increasing the expected pulse fraction and the expected bias in spectral fitting.

4.4   Summary

We studied the effects on the inferred radius of hot spots for these temperature differential limits. We find that the existence of an unmodeled hot spot tends to shift the peak of the spectrum to higher

energies, which reduces the spectroscopically inferred equatorial radii of neutron stars below the "true" radius. The 90% confidence range of the inferred radii are generally still consistent with the true value of our fiducial star (11.5 km) for small temperature differentials (0.03 keV).

For the hottest possible hot spots that would not give rise to detectable pulsations in X7, we find that a bias in the best-fit inferred radius of up to 28% smaller than the true radius may be induced by hot spots below our upper limit. For Cen X-4 (where the pulse fraction constraint is much tighter, $<6.4\%$), downward radius biases are constrained to $< 10\%$. If the hot spot emission angle e is distributed uniformly in e (rather than in $\cos e$, as appropriate if the hot spot may be anywhere on the neutron star surface), then the constraints are significantly looser, and effectively unbounded for the X7 case.

Our analysis constrains a key systematic uncertainty in the most promising radius measurement method. We do not know whether quiescent neutron stars in X-ray binaries without radio pulsar activity have hot spots. However, the possibility strongly motivates further pulsation searches in quiescent neutron stars in X-ray binaries, particularly those that are targets for spectroscopic radius determination.

Chapter 5

The Soft X-ray Spectrum of the High Mass X-Ray Binary V0332+53 in Quiescence

5.1 Introduction

Accreting X-ray pulsars (XRPs) in high mass X-ray binaries (HMXBs) provide an excellent laboratory for accretion physics. The strong ($B \sim 10^{11-13}$ G) neutron star (NS) magnetic field means that the NS's magnetosphere determines the conditions of the accretion flow. The magnetospheric radius is defined to be where the pressure of the magnetic field $B(r_m)^2/8\pi$ equals the ram pressure of the infalling matter, $\rho(r_m)v(r_m)^2$. At this radius, matter is thought to thread itself onto magnetic field lines. If this magnetospheric radius becomes larger than the corotation radius $R_c = (GMP^2/4\pi^2)^{1/3}$, where the Keplarian angular velocity of infalling matter matches the angular velocity of the spinning NS, the infalling matter will not be moving fast enough to join the magnetic field lines (Illarionov & Sunyaev, 1975). This is the *propeller* regime, where the accretion is stopped, or at the very least greatly reduced, when the accretion rate falls below the minimum threshold value of

$$L_{min} = 1.6 \times 10^{37} R_{12}^2 M_{1.4}^{-2/3} B_{12}^2 P_1^{-7/3} \, erg \, s^{-1} \qquad (5.1)$$

where $B_{12}, R_{12}, M_{1.4}$ and P_1 are the NS's surface magnetic field in the units of $10^{12}G$, radius in units of 12 km, mass in units of 1.4 $M_\odot$ and spin period in units of seconds, respectively (Stella et al.,

1986).

Rapid drops in L_x by a factor > 100 during the late stages of an outburst have been seen in several systems, and interpreted as marking the transition to the propeller regime. Some examples include XRPs in HMXBs like 4U 0115+63 and V0332+53 (Campana et al., 2001; Stella et al., 1986; Tsygankov et al., 2016), low magnetic field ($B \sim 10^8 - 10^9$ G) fast-spinning NSs in low-mass X-ray binaries such as Aquila X-1 (Campana et al., 1998c, 2014), SAX J1808.4-3658 (Campana et al., 2008), and XTE J1701-462 (Fridriksson et al., 2010), and the bursting pulsar GRO J1744-28, with an intermediate-strength ($B \sim 5 \times 10^{11}$ G) magnetic field (Cui, 1997). Understanding the transition to the propeller regime is important for understanding the luminosity function of X-ray binary populations (Shtykovskiy & Gilfanov, 2005) and the spin-up of millisecond radio pulsars (e.g. Tauris et al. 2012, Papitto et al. 2014, Archibald et al. 2015).

For a system in the propeller regime, there are a few candidates for the mechanism of continued X-ray emission. If the propeller effect is not 100% effective, calculations have suggested that a small amount of matter ($\sim 1\%$) may penetrate the magnetosphere, and reach the surface of the NS producing X-ray emission, while the majority of matter is ejected (e.g. Stella et al. 1986). Magnetohydrodynamics simulations (e.g. Romanova et al. 2004) agree with this basic picture, providing a possible explanation for continued luminosity in quiescence, which is predicted to be pulsed (see below).

This low-level accretion luminosity may show a similar spectrum to that at higher L_x, or resemble a hot, small-radius blackbody, indicating hot polar caps, as seen in some radio pulsars (e.g. (Zavlin & Pavlov, 1998; Özel, 2013)). Emission from the hot neutron star surface will generate a blackbody-like thermal spectrum, shifted slightly to higher energies by passage through the hydrogen atmosphere, depending on the magnetic field strength (Pavlov et al., 1995). The neutron star core is expected to be heated by accretion during outbursts, providing a steady-state heat flux to the surface during quiescence (Brown et al., 1998). Alternatively, X-ray flux might be generated by accretion down to the magnetosphere, providing a luminosity a factor $L(r_m)/L(R) = 2r_{cor}/R_{NS} \sim 1000$

lower than accretion onto the neutron star surface, and unpulsed (e.g. Campana et al. 1998a). However, accretion down to the magnetosphere is not certain to produce X-rays, and can be ruled out for some XRPs in quiescence (e.g. A 0535+26, Negueruela et al. 2000). Finally, in some cases the O or B companion star may generate soft X-rays at the level of 10^{31-33} erg s^{-1}, which may be detectable in deep quiescence as a line-dominated thermal spectrum. Accurate measurements of the spectrum and pulse fraction can determine what role each of these play in the quiescent emission.

The heating of the NS core during outbursts should lead to thermal X-ray emission from the entire NS surface in quiescence, unless strong neutrino emission is present (e.g. Yakovlev et al., 2003; Heinke et al., 2007; Wijnands et al., 2013). The luminosity expected depends on the long-term average accretion history, and on the mass of the neutron star, and may lie in the range $\sim 10^{31}$–10^{33} erg s^{-1}.

The magnetic fields are known (by X-ray cyclotron line measurements) for some XRPs in HMXBs, and some XRPs have been observed at L_x that are well within the propeller regime. Three HMXBs with known B fields, distances and spin periods have X-ray measurements that are clearly in the propeller regime: A0535+262 (Negueruela et al., 2000; Mukherjee & Paul, 2005; Rothschild et al., 2013; Doroshenko et al., 2014); V0332+53 (Stella et al., 1986; Campana et al., 2002); and 4U 0115+63 (Campana et al., 2001, 2002). Observations of A0535+262 with various telescopes showed clear pulsations and a spectrum describable by a cutoff power-law (photon index ~ 0.4, $E_{fold} \sim$ 4-6 keV) while in the propeller regime (e.g. Doroshenko et al., 2014). The other two systems, which are significantly more distant, have only weak constraints on their quiescent spectra and pulsations from BeppoSAX (Campana et al., 2002). Several other systems have published observations which have been claimed to likely be in the propeller regime, but in these cases the magnetic field is less certain (e.g. A 0538-668, Campana et al. 2002; GX 1+4, Cui & Smith 2004; Vela X-1, Doroshenko et al. 2011). The systems 4U 1145-619 (Mereghetti et al., 1987; Rutledge et al., 2007) and 1A 1118-615 (Rutledge et al., 2007) have been observed to show pulsations and hard power-law spectra when $L_X \sim 2 - 3 \times 10^{34}$ erg/s, with photon indices ~ 0.8–1.6.

Several other XRP systems show evidence of thermal blackbody-like emission while at low X-

ray luminosities. SAX J2103.5+4545 (Reig et al., 2014) demonstrated X-ray pulsations and a $\sim$1 keV blackbody thermal spectrum at $L_X = 1.2 \times 10^{33}$ erg s^{-1}. No variation other than the pulsations were seen. It is unclear if this NS is in the propeller state, since the B field is not accurately known, but it was suggested that the observed X-rays are from hot spots still cooling from the latest outburst. Soft thermal components to XRP X-ray spectra around 10^{34-35} erg s^{-1} have been observed from RX J0146.9+6121 (La Palombara & Mereghetti, 2006), 4U 0352+309/ X Per (La Palombara & Mereghetti, 2007), and RX J1037.5-5647 (La Palombara et al., 2009), suggesting the presence of hot spots on NSs. In no low-luminosity XRP X-ray spectrum has a thermal component consistent with emission from the full NS surface been unambiguously detected.

V0332+53 is a transient XRP in a 33.85-day orbit (Doroshenko et al., 2016) with a Be-type companion, spectroscopically classified as O8-9Ve (Negueruela et al., 1999). The NS spin period is 4.35 s (White et al., 1983), and its magnetic field has been measured (through detection of a cyclotron line) to be 2.7×10^{12} G (Makishima et al., 1990; Pottschmidt et al., 2005). It is thought to be at a distance of roughly 7 kpc (a plausible range includes 6-9 kpc), based on spectral typing of the companion star (Negueruela et al., 1999). V0332+53 was first detected during a large outburst in 1973 by the *Vela 5B* satellite (Terrell & Priedhorsky, 1984). It has since been observed in outburst in 1983 (Tanaka, 1983; Stella et al., 1985), in 1989 (Makishima et al., 1990), in 2004 (Kreykenbohm et al., 2005; Pottschmidt et al., 2005), in late 2008 (Caballero-Garcia et al., 2015), and in 2015 (Tsygankov et al., 2016; Wijnands & Degenaar, 2016). Between outbursts, V0332+53 still gives off X-rays, but at only a small fraction of its outburst luminosity (Campana et al., 2002). We proposed an XMM-Newton observation to determine the shape of its spectrum in quiescence, and search for pulsations.

5.2 Spectral Analysis

We observed V0332+53 with *XMM-Newton* for 39 ks on Feb. 10th, 2008 (ObsID 0506190101). This is at orbital phase 0.7 after periastron, according to the ephemeris of Doroshenko et al. (2016).

Here we discuss only the data obtained with the pn (Strüder & et al., 2001) and MOS (Turner & et al., 2001) cameras. We used SAS v13.5.0 software package to reduce the data. We filtered the data to the range of 0.2 − 10 keV for all three cameras. We created lightcurves from all data from each camera, binned to 50 second bins, to filter out times of high background rates due to soft proton radiation. We removed times with event rates higher than 0.16, 0.12 and 0.2 counts/s for the MOS1, MOS2 and pn cameras respectively, which removed 2 ks from the observation time. We used a circle of radius $10''$ to extract the source, and a $15''$ circle for the background. We created appropriate response files and effective areas for each camera, for source and background.

We grouped the data at three different trial values of 15, 20 and 25 counts/bin. We adopted a grouping of 20 counts/bin for our analysis for the three cameras. We combined the extracted spectra from MOS1 and MOS2 into one spectrum and fit it simultaneously with the spectrum extracted from the pn camera, using several different models (`nsa, nsa[pole], nsa[pole]+pow, pow, nsa[pole]+nsa`), with the details of the spectral fits listed in Table 1, and discussed below. All models included extinction, using the `tbabs` model, with *wilm* abundances (Wilms et al., 2000), which we left a free parameter. The `nsa` model is a neutron star atmosphere model, including appropriate physics for magnetic fields of 10^{12} or 10^{13} G (Pavlov et al., 1995). We fixed the magnetic field at $B = 10^{12}$ Gauss for our fits. In all fits using `nsa`, we fixed the NS mass to 1.4 $M_\odot$, and the NS radius to 11 km. We froze the normalization value ('norm', which gives the angle on the sky) to $K = 2.04 \times 10^{-8}$ pc^{-2} (implying an 11 km NS and a distance of 7.0 kpc) when we were modeling emission from the entire star with the `nsa` model. When we modeled emission from polar caps (we refer to this as `nsa[pole]` models), we allowed this parameter to vary.

We may predict N_H from the optical extinction, using $N_H = (E_{B-V})(R_V)(2.8 \times 10^{21})$ (Bahramian et al., 2015; Foight et al., 2015). For V0332+53, E_{B-V} has been measured by the strength of diffuse interstellar bands to be 1.88±0.1 (Corbet et al., 1986), and, by comparing the spectral classification with the observed colour, to be 1.87 (Negueruela et al., 1999). We can then estimate $N_H = 1.6 \times 10^{22}$ cm^{-2}. However, X-ray observations have given values of N_H varying between 6×10^{21} and 1.5×10^{22} cm^{-2} (Stella et al., 1985, note these N_H measurements were on a different

abundance scale), or between $1.0-1.3 \times 10^{22}$ cm^{-2} (Tsygankov et al., 2016). Possibly the extinction may be smaller towards the NS vs. its companion (not implausible, given the excretion disk). We left N_H a free parameter.

A power-law model, typical of HMXB outburst spectra, provides a reasonable fit, with a reduced chi-squared of 0.81, but an extremely steep best-fit photon index of $4.4^{+0.9}_{-0.7}$, strongly implying that the emission is thermal in origin. The `nsa` model also does not produce an adequate fit, with a reduced chi-squared of 2.6 for 20 degrees of freedom. This suggests that we do not see emission from the neutron star's entire surface. We then consider emission from a small region on the surface of the neutron star, the heated polar cap(s), by allowing the `nsa` normalization to be free (the `nsa[pole]` model). This gives a reasonable fit, with a reduced chi-squared of 0.98. The N_H in this model is constrained to $0.7\pm0.2 \times 10^{22}$ cm^{-2}, which is interestingly low compared to the optical estimate. The `nsa[pole]` model gives a rough estimate of the radius of the emitting region of $R_{spot} = 0.27^{+0.22}_{-0.10}$ km, which may suggest the radius of the heated polar cap. This is comparable to, if a little larger than, the predicted radius for the polar cap of a pulsar with spin period of 4.35 seconds and radius 11 km, of 80 m (Lyne et al., 2006). Note that even if the poles were illuminated only over an 80-m region, a larger portion of the surface may be heated by conduction, as suggested for several pulsars (e.g. Zavlin & Pavlov, 1998; Zavlin, 2006), though the high magnetic field will limit the thermal conductivity perpendicular to the B field lines (Hernquist, 1985).

We also test two models adding additional, physically motivated components to the nsa[pole] model. We first tried adding a power-law component (with fixed $\Gamma = 1.5$, due to our limited statistics) to the `nsa[pole]` model. Such a power law might be predicted for X-ray emission from continuing accretion, as seen in low-mass X-ray binaries, and suggested as a possible spectral shape during the late decay of V0332+53's 2015 outburst (Wijnands & Degenaar, 2016). This also gives an adequate fit, though not a better one (one bin is marginally improved), and an F-test indicates that adding the additional component is not justified for the improvement in spectral quality. We also added thermal emission from the entire NS, thus a nsa[pole]+nsa model. This fit, although more of an improvement, was also not justified in terms of the quality of the spectral fit (an F-

Table 5.1: Spectral analyses of V0332+53. Errors are 90% confidence, and are not calculated if χ^2_ν exceeds 2.0. L_x is given for the 0.5-10 keV range, while $L_{bol,th}$ gives the 0.1-10 keV luminosity for thermal components, both for an assumed distance of 7 kpc. R_{emit} is a rough estimate of the emitting radius, defined as the square root of the nsa normalization times distance (in parsecs), multiplied by the assumed NS radius.

Parameter/Model	pow	nsa	nsa[pole]	nsa[pole]+pow	nsa+nsa[pole]
$N_H[\times10^{22}\text{cm}^{-2}]$	$2.6^{+0.8}_{-0.6}$	3.34	$1.00^{+0.45}_{-0.31}$	$1.19^{+0.58}_{-0.45}$	$2.06^{+0.62}_{-1.19}$	–
$\text{Log}T_{eff}[K]$	...	6.25	$6.77^{+0.07}_{-0.10}$	$6.69^{+0.13}_{-0.17}$	$6.14^{+0.05}_{-6.14}$	$6.82^{+0.11}_{-0.12}$
χ^2_ν/dof	0.81/20	2.60/20	0.87/19	0.88/18	0.80/18	-
Γ	$4.4^{+0.9}_{-0.7}$	...	...	(1.5)	...	...
R_{emit}, km	...	(11)	$0.27^{+0.22}_{-0.10}$	$0.36^{+0.72}_{-0.17}$	(11)	$0.21^{+0.21}_{-0.12}$
$L_{x,unabs}[\text{erg s}^{-1}]$	$4.9^{+1.0}_{-1.0} \times 10^{33}$	3.5×10^{33}	$3.7^{+1.1}_{-0.5} \times 10^{32}$	$4.4^{+2.1}_{-0.6} \times 10^{32}$	$1.07^{+0.94}_{-1.07} \times 10^{33}$	$3.6^{+1.2}_{-1.1} \times 10^{32}$
$L_{bol,th}[\text{erg s}^{-1}]$	...	5.2×10^{33}	$3.9^{+1.3}_{-0.6} \times 10^{32}$	$4.0^{+2.8}_{-0.6} \times 10^{32}$	$1.96^{+1.33}_{-1.96} \times 10^{33}$	$3.7^{+1.4}_{-1.2} \times 10^{32}$

Figure 5.1: RXTE/ASM and Swift/BAT lightcurves for V0332+53. Daily measurements for both were converted to Crab units, and assuming a power-law spectrum between 0.1 keV - 100 keV, with photon index of 2 converted to bolometric fluxes.

test gives an F-statistic of 2.79, and probability 0.11 of obtaining such a spectral improvement by chance), but it is useful for permitting a constraint upon thermal emission from the NS (see the Discussion). The spectra, fit to this model, are shown in Fig. 5.3.

For completeness, we also tested how our results would be affected if we used the $B = 10^{13}$ G nsa model, instead of the 10^{12} G model. The nsa[pole], 10^{13} G model still provides a good fit (χ^2_ν=0.82), with a smaller temperature (log T_{eff}=6.56$^{0.53}_{-0.38}$) and a larger radius (0.9 km).
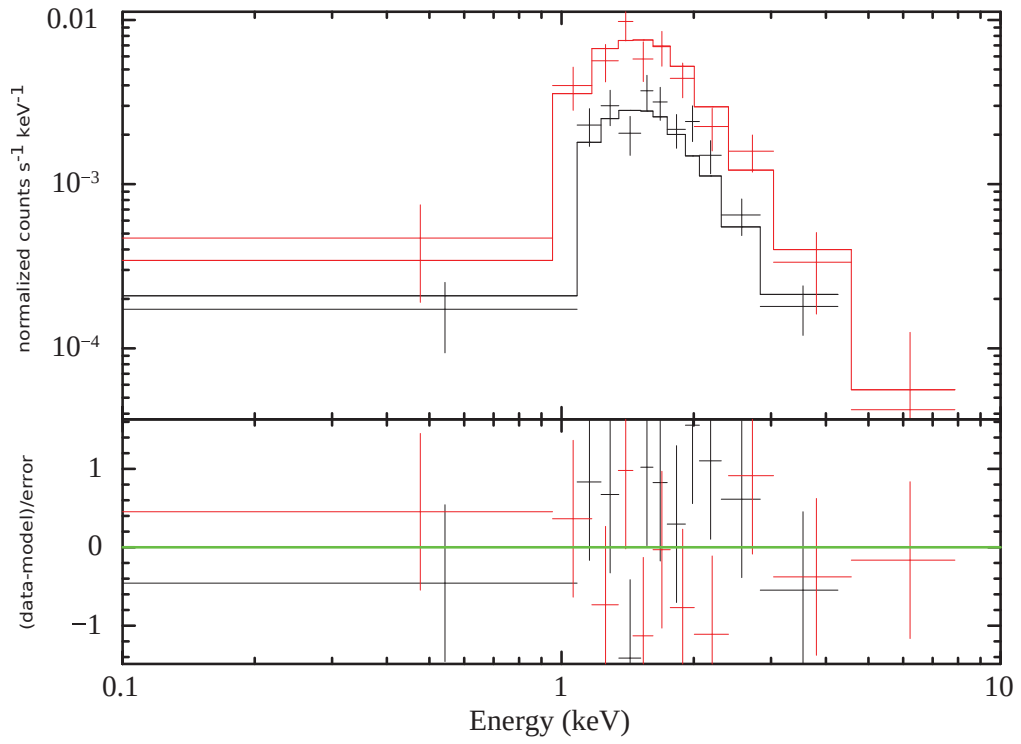
Figure 5.2: Fit of all spectra from MOS1+MOS2 (combined; black) and PN (red) to the nsa[pole]+nsa model, representing emission from a hot spot, and from the full surface, of a NS, with $B = 10^{12}$ G.

5.3   Pulsation Search

We attempted to search for pulsations from V0332+53, which is feasible for XMM imaging observations given the relatively long known spin period of 4.35 seconds. We extracted lightcurves from 15″ radius circular regions in the MOS and pn data, within which 239 photons were found, of which we estimate 55 to be background. We searched for periodicities using the *powspec* command in FTOOLS. No significant periodicities were detected.

To estimate our sensitivity limit for pulsations, we simulated XMM-Newton observations with different pulse fractions. We defined the pulse fraction as the semiamplitude of modulation, divided by the average source count rate (Campana et al., 2001). We tried various pulsed fractions up to 95%, but were unable to generate a detectable signal in these simulations. Trials with 1000 simulated source photons (vs. the 184 we obtained) produced a signal when the pulsed fraction reached 45%. We conclude that our observations were completely insensitive to pulsations from V0332+53 in quiescence, and that such searches on low-luminosity targets are quite difficult.

5.4   Discussion

For V0332+53, the value of the propeller regime cutoff luminosity from eq. 5.1 is $L_{min} \sim 3 \times 10^{36}$ erg s^{-1}, for typical NS mass and radius estimates. In table 5.1, we find L_X estimates, for different model choices, to be 0.4-1.4$\times 10^{33}$ erg s^{-1}. This is one of the lowest luminosities yet measured for a HMXB in quiescence, and is well below the cutoff luminosity for the propeller regime. Tsygankov et al. (2016) argue that V0332+53 showed clear evidence of a propeller effect truncating accretion during its 2015 outburst, while Wijnands & Degenaar (2016), observing the late decay with Swift, identify a slow dimming trend, suggesting either low-luminosity continuing accretion, or cooling of the NS crust post-accretion. Our observation of purely thermal emission from V0332+53 in quiescence may indicate that cooling of the NS crust powers its post-outburst luminosity. This argument is supported by analogy with low-mass X-ray binary NSs in quiescence, where purely

thermal emission has been found to be associated with a lack of variability (e.g. Walsh et al., 2015; Bahramian et al., 2015).

Accretion episodes deposit heat, through density-driven pycnonuclear reactions, in the inner crust (deep crustal heating), which diffuses through the core and slowly leaks to the surface over $\sim 10^4 - 10^5$ years (Haensel & Zdunik, 1990; Brown et al., 1998). Observations of the quiescent luminosity well after an outburst, combined with an estimate of the mass transfer rate, can measure the fraction of heat deposited in the core during outbursts that emerges as X-rays, vs. that escaping as undetected neutrinos (e.g. Colpi et al., 2001; Yakovlev & Pethick, 2004; Heinke et al., 2009). We plot the X-ray lightcurve observed for V0332+53 by *RXTE/ASM* between 1995 and 2004 and observed by *Swift* between 2005 and 2016 (Figure. 5.1). We estimate the time-averaged mass transfer rate from the companion to the neutron star based on the total X-ray luminosity observed,

$$L_x \sim \frac{GM_{NS}\dot{M}}{R_{NS}} \tag{5.2}$$

where we assume M_{NS}=1.4 $M_\odot$, and R_{NS}=11.5 km. Using the Crab flux and countrate as a reference, we calculate the X-ray flux based on the observed countrate from each instrument. We compute bolometric corrections assuming a power-law spectrum between 0.1 keV - 100 keV with photon index of 2. We calculate that the time-averaged mass transfer is 9.8×10^{-11} $M_\odot \mathrm{yr}^{-1}$, with an uncertainty of (± 0.1) $\times 10^{-11}$ $M_\odot \mathrm{yr}^{-1}$ from the conversion from countrate to flux, and an uncertainty of (± 0.4) $\times 10^{-11}$ $M_\odot \mathrm{yr}^{-1}$ from our uncertainty in the M/R value.

The thermal radiation that we see in quiescence could have one or more of three origins. It could be driven entirely by continued accretion, though this seems unlikely (see above). It could originate from heat deposited in the outer crust during the previous (2004) accretion episode (as suggested by Wijnands & Degenaar 2016). Or it could originate from heat deposited in the inner crust over multiple accretion episodes. The thermal conductivity of NSs is altered by B fields reaching 10^{12} G, permitting faster transport along magnetic field lines than across them; this predicts that NSs with relatively strong B fields will show hot spots at their magnetic poles (Greenstein et al., 1983; Potekhin & Yakovlev, 2001; Geppert et al., 2004).

Since our observation was taken 4 years after the last major outburst (see, e.g., crust cooling

curves in Shternin et al. 2007; Brown & Cumming 2009), we suspect that the thermal flux at this point is dominated by heat stored in the core. However, we do not know the *B* field and temperature distributions over the surface of the NS, and cannot yet rule out that a large portion of the emitted heat is radiated uniformly from the NS surface. Therefore, we calculate two reasonable limits on the thermal luminosity from deep crustal heating; one from the nsa[pole] hot spot model, and the other from the nsa[pole]+nsa hot spot plus surface model.

Comparing the time-averaged mass transfer rate with the observed quiescent thermal NS luminosity allows identification of a NS as following "standard" cooling tracks (dominated by modified Urca and/or neutron-neutron neutrino bremssstrahlung; Yakovlev & Pethick 2004; Page et al. 2006) or "enhanced" cooling tracks (e.g. direct Urca processes involving protons or hyperons, or similar processes involving pions, kaons, or quark matter; Yakovlev & Pethick 2004). Higher-mass NSs will have higher central densities, possibly permitting "enhanced" cooling, while lower-mass NSs are likely to follow "standard" cooling (Beznogov & Yakovlev, 2015). NSs in HMXBs have not had time to accrete substantial mass, but can be born with a range of masses (e.g. Rawls et al., 2011), so there is not a theoretical preference for the cooling rate of V0332+53.

We see (Figure 5.3) that if V0332+53's thermal luminosity is dominated by the hotspots that we have detected, then the NS is relatively cool, and seems to require slightly enhanced cooling. Alternatively, the rate of deep crustal heating per accretion episode might be reduced for young NSs like this one, since the relevant layers of the crust may not have been completely replaced by accreted material; see Wijnands et al. 2013. However, if V0332+53's thermal luminosity is dominated by emission from its entire surface, then it can be consistent with standard cooling tracks. The N_H to V03332+53 (as for most HMXBs) is unfortunately high enough to prevent tight constraints on the thermal luminosity from the full surface of the NS.
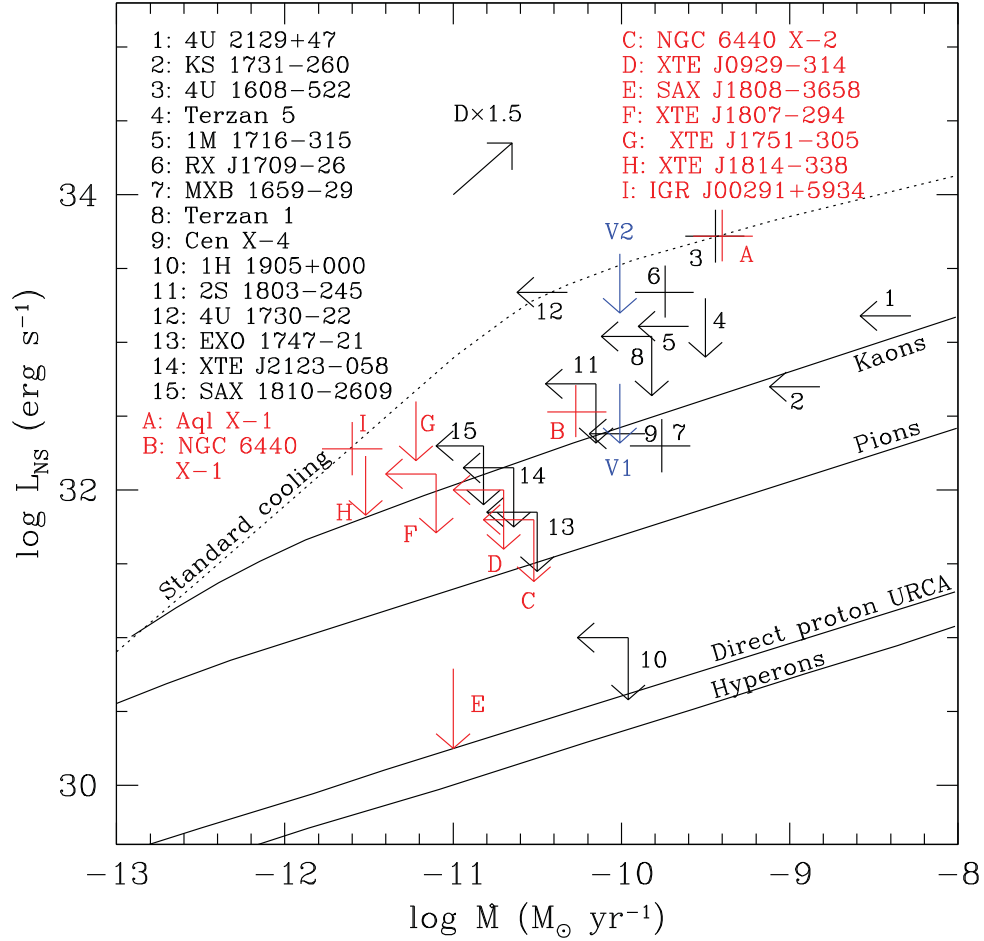
Figure 5.3: Time-averaged mass transfer rate (in $M_\odot$/yr) vs. quiescent thermal NS luminosity, for NS low-mass X-ray binaries (red: accreting millisecond pulsars; black: other NSs; after Heinke et al. 2007, 2009) and (in blue) for V0332+53. V1 marks the upper limit on thermal luminosity for the hot spot plus surface spectral model, while V2 marks the upper limit for the hot spot model alone. Sample calculations of standard and enhanced neutrino cooling are plotted following Yakovlev & Pethick (2004); see also Wijnands et al. (2013).

5.5 Summary

We performed a 39 ks *XMM-Newton* observation of the transient HMXB V0332+53 in quiescence to investigate the source of the quiescent X-ray emission. The low observed X-ray luminosity, L_x(0.5-10 keV)$\sim 4 \times 10^{32}$ erg s $^{-1}$, together with its 4.35 second spin period, and 3×10^{12} G magnetic field, indicates that V0332+53 is in the propeller regime. We attempted a search for pulsations, but the small number of photons from V0332+53 prevented a useful upper limit.

The X-ray spectrum of V0332+53 is quite soft, indicating thermal radiation from the surface, but the inferred radius when fit with a hydrogen NS atmosphere model is much smaller than the NS radius (a simple analysis suggests $0.27^{+0.22}_{-0.10}$ km), requiring hot spots on the NS.

From the known outburst history of V0332+53, we estimated the time-averaged mass transfer rate as $9.8 \pm 0.4 \times 10^{-11}$ $M_\odot \text{yr}^{-1}$. If the hotspot emission from V0332+53 is the dominant thermal emission from this NS, then this suggests that V0332+53 exhibits enhanced neutrino cooling, or reduced levels deep crustal heating due to the crust still being partly primordial, rather than accreted (Wijnands et al., 2013). However, we can only place an upper limit of $L_{bol} < 3 \times 10^{33}$ on thermal emission from the entire surface of the NS; if there is a strong thermal emission component from the full surface (in addition to the hotspot emission), then V0332+53 is consistent with standard cooling rates.

Chapter 6

Conclusions

In this thesis, I showed how X-ray observations of neutron stars were used to constrain some of its physical properties.

In chapter 2, I constrained the cooling measurement of the neutron star in Cas A using all *Chandra* detectors to be $2.9 \pm 0.5_{\mathrm{stat}} \pm 1.0_{\mathrm{sys}}\%$ over 10 years, where the systematic error range is due to different source and background extraction regions. Even a temperature decline as low as 1% over 10 years can be explained by models of NSs with nucleon cores that contain strong superfluidity of protons and moderately strong superfluidity of neutrons. However, recent work by Posselt et al. (2013) using *Chandra* ACIS-S observations in subarray mode argues that there may be only a marginal or no temperature decline at all, and that what we see in the other detectors is an artifact due to a combination of instrument calibration issues and absorbing filaments in the foreground of the moving neutron star.

In chapter 3, I explored the effect of the surface temperature inhomogeneities on quiescent low mass X-ray binaries, and particularly the application of these inhomogeneities to the neutron stars X5 and X7 in 47 Tuc, and the neutron star in Cen-X4. This research explored the limits on the surface temperature based on the upper limits of pulsation searches, where the 90% upper limits on the pulsed fractions from 800 ks *Chandra* HRC-S observation for the two sources X5 and X7 in the globular cluster 47-Tuc are 14% and 13% respectively, searching spin frequencies < 500 Hz. For

higher spin frequencies (up to 716 Hz) the limits are 16% and 15% respectively. The pulse profiles were simulated for ranges of inclination and hot spot emission angles i and e, obtaining the central 90% range of pulse fraction obtained for different choices of temperature differentials (between the hot spot and the rest of the NS) and NS spin frequencies. In the case of X7, if we assume it is a 1.4 $M_\odot$ neutron star spinning at 500 Hz, the results indicate that the maximum allowable temperature differential is 0.055 keV, where > 90% of our simulations are above the 90% upper limit of pulsed fraction. The neutron star in Cen-X4 has a significantly lower upper limit on the pulse fraction of 6.4%, which puts a tighter constraint on the maximum allowable temperature differential of 0.025 keV.

In chapter 4, I studied the effects on the inferred radius, particularly for X5 and X7 in 47 Tuc, of hot spots for these temperature differential limits. We found that the existence of an unmodeled hot spot tends to shift the peak of the spectrum to higher energies, which reduces the spectroscopically inferred equatorial radii of neutron stars below the "true" radius. The 90% confidence range of the inferred radii are generally still consistent with the true value of our fiducial star (11.5 km) for small temperature differentials (0.03 keV). For the hottest possible hot spots that would not give rise to detectable pulsations in X7, we find that a bias in the best-fit inferred radius of up to 28% smaller than the true radius may be induced by hot spots below our upper limit.

Finally, in chapter 5, I performed a 39 ks *XMM-Newton* observation of the transient HMXB V0332+53 in quiescence to investigate the source of the quiescent X-ray emission. The neutron star in V0332+53 is in the propeller regime. We attempted a search for pulsations, but the small number of photons from V0332+53 prevented a useful upper limit. The X-ray spectrum of V0332+53 is quite soft, indicating thermal radiation from the surface, but the inferred radius when fit with a hydrogen NS atmosphere model is much smaller than the NS radius (a simple analysis suggests $0.27^{+0.22}_{-0.10}$ km), requiring hot spots on the NS. The time-averaged mass transfer rate is estimated as $9.8 \pm 0.4 \times 10^{-11}$ $M_\odot \mathrm{yr}^{-1}$. If the hotspot emission from V0332+53 is the dominant thermal emission from this NS, then this suggests that V0332+53 exhibits enhanced neutrino cooling, or reduced levels of deep crustal heating due to the crust still being partly primordial, rather than

accreted.

References

Akmal, A. & Pandharipande, V. R. 1997, Phys. Rev. C, 56, 2261

Alcock, C. & Illarionov, A. 1980, ApJ, 235, 534

Antoniadis, J., Freire, P. C. C., Wex, N., Tauris, T. M., Lynch, R. S., van Kerkwijk, M. H., Kramer, M., Bassa, C., Dhillon, V. S., Driebe, T., Hessels, J. W. T., Kaspi, V. M., Kondratiev, V. I., Langer, N., Marsh, T. R., McLaughlin, M. A., Pennucci, T. T., Ransom, S. M., Stairs, I. H., van Leeuwen, J., Verbiest, J. P. W., & Whelan, D. G. 2013, Science, 340, 448

Archibald, A. M., Bogdanov, S., Patruno, A., Hessels, J. W. T., Deller, A. T., Bassa, C., Janssen, G. H., Kaspi, V. M., Lyne, A. G., Stappers, B. W., Tendulkar, S. P., D'Angelo, C. R., & Wijnands, R. 2015, ApJ, 807, 62

Arnaud, K. A. 1996, in ASP Conf. Ser. 101: Astronomical Data Analysis Software and Systems V, 17

Bahramian, A., Heinke, C. O., Degenaar, N., Chomiuk, L., Wijnands, R., Strader, J., Ho, W. C. G., & Pooley, D. 2015, MNRAS, 452, 3475

Bahramian, A., Heinke, C. O., Sivakoff, G. R., Altamirano, D., Wijnands, R., Homan, J., Linares, M., Pooley, D., Degenaar, N., & Gladstone, J. C. 2014, ApJ, 780, 127

Balucinska-Church, M. & McCammon, D. 1992, ApJ, 400, 699

Bauböck, M., Özel, F., Psaltis, D., & Morsink, S. M. 2015a, ApJ, 799, 22

Bauböck, M., Psaltis, D., & Özel, F. 2015b, ApJ, 811, 144

Becker, W., Swartz, D. A., Pavlov, G. G., Elsner, R. F., Grindlay, J., Mignani, R., Tennant, A. F., Backer, D., Pulone, L., Testa, V., & Weisskopf, M. C. 2003, ApJ, 594, 798

Beznogov, M. V. & Yakovlev, D. G. 2015, MNRAS, 452, 540

Bhattacharya, D. & van den Heuvel, E. P. J. 1991, Phys. Rep., 203, 1

Bhattacharyya, S. 2010, Advances in Space Research, 45, 949

Blaschke, D., Grigorian, H., Voskresensky, D. N., & Weber, F. 2012, Phys. Rev. C, 85, 022802

Bogdanov, S. 2013, ApJ, 762, 96

Bogdanov, S., Archibald, A. M., Hessels, J. W. T., Kaspi, V. M., Lorimer, D., McLaughlin, M. A., Ransom, S. M., & Stairs, I. H. 2011, ApJ, 742, 97

Bogdanov, S. & Grindlay, J. E. 2009, ApJ, 703, 1557

Bogdanov, S., Heinke, C. O., Özel, F., & Güver, T. 2016, ArXiv e-prints

Bogdanov, S., Rybicki, G. B., & Grindlay, J. E. 2007, ApJ, 670, 668

Brown, E. F., Bildsten, L., & Rutledge, R. E. 1998, ApJ, 504, L95

Brown, E. F. & Cumming, A. 2009, ApJ, 698, 1020

Caballero-Garcia, M. D., Camero-Arranz, A., Ozbey Arabaci, M., Hudec, R., & on behalf of a larger collaboration. 2015, ArXiv e-prints

Cackett, E. M., Brown, E. F., Miller, J. M., & Wijnands, R. 2010, ApJ, 720, 1325

Cadeau, C., Morsink, S. M., Leahy, D., & Campbell, S. S. 2007, ApJ, 654, 458

Cameron, P. B., Rutledge, R. E., Camilo, F., Bildsten, L., Ransom, S. M., & Kulkarni, S. R. 2007, ApJ, 660, 587

Campana, S., Brivio, F., Degenaar, N., Mereghetti, S., Wijnands, R., D'Avanzo, P., Israel, G. L., & Stella, L. 2014, MNRAS, 441, 1984

Campana, S., Colpi, M., Mereghetti, S., Stella, L., & Tavani, M. 1998a, A&A Rev., 8, 279

Campana, S., Gastaldello, F., Stella, L., Israel, G. L., Colpi, M., Pizzolato, F., Orlandini, M., & Dal Fiume, D. 2001, ApJ, 561, 924

Campana, S., Stella, L., Gastaldello, F., Mereghetti, S., Colpi, M., Israel, G. L., Burderi, L., Di Salvo, T., & Robba, R. N. 2002, ApJ, 575, L15

Campana, S., Stella, L., & Kennea, J. A. 2008, ApJ, 684, L99

Campana, S., Stella, L., Mereghetti, S., Colpi, M., Tavani, M., Ricci, D., Dal Fiume, D., & Belloni, T. 1998b, ApJ, 499, L65

Campana, S., Stella, L., Mereghetti, S., Colpi, M., Tavani, M., Ricci, D., Fiume, D. D., & Belloni, T. 1998c, ApJ, 499, L65

Catuneanu, A., Heinke, C. O., Sivakoff, G. R., Ho, W. C. G., & Servillat, M. 2013, ApJ, 764, 145

Chakrabarty, D., Tomsick, J. A., Grefenstette, B. W., Psaltis, D., Bachetti, M., Barret, D., Boggs, S. E., Christensen, F. E., Craig, W. W., Fürst, F., Hailey, C. J., Harrison, F. A., Kaspi, V. M., Miller, J. M., Nowak, M. A., Rana, V., Stern, D., Wik, D. R., Wilms, J., & Zhang, W. W. 2014, ApJ, 797, 92

Chang, P., Bildsten, L., & Arras, P. 2010, ApJ, 723, 719

Chen, K. & Ruderman, M. 1993, ApJ, 408, 179

Chen, K., Ruderman, M., & Zhu, T. 1998, ApJ, 493, 397

Chevalier, C. & Ilovaisky, S. A. 1989, in ESA Special Publication, Vol. 296, Two Topics in X-Ray Astronomy, Volume 1: X Ray Binaries. Volume 2: AGN and the X Ray Background, ed. J. Hunt & B. Battrick, 345–347

Colpi, M., Geppert, U., Page, D., & Possenti, A. 2001, ApJ, 548, L175

Cooper, L. N. 1956, Phys. Rev., 104, 1189

Corbet, R. H. D., Charles, P. A., & van der Klis, M. 1986, A&A, 162, 117

Cui, W. 1997, ApJ, 482, L163

Cui, W. & Smith, B. 2004, ApJ, 602, 320

Damen, E., Magnier, E., Lewin, W. H. G., Tan, J., Penninx, W., & van Paradijs, J. 1990, A&A, 237, 103

Damour, T. & Deruelle, N. 1986, Ann. Inst. Henri Poincaré Phys. Théor., Vol. 44, No. 3, p. 263 - 292, 44, 263

Damour, T., Soffel, M., & Xu, C. 1992, Phys. Rev. D, 45, 1017

D'Angelo, C. R., Fridriksson, J. K., Messenger, C., & Patruno, A. 2015, MNRAS, 449, 2803

Davidsen, A., Henry, J. P., Middleditch, J., & Smith, H. E. 1972, ApJ, 177, L97

Davis, J. E. 2001, ApJ, 562, 575

De Luca, A., Caraveo, P. A., Mereghetti, S., Negroni, M., & Bignami, G. F. 2005, ApJ, 623, 1051

Demorest, P. B., Pennucci, T., Ransom, S. M., Roberts, M. S. E., & Hessels, J. W. T. 2010, Nature, 467, 1081

Deufel, B., Dullemond, C. P., & Spruit, H. C. 2001, A&A, 377, 955

Doroshenko, V., Santangelo, A., Doroshenko, R., Caballero, I., Tsygankov, S., & Rothschild, R. 2014, A&A, 561, A96

Doroshenko, V., Santangelo, A., & Suleimanov, V. 2011, A&A, 529, A52

Doroshenko, V., Tsygankov, S., & Santangelo, A. 2016, A&A, 589, A72

Edmonds, P. D., Heinke, C. O., Grindlay, J. E., & Gilliland, R. L. 2002, ApJ, 564, L17

Engvik, L., Osnes, E., Hjorth-Jensen, M., Bao, G., & Ostgaard, E. 1996, ApJ, 469, 794

Fesen, R. A., Hammell, M. C., Morse, J., Chevalier, R. A., Borkowski, K. J., Dopita, M. A., Gerardy, C. L., Lawrence, S. S., Raymond, J. C., & van den Bergh, S. 2006, ApJ, 645, 283

Flowers, E., Ruderman, M., & Sutherland, P. 1976, ApJ, 205, 541

Foight, D., Guver, T., Ozel, F., & Slane, P. 2015, ArXiv e-prints

Freire, P. C. C., Bassa, C. G., Wex, N., Stairs, I. H., Champion, D. J., Ransom, S. M., Lazarus, P., Kaspi, V. M., Hessels, J. W. T., Kramer, M., Cordes, J. M., Verbiest, J. P. W., Podsiadlowski, P., Nice, D. J., Deneva, J. S., Lorimer, D. R., Stappers, B. W., McLaughlin, M. A., & Camilo, F. 2011, MNRAS, 412, 2763

Fridriksson, J. K., Homan, J., Wijnands, R., Méndez, M., Altamirano, D., Cackett, E. M., Brown, E. F., Belloni, T. M., Degenaar, N., & Lewin, W. H. G. 2010, ApJ, 714, 270

Galloway, D. K. & Lampe, N. 2012, ApJ, 747, 75

Geppert, U., Küker, M., & Page, D. 2004, A&A, 426, 267

Giacconi, R., Gursky, H., Kellogg, E., Schreier, E., & Tananbaum, H. 1971, ApJ, 167, L67

Gierliński, M., Done, C., & Barret, D. 2002, MNRAS, 331, 141

Glendenning, N. K. & Moszkowski, S. A. 1991, Physical Review Letters, 67, 2414

Glendenning, N. K. & Schaffner-Bielich, J. 1998, Physical Review Letters, 81, 4564

Gnedin, O. Y., Yakovlev, D. G., & Potekhin, A. Y. 2001, MNRAS, 324, 725

Gotthelf, E. V., Halpern, J. P., & Alford, J. 2013, ApJ, 765, 58

Gotthelf, E. V., Perna, R., & Halpern, J. P. 2010, ApJ, 724, 1316

Gratton, R. G., Bragaglia, A., Carretta, E., & et al. 2003, A&A, 408, 529

Greenstein, J. L., Dolez, N., & Vauclair, G. 1983, A&A, 127, 25

Grindlay, J. E., Heinke, C., Edmonds, P. D., & Murray, S. S. 2001, Science, 292, 2290

Guillot, S., Kaspi, V. M., Archibald, R. F., Bachetti, M., Flynn, C., Jankowski, F., Bailes, M., Boggs, S., Christensen, F. E., Craig, W. W., Hailey, C. A., Harrison, F. A., Stern, D., & Zhang, W. W. 2015, ArXiv e-prints

Guillot, S., Rutledge, R. E., Brown, E. F., Pavlov, G. G., & Zavlin, V. E. 2011, ApJ, 738, 129

Guillot, S., Servillat, M., Webb, N. A., & Rutledge, R. E. 2013, ApJ, 772, 7

Gusakov, M. E., Kaminker, A. D., Yakovlev, D. G., & Gnedin, O. Y. 2004, A&A, 423, 1063

Güver, T., Özel, F., Cabrera-Lavers, A., & Wroblewski, P. 2010a, ApJ, 712, 964

Güver, T., Wroblewski, P., Camarota, L., & Özel, F. 2010b, ApJ, 719, 1807

Haakonsen, C. B., Turner, M. L., Tacik, N. A., & Rutledge, R. E. 2012, ApJ, 749, 52

Haensel, P., Bejger, M., Fortin, M., & Zdunik, L. 2016, European Physical Journal A, 52, 59

Haensel, P. & Zdunik, J. L. 1990, A&A, 227, 431

Haggard, D., Cool, A. M., Anderson, J., Edmonds, P. D., Callanan, P. J., Heinke, C. O., Grindlay, J. E., & Bailyn, C. D. 2004, ApJ, 613, 512

Halpern, J. P. & Gotthelf, E. V. 2010, ApJ, 709, 436

Hameury, J. M., Heyvaerts, J., & Bonazzola, S. 1983, A&A, 121, 259

Hansen, B. M. S., Kalirai, J. S., Anderson, J., Dotter, A., Richer, H. B., Rich, R. M., Shara, M. M., Fahlman, G. G., Hurley, J. R., King, I. R., Reitzel, D., & Stetson, P. B. 2013, Nature, 500, 51

Harding, A. K., Strickman, M. S., Gwinn, C., Dodson, R., Moffet, D., & McCulloch, P. 2002, ApJ, 576, 376

Hasinger, G., Johnston, H. M., & Verbunt, F. 1994, A&A, 288, 466

Hebeler, K., Lattimer, J. M., Pethick, C. J., & Schwenk, A. 2013, ApJ, 773, 11

Heinke, C. O., Cohn, H. N., Lugger, P. M., Webb, N. A., Ho, W. C. G., Anderson, J., Campana, S., Bogdanov, S., Haggard, D., Cool, A. M., & Grindlay, J. E. 2014, MNRAS, 444, 443

Heinke, C. O., Grindlay, J. E., Lloyd, D. A., & Edmonds, P. D. 2003, ApJ, 588, 452

Heinke, C. O. & Ho, W. C. G. 2010, ApJ, 719, L167

Heinke, C. O., Jonker, P. G., Wijnands, R., Deloye, C. J., & Taam, R. E. 2009, ApJ, 691, 1035

Heinke, C. O., Jonker, P. G., Wijnands, R., & Taam, R. E. 2007, ApJ, 660, 1424

Heinke, C. O., Rybicki, G. B., Narayan, R., & Grindlay, J. E. 2006, ApJ, 644, 1090

Hernquist, L. 1985, MNRAS, 213, 313

Hertz, P. & Grindlay, J. E. 1983, ApJ, 275, 105

Hessels, J. W. T., Ransom, S. M., Stairs, I. H., Freire, P. C. C., Kaspi, V. M., & Camilo, F. 2006, Science, 311, 1901

Ho, W. C. G. 2013, in IAU Symposium, Vol. 291, IAU Symposium, 101–106

Ho, W. C. G. & Heinke, C. O. 2009, Nature, 462, 71

Hwang, U. & Laming, J. M. 2012, ApJ, 746, 130

Illarionov, A. F. & Sunyaev, R. A. 1975, A&A, 39, 185

Johnson, T. J., Venter, C., Harding, A. K., Guillemot, L., Smith, D. A., Kramer, M., Çelik, Ö., den Hartog, P. R., Ferrara, E. C., Hou, X., Lande, J., & Ray, P. S. 2014, ApJS, 213, 6

Kaminker, A. D., Haensel, P., & Yakovlev, D. G. 2001, A&A, 373, L17

Kreykenbohm, I., Mowlavi, N., Produit, N., Soldi, S., Walter, R., Dubath, P., Lubiński, P., Türler, M., Coburn, W., Santangelo, A., Rothschild, R. E., & Staubert, R. 2005, A&A, 433, L45

La Palombara, N. & Mereghetti, S. 2006, A&A, 455, 283

—. 2007, A&A, 474, 137

La Palombara, N., Sidoli, L., Esposito, P., Tiengo, A., & Mereghetti, S. 2009, A&A, 505, 947

Lamb, F. K., Boutloukos, S., Van Wassenhove, S., Chamberlain, R. T., Lo, K. H., Clare, A., Yu, W., & Miller, M. C. 2009, ApJ, 706, 417

Lamb, F. K., Pethick, C. J., & Pines, D. 1973, ApJ, 184, 271

Lattimer, J. M. & Prakash, M. 2001, ApJ, 550, 426

—. 2007, Phys. Rep., 442, 109

—. 2016, Phys. Rep., 621, 127

Lattimer, J. M., Prakash, M., Pethick, C. J., & Haensel, P. 1991, Physical Review Letters, 66, 2701

Lattimer, J. M. & Steiner, A. W. 2014, ApJ, 784, 123

Lattimer, J. M., van Riper, K. A., Prakash, M., & Prakash, M. 1994, ApJ, 425, 802

Leahy, D. A., Darbro, W., Elsner, R. F., Weisskopf, M. C., Kahn, S., Sutherland, P. G., & Grindlay, J. E. 1983, ApJ, 266, 160

Leinson, L. B. 2010, Phys. Rev. C, 81, 025501

Lewin, W. H. G., van Paradijs, J., & Taam, R. E. 1993, Space Sci. Rev., 62, 223

Lloyd, D. A. 2003, ArXiv e-prints

Lyne, A., Graham-Smith, F., & Graham-Smith, F. 2006, Pulsar Astronomy, Cambridge Astrophysics (Cambridge University Press)

Makishima, K., Ohashi, T., Kawai, N., Matsuoka, M., Koyama, K., Kunieda, H., Tawara, Y., Ushimaru, N., Corbet, R. H. D., Inoue, H., Kii, T., Makino, F., Mitsuda, K., Murakami, T., Nagase, F., Ogawara, Y., Tanaka, Y., Kitamoto, S., Miyamoto, S., Tsunemi, H., & Yamashita, K. 1990, PASJ, 42, 295

Manchester, R. N. & Han, J. L. 2004, ApJ, 609, 354

Manchester, R. N. & Lyne, A. G. 1977, MNRAS, 181, 761

Manzali, A., De Luca, A., & Caraveo, P. A. 2007, ApJ, 669, 570

McClintock, J. E., Narayan, R., & Rybicki, G. B. 2004, ApJ, 615, 402

McLaughlin, M. A., Cordes, J. M., Deshpande, A. A., Gaensler, B. M., Hankins, T. H., Kaspi, V. M., & Kern, J. S. 2001, ApJ, 547, L41

Mereghetti, S., Bignami, G. F., Caraveo, P. A., & Goldwurm, A. 1987, ApJ, 312, 755

Mereghetti, S., Tiengo, A., & Israel, G. L. 2002, ApJ, 569, 275

Messenger, C. 2011, Phys. Rev. D, 84, 083003

Middleditch, J. 1976, PhD thesis, California Univ., Berkeley.

Migdal, A. 1959, Nucl. Phys. A, 13, 655

Miller, M. C. & Lamb, F. K. 1998, ApJ, 499, L37

Miller, M. C. & Miller, J. M. 2015, Phys. Rep., 548, 1

Morsink, S. M., Leahy, D. A., Cadeau, C., & Braga, J. 2007, ApJ, 663, 1244

Mukherjee, U. & Paul, B. 2005, A&A, 431, 667

Müller, H. & Serot, B. D. 1996, Nuclear Physics A, 606, 508

Murray, S. S., Ransom, S. M., Juda, M., Hwang, U., & Holt, S. S. 2002, ApJ, 566, 1039

Nättilä, J., Steiner, A. W., Kajava, J. J. E., Suleimanov, V. F., & Poutanen, J. 2015, ArXiv e-prints

Negreiros, R., Ruffini, R., Bianco, C. L., & Rueda, J. A. 2012, A&A, 540, A12

Negueruela, I., Reig, P., Finger, M. H., & Roche, P. 2000, A&A, 356, 1003

Negueruela, I., Roche, P., Fabregat, J., & Coe, M. J. 1999, MNRAS, 307, 695

Oppenheimer, J. R. & Volkoff, G. M. 1939, Phys. Rev., 55, 374

Özel, F. 2006, Nature, 441, 1115

Özel, F. 2013, Reports on Progress in Physics, 76, 016901

Özel, F., Güver, T., & Psaltis, D. 2009, ApJ, 693, 1775

Özel, F., Psaltis, D., Güver, T., Baym, G., Heinke, C., & Guillot, S. 2016, ApJ, 820, 28

Page, D., Geppert, U., & Weber, F. 2006, Nuclear Physics A, 777, 497

Page, D., Lattimer, J. M., Prakash, M., & Steiner, A. W. 2004, ApJS, 155, 623

—. 2009, ApJ, 707, 1131

Page, D., Prakash, M., Lattimer, J. M., & Steiner, A. W. 2011, Physical Review Letters, 106, 081101

Papitto, A., Ferrigno, C., Bozzo, E., Rea, N., Pavan, L., Burderi, L., Burgay, M., Campana, S., di Salvo, T., Falanga, M., Filipović, M. D., Freire, P. C. C., Hessels, J. W. T., Possenti, A., Ransom, S. M., Riggio, A., Romano, P., Sarkissian, J. M., Stairs, I. H., Stella, L., Torres, D. F., Wieringa, M. H., & Wong, G. F. 2013, Nature, 501, 517

Papitto, A., Torres, D. F., Rea, N., & Tauris, T. M. 2014, A&A, 566, A64

Patnaude, D. J. & Fesen, R. A. 2009, ApJ, 697, 535

Pavlov, G. G. & Luna, G. J. M. 2009, ApJ, 703, 910

Pavlov, G. G., Shibanov, Y. A., Ventura, J., & Zavlin, V. E. 1994, A&A, 289, 837

Pavlov, G. G., Shibanov, Y. A., Zavlin, V. E., & Meyer, R. D. 1995, in The Lives of the Neutron
    Stars, ed. M. A. Alpar, U. Kiziloglu, & J. van Paradijs, 71

Pechenick, K. R., Ftaclas, C., & Cohen, J. M. 1983, ApJ, 274, 846

Pethick, C. J. & Thorsson, V. 1995, in The Lives of the Neutron Stars, ed. M. A. Alpar, U. Kiziloglu,
    & J. van Paradijs, 121

Pons, J. A., Miralles, J. A., Prakash, M., & Lattimer, J. M. 2001, ApJ, 553, 382

Pons, J. A., Walter, F. M., Lattimer, J. M., Prakash, M., Neuhäuser, R., & An, P. 2002, ApJ, 564,
    981

Posselt, B., Pavlov, G. G., Suleimanov, V., & Kargaltsev, O. 2013, ApJ, 779, 186

Potekhin, A. Y. & Yakovlev, D. G. 2001, A&A, 374, 213

Pottschmidt, K., Kreykenbohm, I., Wilms, J., Coburn, W., Rothschild, R. E., Kretschmar, P.,
    McBride, V., Suchy, S., & Staubert, R. 2005, ApJ, 634, L97

Poutanen, J. & Gierliński, M. 2003, MNRAS, 343, 1301

Poutanen, J., Nättilä, J., Kajava, J. J. E., Latvala, O.-M., Galloway, D. K., Kuulkers, E., &
    Suleimanov, V. F. 2014, MNRAS, 442, 3777

Prakash, M., Cooke, J. R., & Lattimer, J. M. 1995, Phys. Rev. D, 52, 661

Prakash, M., Lattimer, J. M., & Ainsworth, T. L. 1988, Physical Review Letters, 61, 2518

Prakash, M., Prakash, M., Lattimer, J. M., & Pethick, C. J. 1992, ApJ, 390, L77

Predehl, P., Costantini, E., Hasinger, G., & Tanaka, Y. 2003, Astronomische Nachrichten, 324, 73

Predehl, P., Hasinger, G., & Verbunt, F. 1991, A&A, 246, L21

Psaltis, D., Özel, F., & Chakrabarty, D. 2014, ApJ, 787, 136

Psaltis, D., Özel, F., & DeDeo, S. 2000, ApJ, 544, 390

Rajagopal, M. & Romani, R. W. 1996, ApJ, 461, 327

Ransom, S. M. 2002, in Astronomical Society of the Pacific Conference Series, Vol. 271, Neutron Stars in Supernova Remnants, ed. P. O. Slane & B. M. Gaensler, 361–+

Ransom, S. M., Cordes, J. M., & Eikenberry, S. S. 2003, ApJ, 589, 911

Ransom, S. M., Greenhill, L. J., Herrnstein, J. R., Manchester, R. N., Camilo, F., Eikenberry, S. S., & Lyne, A. G. 2001, ApJ, 546, L25

Ransom, S. M., Stairs, I. H., Archibald, A. M., Hessels, J. W. T., Kaplan, D. L., van Kerkwijk, M. H., Boyles, J., Deller, A. T., Chatterjee, S., Schechtman-Rook, A., Berndsen, A., Lynch, R. S., Lorimer, D. R., Karako-Argaman, C., Kaspi, V. M., Kondratiev, V. I., McLaughlin, M. A., van Leeuwen, J., Rosen, R., Roberts, M. S. E., & Stovall, K. 2014, Nature, 505, 520

Rawls, M. L., Orosz, J. A., McClintock, J. E., Torres, M. A. P., Bailyn, C. D., & Buxton, M. M. 2011, ApJ, 730, 25

Reed, J. E., Hester, J. J., Fabian, A. C., & Winkler, P. F. 1995, ApJ, 440, 706

Reig, P., Doroshenko, V., & Zezas, A. 2014, MNRAS, 445, 1314

Romani, R. W. 1987, ApJ, 313, 718

Romanova, M. M., Ustyugova, G. V., Koldoba, A. V., & Lovelace, R. V. E. 2004, ApJ, 616, L151

Rothschild, R., Markowitz, A., Hemphill, P., Caballero, I., Pottschmidt, K., Kühnel, M., Wilms, J., Fürst, F., Doroshenko, V., & Camero-Arranz, A. 2013, ApJ, 770, 19

Rutledge, R. E., Bildsten, L., Brown, E. F., Chakrabarty, D., Pavlov, G. G., & Zavlin, V. E. 2007, ApJ, 658, 514

Rutledge, R. E., Bildsten, L., Brown, E. F., Pavlov, G. G., & Zavlin, V. E. 2002a, ApJ, 578, 405

Rutledge, R. E., Bildsten, L., Brown, E. F., Pavlov, G. G., Zavlin, V. E., & Ushomirsky, G. 2002b, ApJ, 580, 413

Rutledge, R. E., Fox, D. W., Kulkarni, S. R., Jacoby, B. A., Cognard, I., Backer, D. C., & Murray, S. S. 2004, ApJ, 613, 522

Schreier, E., Levinson, R., Gursky, H., Kellogg, E., Tananbaum, H., & Giacconi, R. 1972, ApJ, 172, L79

Sedrakian, A. 2013, ArXiv e-prints

Servillat, M., Heinke, C. O., Ho, W. C. G., Grindlay, J. E., Hong, J., van den Berg, M., & Bogdanov, S. 2012, MNRAS, 423, 1556

Shapiro, S. L. & Teukolsky, S. A. 1983, Black holes, white dwarfs, and neutron stars: The physics of compact objects

Shen, G., Horowitz, C. J., & Teige, S. 2010, Phys. Rev. C, 82, 045802

Shternin, P. S., Yakovlev, D. G., Haensel, P., & Potekhin, A. Y. 2007, MNRAS, 382, L43

Shternin, P. S., Yakovlev, D. G., Heinke, C. O., Ho, W. C. G., & Patnaude, D. J. 2011, MNRAS, 412, L108

Shtykovskiy, P. & Gilfanov, M. 2005, A&A, 431, 597

Steiner, A. W., Lattimer, J. M., & Brown, E. F. 2010, ApJ, 722, 33

—. 2016, European Physical Journal A, 52, 18

Stella, L., White, N. E., Davelaar, J., Parmar, A. N., Blissett, R. J., & van der Klis, M. 1985, ApJ, 288, L45

Stella, L., White, N. E., & Rosner, R. 1986, ApJ, 308, 669

Strüder, L. & et al. 2001, A&A, 365, L18

Suleimanov, V., Poutanen, J., & Werner, K. 2011, A&A, 527, A139

Sztajno, M., Fujimoto, M. Y., van Paradijs, J., Vacca, W. D., Lewin, W. H. G., Penninx, W., & Trumper, J. 1987, MNRAS, 226, 39

Tanaka, Y. 1983, IAU Circ., 3891

Tananbaum, H. 1999, IAU Circ., 7246, 1

Tananbaum, H., Gursky, H., Kellogg, E., Giacconi, R., & Jones, C. 1972, ApJ, 177, L5

Tauris, T. M., Langer, N., & Kramer, M. 2012, MNRAS, 425, 1601

Terrell, J. & Priedhorsky, W. C. 1984, ApJ, 285, L15

Townsley, L. K., Broos, P. S., Garmire, G. P., & Nousek, J. A. 2000, ApJ, 534, L139

Tsuruta, S. 1998, Phys. Rep., 292, 1

Tsuruta, S., Sadino, J., Kobelski, A., Teter, M. A., Liebmann, A. C., Takatsuka, T., Nomoto, K., & Umeda, H. 2009, ApJ, 691, 621

Tsygankov, S. S., Lutovinov, A. A., Doroshenko, V., Mushtukov, A. A., & Poutanen, J. 2016, ArXiv e-prints

Turner, M. J. L. & et al. 2001, A&A, 365, L27

van Paradijs, J. 1979, ApJ, 234, 609

Vaughan, B. A., van der Klis, M., Wood, K. S., Norris, J. P., Hertz, P., Michelson, P. F., van Paradijs, J., Lewin, W. H. G., Mitsuda, K., & Penninx, W. 1994, ApJ, 435, 362

Verbunt, F. & Hasinger, G. 1998, A&A, 336, 895

Walsh, A. R., Cackett, E. M., & Bernardini, F. 2015, MNRAS, 449, 1238

Wang, Z., Kaplan, D. L., & Chakrabarty, D. 2007, ApJ, 655, 261

Webb, N. A. & Barret, D. 2007, ApJ, 671, 727

White, N. E., Swank, J. H., & Holt, S. S. 1983, ApJ, 270, 711

Wijnands, R. & Degenaar, N. 2016, ArXiv e-prints

Wijnands, R., Degenaar, N., & Page, D. 2013, MNRAS, 432, 2366

Wilms, J., Allen, A., & McCray, R. 2000, ApJ, 542, 914

Woodley, K. A., Goldsbury, R., Kalirai, J. S., Richer, H. B., Tremblay, P.-E., Anderson, J., Bergeron, P., Dotter, A., Esteves, L., Fahlman, G. G., Hansen, B. M. S., Heyl, J., Hurley, J., Rich, R. M., Shara, M. M., & Stetson, P. B. 2012, AJ, 143, 50

Worpel, H., Galloway, D. K., & Price, D. J. 2013, ApJ, 772, 94

Yakovlev, D. G., Ho, W. C. G., Shternin, P. S., Heinke, C. O., & Potekhin, A. Y. 2011, MNRAS, 411, 1977

Yakovlev, D. G., Kaminker, A. D., Gnedin, O. Y., & Haensel, P. 2001, Phys. Rep., 354, 1

Yakovlev, D. G., Levenfish, K. P., & Haensel, P. 2003, A&A, 407, 265

Yakovlev, D. G., Levenfish, K. P., & Shibanov, Y. A. 1999, Physics Uspekhi, 42, 737

Yakovlev, D. G. & Pethick, C. J. 2004, ARA&A, 42, 169

Zamfir, M., Cumming, A., & Galloway, D. K. 2012, ApJ, 749, 69

Zavlin, V. E. 2006, ApJ, 638, 951

Zavlin, V. E. & Pavlov, G. G. 1998, A&A, 329, 583

Zavlin, V. E. & Pavlov, G. G. 2002, in Neutron Stars, Pulsars, and Supernova Remnants, ed. W. Becker, H. Lesch, & J. Trümper, 263

Zavlin, V. E., Pavlov, G. G., Sanwal, D., & Trümper, J. 2000, ApJ, 540, L25

Zavlin, V. E., Pavlov, G. G., & Shibanov, Y. A. 1996, A&A, 315, 141